Doctoral theses at NTNU, 2022:218

Dario Rafael Fernandez Castellon

Probabilistic modelling of wind induced load effects for suspension bridges with emphasis on long-term extreme value analysis

Doctoral thesis

NTNU
Norwegian University of Science and Technology
Thesis for the Degree of
Philosophiae Doctor
Faculty of Engineering
Department of Structural Engineering

NTNU
Norwegian University of
Science and Technology

Dario Rafael Fernandez Castellon

Probabilistic modelling of wind induced load effects for suspension bridges with emphasis on long-term extreme value analysis

Thesis for the Degree of Philosophiae Doctor

Trondheim, June 2022

Norwegian University of Science and Technology
Faculty of Engineering
Department of Structural Engineering

NTNU
Norwegian University of
Science and Technology

NTNU
Norwegian University of Science and Technology

Thesis for the Degree of Philosophiae Doctor

Faculty of Engineering
Department of Structural Engineering

ISBN 978-82-326-5343-0 (printed ver.)
ISBN 978-82-326-5401-7 (electronic ver.)
ISSN 1503-8181 (printed ver.)
ISSN 2703-8084 (online ver.)

Doctoral theses at NTNU, 2022:218

Printed by NTNU Grafisk senter

Abstract

Economic development has gradually promoted an increase in the demand for and size of long-span bridges worldwide. A tangible example of such development is the Coastal Highway Route E39 led by the Norwegian Public Roads Administration (NPRA). The project proposes the construction of a 1000 km ferry-free highway from the cities of Kristiansand to Trondheim, including 8 major fjord crossings spanning from 1300 to 5000 m at water depths from 500 to 1250 m. The longest, single-span suspension bridge planned within the project is the 3000 m bridge across Sulafjord in the county of Møre og Romsdal in western Norway. The project has encouraged several research studies from which this thesis takes off.

Structures such as the Sulafjord Bridge pose a major challenge to the existing technologies of bridge construction. As bridges become longer, they become more flexible and susceptible to wind loading. However, wind loading and its effects are often oversimplified in most of the current design guidelines. Some of these simplifications may be acceptable for designing regular structures but are unaccurate for long-span bridges. Recent experience based on full-scale measurements has shown discrepancies between the observations and available analytical formulations. Therefore, the need to revaluate the design guidelines is exposed. Existing research has pointed out the omission of the stochastic behaviour of the structural response and wind turbulence as the main reason for these discrepancies. Alternatively, full long-term analysis is recognized as the most accurate way to evaluate the stochastic behaviour of the structural response given the fluctuations of the environmental conditions during the lifetime of a structure. Nevertheless, the traditional full long-term analysis is based on numerical integration and requires the evaluation of the short-term response statistics from several environmental states. This requirement renders the approach unfeasible for practical engineering applications such as the Sulafjord Bridge.

The objective of this thesis is to propose a reliable and computationally efficient, full long-term framework for the wind-resistant design of long-span bridges. The Sulafjord Bridge was selected as a case study. Although the results are site-specific, the framework can be easily extended to similar projects given that site-specific data are available, which is the case for most projects of this magnitude. The thesis is composed of a collection of papers, each of which accomplishes a portion of the general objective. The first paper shows surrogate modelling strategies to reduce the computational effort in the estimation of the short-term statistics of the wind responses given a wind state. Conversely, the paper applied the data of the Hardanger Bridge as the accuracy of the surrogate modelling was compared with full-scale, measured bridge responses (not available at Sulafjord). The second paper presents the wind characterization of the Sulafjord site with the environmental contour method and a probabilistic model of wind turbulence. The third paper presents a full long-term analysis of the extreme response and compares the results with the existing methods utilized in the design guidelines. In this paper, we also proposed a framework to reduce the computational effort of the full long-term analysis by replacing the traditional analysis based on numerical integration with importance sampling Monte Carlo (ISMC) simulations. The fourth and final paper combines the strategies of surrogate modelling and importance sampling Monte Carlo simulations to enhance the efficiency of full long-term analysis.

The results of this thesis showed that environmental contours were the most efficient strategy for representing the characterization of the wind conditions at the Sulafjord Bridge site. The contours captured the variability measured wind turbulence and provided a more complete and yet intuitive description of the wind field compared with the current design methodology. Extreme responses from the environmental contours were on average 14% higher than the common practice based on the short-term method. The surrogate modelling strategy was a very accurate alternative for estimating the short-term statistics. The models evaluated in this thesis showed a complementary mean absolute percent error (1-MAPE) of 98% compared with analytical predictions of the buffeting response, and the full long-term framework based on the surrogate model required less than 1% of the computational effort of the traditional full long-term analysis. The most important finding of this thesis is that the extreme response from the full long-term analysis was on average more than 25% larger than the traditional short-term methodology.

Acknowledgements

I dedicate this work to my son. I hope that this research inspires you to achieve your goals in life. Nonetheless, I regret every moment that I missed with you while I was away. Hopefully, we will not be apart anymore. I also thank Yamile Aponte for being such an important source of support during this period. Herminia Castellon was also invaluable; thank you for always listening to me during our phone conversations. This work is for you. Your efforts supported me during the dark nights and tough winters.

To my supervisor Ole Øiseth, I sincerely thank you for your guidance and patience. I learned many valuable lessons from you, and I will treasure them during my journey. To my work team, Aksel Fenerci and Øyvind Petersen, I am thankful for the positive comments and your commitment to my work without any expectation of retribution.

I thank the dynamics group for their help and wonderful conversations during the coffee breaks. To my officemate Maria, thank you for the music that we played. To Anno and Sebastian, thank you for training me to achieve one of my side goals of completing a triathlon. To Niccolo, Gabriel and Oddbjørn, thank you for listening to me and showing me the qualities of a good friendship. To the other team members, Anders, Stefano, Bjørn, Gunnstein, Tor Martin, Knut, Bartoz, MingJie, Teng Jiao, and the remainder of the community in the structural department, thank you for the amazing working environment.

Preface

This thesis is submitted in partial fulfilment of the requirements for the degree Philosophiae Doctor at the Norwegian University of Science and Technology (NTNU). The work has been carried out at the Department of Structural Engineering, Faculty of Engineering and with financial support from the Norwegian Public Road Administration (NPRA). Professor Ole Andre Øiseth, Associate Professor Aksel Fenerci and researcher Øyvind Wiig Petersen supervised the work.

This thesis is composed of a collection of four papers, either published or submitted to international peer-reviewed scientific journals, and the following introductory part.

Dario Rafael Fernandez Castellon
Trondheim, Norway
March 2022

List of appended papers

I. [1] Castellon D, Fenerci A, Øiseth O. A comparative study of wind-induced dynamic response models of long-span bridges using artificial neural networks, support vector regression and buffeting theory. J. Wind Eng. Ind. Aerodyn., vol. 209, p. 104484, 2021, doi: https://doi.org/10.1016/j.jweia.2020.104484.

II. [2] Castellon D, Fenerci A, Øiseth O. Environmental contours for wind-resistant bridge design in complex terrain. J. Wind Eng. Ind. Aerodyn., vol. 224, p. 104943, 2022, doi: 10.1016/j.jweia.2022.104943.

III. [3] Castellon D, Fenerci A, Øiseth O, Petersen Ø. Investigations of the long-term extreme buffeting response of long-span bridges using importance sampling Monte Carlo simulations. Submitted for Journal publication.

IV. [4] Castellon D, Fenerci A, Øiseth O, Petersen Ø. Full long-term buffeting analysis of suspension bridges using Gaussian process surrogate modelling and importance sampling Monte Carlo simulations. Submitted for Journal publication.

Other scientific contributions

I. [5] D. F. Castellon, A. Fenerci, and O. A. Øiseth, "A study on the evaluation of wind induced vibration of long-span suspension bridges with artificial neural networks," Proc. Int. Conf. Struct. Dyn., EURODYN, vol. 1, no. June, pp. 1958–1967, 2020.
II. [6] D. F. Castellon, Aksel Fenerci, and O. Øiseth, "A PROBABILISTIC ANALYSIS OF THE WIND FIELD AT SULAFJORDEN BRIDGE SITE," in *ANCRiSST:14th International Workshop on Advanced Smart Materials and Smart Structures Technology*, 2019, pp. 115–118, [Online]. Available: https://doi.org/10.13133/9788893771146.
III. D. F. Castellon, A. Fenerci, and O. A. Øiseth, "Estimation of extreme buffeting response in long-span bridges with Environmental Contour Method". Submitted to conference publication 8EACWE: 8th European African Conference on Wind Engineering.

CONTENT

Abstract i

Acknowledgments ii

Preface iii

List of appended papers iv

Other scientific contributions v

1 Introduction 1

1.1 Background and motivation 1

1.2 Objectives and scope 2

1.3 Workflow and structure of the thesis 3

2 Sulafjord monitoring system 5

2.1 Local topography 5

2.2 Monitoring system 6

3 Wind turbulence model 7

3.1 Probabilistic model 9

4 Buffeting response of long-span bridges 10

4.1 Theoretical estimation of buffeting response with the Multi-modal approach 10

4.2 Approximate estimation of buffeting response with machine learning 13

5 Extreme response estimation 18

5.1 Short-term method 18

5.2 Environmental contour method 19

5.3 Full long-term analysis 22

6 Summary of the appended papers 27

6.1 Declaration of Authorship 27

6.2 Paper 1 27

6.3 Paper 2 27

6.4 Paper 3 28

6.5 Paper 4 28

7 Conclusions 29

8 Future research 29

9 References 30

1 Introduction

1.1 Background and motivation

1.1.1 Long-span bridges

Infrastructure development is a key factor for economic growth. Continuous commercial expansion worldwide has promoted an unprecedented increase in the demand for long-span bridges (with a main span greater than 150 m) [7]. Globally, the United States has the largest number of long-span bridges (245), followed by China, with 98 long-span bridges and 23 long-span bridges, respectively, under construction. In the European scene, Norway leads with 51 long-span bridges [7]. The increase in number is followed by an increase in scale; since the 19th century, the main span of the world's longest bridge has doubled approximately every 50 years [8]. Cable-supported bridges are the most suitable bridge type to cover the long main spans, with the suspension bridge being the principal configuration of the longest-span bridges [9]. Currently, the longest single-span bridge is the Çanakkale 1915 Bridge in Turkey (2022), which is a suspension bridge with a 2023 m main span. The increase in the scale of long-span bridges constantly challenges the existing technologies of bridge construction. As these structures become slender and more flexible, they also become more susceptible to wind vibrations.

The design of long-span bridges is governed by wind loading and wind loading effects. Long-span bridges are flexible structures with low structural damping and relatively light weight [9]. Therefore, the natural frequencies of their principal modes are very low, overlapping with the frequencies where the wind spectrum encloses most of its energy. The engineering community is well aware of bridge aerodynamics, and sophisticated models are well documented in the literature [10]–[16].

On the other hand, wind loading effects are often simplified in the design guidelines. Wind actions in bridges are considered with their characteristic values associated with a design return period. Most of the wind resistance design guidelines assume the return period of the characteristic response to be equivalent to the return period of the mean wind speed [17], [18]. Such an assumption may not be accurate because of the inherent stochastic behaviour of the structural responses due to wind fluctuations. In addition, the variation in the wind turbulence field is generally disregarded, as the common practice is to define the turbulence parameters from deterministic relationships based on the mean wind speed only. The combinations of these assumptions may cause underestimations of the actual design response in long-span bridges, exposing the need to revaluate the design guidelines and to propose more reliable alternatives to the wind-resistant design of long-span bridges [19], [20].

1.1.2 Sulafjord

The financial progress of Norway has promoted the development of several infrastructure projects. Nevertheless, the country has mountainous topography characterized by the presence of fjords, leaving important economic regions such as the Norwegian western coast separated by these massive inlets of sea water. In an effort to connect the main cities of the Norwegian western coast, the Norwegian Public Roads Administration (NPRA) started the Coastal Highway Route E39. The project proposes the construction of a 1000 km ferry-free highway from the cities of Kristiansand to Trondheim [21]. The project includes 8 major fjord crossings spanning from 1300 to 5000 m at water depths from 500 to 1250 m [22]. The development of such projects has stimulated a vast research effort, including novel concepts such as submerged tunnels and floating bridges, as well as improvements in the design techniques for cable-supported bridges.

From the crossings considered in E-39, the longest solution planned with a suspension bridge is the Sulafjord crossing. The Sulafjord Bridge is projected to be a 3000 m main span suspension bridge standing across the villages of Hareid in the west and Sula in the east in the vicinity of Ålesund. Figure 1 shows the Sulafjord suspension bridge adapted from illustrations by the NPRA [23]. This bridge will serve as a case study given its large scale, which makes it extremely susceptible to wind loading effects. The project has driven an immense research effort, including studies to enhance buffeting response calculations [24], [25], conceptual designs, wind tunnel testing, and meteorological observations [26], [27]. To date, the greatest part of the research effort has been dedicated to the wind monitoring campaign of Sulafjord. Since 2014, a set of meteorological masts have been erected in strategic points along the Sulafjord channel, and the masts carry sensors to observe and register the wind conditions. The campaign is planned to last 8 years with a possible extension to 12 years. The recordings from the campaign are open to the public and have been carefully investigated in the content of this thesis to characterize the wind conditions of the Sulafjord site and to propose more reliable alternatives to wind resistant design based on the expected behaviour of wind at the site.

Figure 1: Illustration of the Sulafjord suspension bridge. (Image courtesy of NPRA)

1.2 Objectives and scope

1.2.1 Research objectives

This work aims to develop methods for wind field characterization and extreme response prediction of long-span bridges that take into account the probability distribution of the wind field parameters and the extreme response. There is a particular emphasis on developing a methodology that predicts response with enhanced accuracy but with reasonable computational effort.

The following research objectives are defined to achieve this goal:

- **Test the feasibility of using a probabilistic model of wind field parameters to characterize the wind conditions at the Sulafjord Bridge site.** The topography at the Sulafjord Bridge site strongly affects the wind conditions. An accurate description of the wind variables, including their variability under extreme conditions, is required to ensure a reliable design of the Sulafjord Bridge.

- **Investigate the improvement in safety provided by including the variability of the wind turbulence in the buffeting response calculations.** The scatter in the measured buffeting response of long-span bridges with respect to the analytical models is partially attributed to inaccurate assumptions in the current guidelines, which disregard the variability of the wind field. Therefore, the stochastic behaviour of the turbulence parameters is included in the modelling to investigate its effect on the design buffeting response.

- **Explore the validity of surrogate modelling techniques based on machine learning for buffeting response estimations.** Calculating the buffeting response involves computationally demanding procedures, which can be challenging to handle when several analyses are needed. On the other hand, machine learning models alleviate the computational demand by learning the underlying relation between wind variables and the buffeting response. In this thesis, the accuracy of such methods is tested and compared with data from full-scale measurement campaigns on long-span bridges.

- **Compare the design buffeting response from full long-term and short-term analysis.** Full long-term analysis is the most accurate methodology to estimate extreme responses. However, the method is not widespread in the design practice of wind engineering. Therefore, this study presents the buffeting response of a long-span bridge in the design phase with full long-term analysis and simplified methodologies, such as the environmental contour method and the short-term approach. The difference in the response from the different methods is analysed to investigate the reliability of the simplified methods.

- **Develop an efficient, full long-term framework for estimating the design buffeting response of long-span bridges.** The required computational effort is a major weakness of the full long-term analysis. Despite the literature offering approximations to reduce such demand, the approximate methods do not converge to the exact solutions. Therefore, an alternative methodology based on importance sampling is investigated to determine a more efficient way to carry out the full long-term analysis. The framework was further enhanced by introducing a surrogate model of the buffeting response, reducing the time required to estimate the short-term response statistics.

1.2.2 Scope of the thesis

The Sulafjord Bridge was used as a case study. The methodology could be easily extended to any other bridge site given that monitoring data are available. Nevertheless, the results cannot be generalized without proper site-specific investigations. Only data from the metallic mast stations of the measurement campaign were analysed in this thesis. Additional measurement information from floating buoys and lidar was not included.

This study is focused only on wind buffeting effects, i.e., vibrations in the structure due to the turbulence of the wind field. Other aerodynamic phenomena, such as instability due to galloping, flutter or vortex-induced vibrations, are beyond the scope of this thesis. The wind conditions are averaged in short-term intervals of 10 minutes. The wind field is assumed to be stationary and Gaussian in each interval. The winds are assumed to impact the bridge orthogonal to the longitudinal axis, and the variation in the angle of attack is not considered significant (linear model). Buffeting response analysis is performed in the frequency domain. Therefore, nonstationary and non-Gaussian wind loading and wind loading effects, skew winds and nonlinearities due to the constitutive law of the material, geometric stiffness, instabilities or excessive angles of attack are considered beyond the scope of the thesis. Admittance functions are taken as unity, and crosswind turbulence components and the correlation between vertical turbulence and along-wind turbulence are disregarded due to their low effect on the final buffeting response.

Regarding the proposed framework for long-term analysis, the following finding is valid. In surrogate modelling with machine learning, the hyperparameters are optimized using the machine learning and statistics toolbox of MATLAB. On the other hand, in the full long-term framework based on importance sampling, samples were considered uniformly distributed. The methods for hyperparameter optimization and the effects of other importance sampling distribution functions are considered beyond the scope of this thesis.

1.3 Workflow and structure of the thesis

The workflow of the analysis is presented as follows: First, the wind conditions are characterized by a probabilistic modelling approach. Second, the buffeting response is computed for each wind condition with either the multimode approach or a surrogate model based on machine learning. The extreme buffeting response is then obtained with the short-term method, the environmental contour method, or the full long-term analysis. Figure 2 shows the workflow diagram of the thesis.

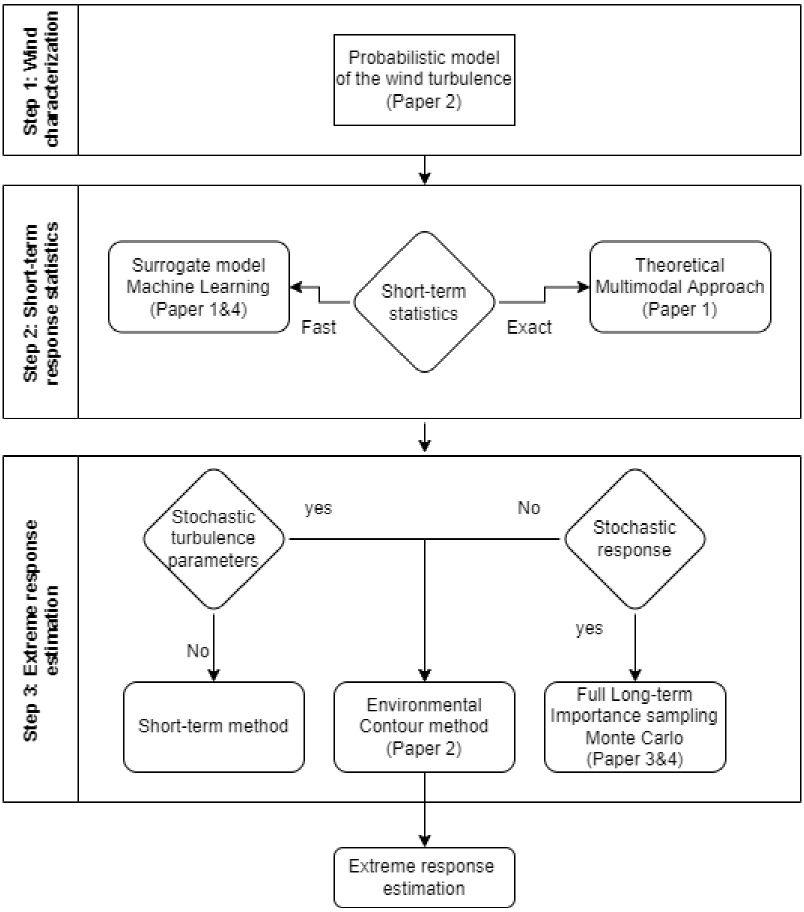

Figure 2: Workflow of the thesis

The synopsis is organized to explain each step of the workflow. Section 2 shows the Sulafjord site and monitoring campaign. Section 3 shows the wind turbulence considerations and the probabilistic modelling. Section 4 shows the buffeting response calculations based on the multimodal approach and surrogate modelling. Section 5 provides the design buffeting response with the short-term method, environmental contour method, and full long-term analysis. In addition, the collection of papers that compound this thesis can be grouped into the following topics:

- Short-term statistics of the buffeting response with the multimodal approach and machine learning surrogate models (Paper 1).
- Wind characterization and probabilistic model of the Sulafjord Bridge site (Paper 2).
- Full long-term estimation of the design buffeting response (Paper 3 & 4).
- Enhanced full long-term analysis (Paper 4).

2 Sulafjord monitoring system

2.1 Local topography

Sulafjord is located on the western coast of Norway 10 km southwest of Ålesund. The fjord is oriented from southeast to northwest, is approximately 12 km long and 4 km wide and has a maximum water depth of 450 m. The fjord is surrounded by steep mountains with an elevation between 500 and 700 m from both sides. Figure 3 shows the surroundings and topography of the fjord. The mountainous topography of the area directs the wind flow through the fjord. Figure 4 shows a picture of the fjord surroundings from the bridge location towards the north and south. Figure 4 a) also shows the island Godøya, which is located on the northern side of the fjord. The island partly shields the fjord from the winds coming directly from the sea [6].

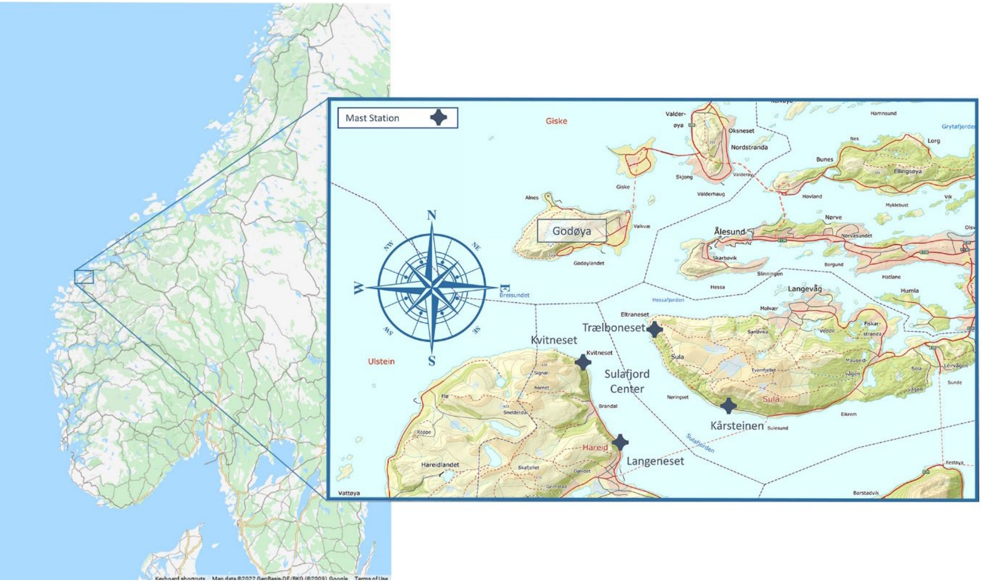

Figure 3: Topographical map of the Sulafjord site (adapted from https://norgeskart.no/- ®norgeskart Norwegian Mapping Authority)

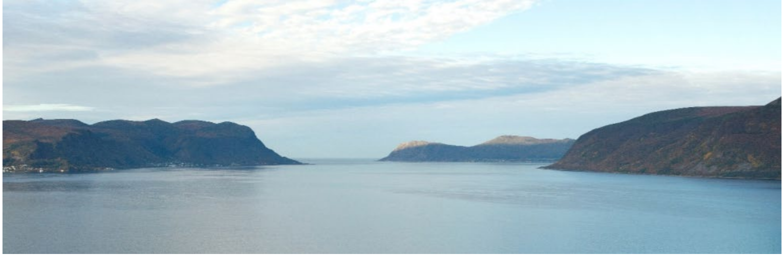

a) North view

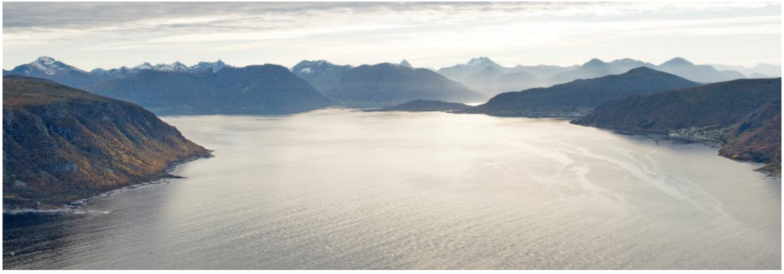

b) South view

Figure 4: Bridge site. (Images courtesy of NPRA)

The principal environmental loading on the long-span suspension bridge across Sulafjord will be the wind action. Therefore, a wind measurement campaign has been deployed in the area. The measurement campaign is managed by the Norwegian Public Road Administration (NPRA) and operated by Kjeller Vindteknikk (KVT). The observations from the campaign are open to the public through the Norwegian Meteorological Institute (MET Norway). The campaign measurements are carried out at four strategic locations near both ends of the two possible fjord crossings, Kvitneset to Trælbonset on the northern side and Langeneset to Kårsteinen on the southern side. Each location is composed of a metallic mast structure that holds anemometers at different heights. Figure 3 shows the locations of the metrological stations. The elevation profiles of the two alternative crossing tracks are shown in Figure 5. The figure highlights the steepness and height of the surrounding mountains.

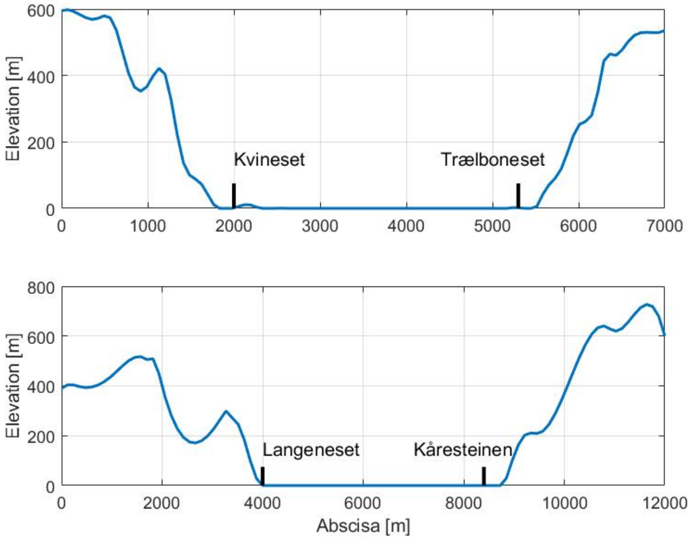

Figure 5: Terrain profiles at possible fjord crossings

The shortest track for the Sulafjord Bridge is between the stations of Kvitneset and Trælboneset (Figure 3). Most of the content of this thesis derived from observations made at these stations. Kvitneset is located northeast of the island Hareidlandet. The mast is open to the Norwegian Sea in the west-northwest to north-northwest sector. The immediate terrain leading to the station is relatively flat, but within a distance less than 1 km southwest, there is a steep mountain with a height greater than 500 m. On the other side of the fjord, on a small cliff of the western side of Sula, Trælbodneset is located. The island Godøya in the north blocks most of the winds coming from the Norwegian Sea at this location. The terrain near the station is steep, with the abrupt presence of a 450 m tall mountain towards the east immediately after the mast.

The other possible design alternative is to build the bridge from Langeneset to Kårsteinen (Figure 3). This track is closer to populated areas and spans the exiting ferry route. Langeneset is located inwards from Sulafjord many kilometres south from Kvitneset. The mast is erected in an industrial area a few metres from the mountain side. Kårsteinen is located on a small cliff in the vicinity of a steep mountain with a height of approximately 660 m. The mast is located near the opening of Sulafjorden into Vartdalsfjord. The principal directions of the wind at this station are aligned with the axis of both fjords.

2.2 Monitoring system

Each mast is equipped with 3 to 4 wind sensors at different heights to capture the vertical wind profile. Table 1 reports the geographical coordinates of the stations, the initial date of recording, the number of sensors and their height above sea level. Observations are still ongoing at the moment of writing this thesis. The sensors employed are WindMaster Pro 3-Axis anemometers (Gill Instruments Limited), which can measure maximum wind gusts of 65 m/s. The speed resolution is 0.01 m/s, and the direction resolution is 0.1°, while the accuracy at 12 m/s is reportedly <1.5% RMS and 2° for speed and direction, respectively. The sensors installed before October 2015 were affected by the software bug reported in [28]. To date, this error has accounted for all the measurements of the dataset. The wind speed observations from the anemometers are divided into recordings of 10-minute intervals. Subsequently, the statistical properties of these recordings are analysed to characterize the site-specific wind conditions. The data availability of 10-min intervals from all stations is estimated to exceed 98.9% with punctual losses due to instrument or logger failure. Reports of data availability by station are provided in [26].

Station name	Latitude	Longitude	Initial date of recording	Sensors	Altitude (m)
Kvitneset	62°25'17.74"N	6° 0'4.03"E	2016-11-24	3	92.5, 71.5, 44.5
Trælboneset	62°25'39.47"N	6° 3'45.45"E	2018-01-03	3	76.8, 48.3, 27.3
Langeneset	62°23'10.68"N	6° 1'52.72"E	2017-04-26	4	94.8, 75, 50, 27
Kårsteinen	62°24'0.48"N	6° 7'9.82"E	2017-12-04	3	62.8, 40, 13.4

Table 1: Sulafjord wind mast station coordinates

3 Wind turbulence model

The observations from the monitoring campaign reveal that Sulafjord Bridge will be exposed to strong European windstorms. Therefore, the dynamic response of the bridge is expected to be governed by the action of wind gusts, i.e., fluctuations in the wind speed. The usual approach to model the effect of gusts is to decompose the wind velocity into the mean wind field (speed and direction) and the three orthogonal turbulent components—the along-wind (aligned with the mean), crosswind (orthogonal to the mean) and vertical components. The crosswind turbulent component is disregarded in the analysis because of its negligible contribution to the buffeting response due to the relatively high axial stiffness of the bridge girder. The action of the turbulence in the modelling is represented with its cross-spectral density ($S_{uu,ww}$) composed of the one-point autospectral density ($S_{u,w}$) and normalized cross spectrum ($C_{uu,ww}$). The cross-spectral densities are then arranged in matrix format as follows (S_V):

$$S_V(x_1, x_2, \omega) = \begin{bmatrix} S_{uu}(x_1, x_2, \omega) & S_{wu}(x_1, x_2, \omega) \\ S_{uw}(x_1, x_2, \omega) & S_{ww}(x_1, x_2, \omega) \end{bmatrix} \tag{1}$$

$$S_{uu,ww}(x_1, x_2, \omega) = \sqrt{S_{u,w}(x_1, \omega) S_{u,w}(x_2, \omega)}\, C_{uu,ww}(\Delta x, \omega)$$

where x_1, x_2 are the coordinates of two points separated by the distance Δx and $\omega = 2\pi f$ is the circular frequency.

The autospectral density shows how the energy of the wind turbulence is distributed along its frequency content. The autospectral densities extracted directly from the wind recordings contain fluctuations. The usual engineering approach is to approximate them with a smooth curve [29]. The literature offers a substantial number of models to approximate such behaviour [30]–[40]; the reader is referred to Solari et al. for a more comprehensive comparison of the models [41], [42]. Since the focus of this research is to improve the design guidelines of long-span bridges, the spectral density fitting used in the Norwegian handbook for bridge design (N400) [18] will be employed. The expression is derived from the Kaimal-type spectrum [43]:

$$\frac{S_{u,w} f}{\left(V\, I_{u,w}\right)^2} = \frac{A_{u,w} f_{z_h}}{\left(1 + 1.5 A_{u,w} f_{z_h}\right)^{5/3}}, f_z = \frac{z_h f}{V}, I_u = \frac{\sigma_{u,w}}{V} \tag{2}$$

where V denotes the mean wind speed, $I_{u,w}$ represent the along-wind and vertical turbulence intensities, $A_{u,w}$ indicate the spectral parameters relative to the integral length scales and z_h denotes the reference height. Overlapping fitted and measured power spectra from a recording registered on 01.01.19 at Trælboneset station from 14:40 to 14:50, which correspond to the annual highest mean speed, are shown in Figure 6.

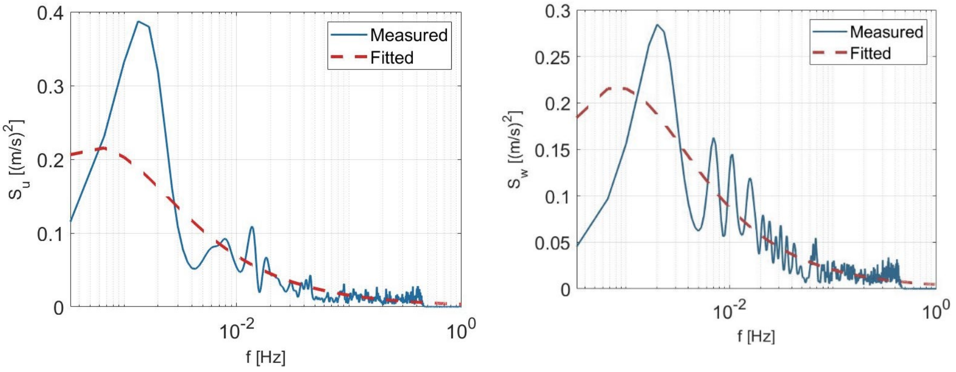

a) Along-wind turbulence autospectra b) vertical turbulence autospectra

Figure 6: Two components of the one-point spectrum 'max 2019' Record 01.01.19 from 14:40 to 14:50. a) Su b) Sw

The normalized cross-spectrum gives the correlation between two points along the structure. The cross-spectrum is a complex quantity whose imaginary part is usually disregarded for perpendicular winds [44]. The real part is known as the normalized co-spectra; this quantity is influenced by the frequency and distance between the analysed points. The correlation assumes values from -1 to 1, where 1 represents a perfect correlation. The literature has several models to define this quantity [33], [40], [45]–[47]. Nevertheless, an exponentially decaying curve based on the Davenport decay coefficients (K_u, K_w) is the simplest expression that matches the data observations [48]. The cross term C_{uw} is disregarded in the analysis due to its low contribution to the measured buffeting response of the bridges [49].

$$C_{u,w}(f, \Delta x) = \exp\left(-K_{u,w} \frac{\Delta x\, f}{V}\right) \tag{3}$$

3.1 Probabilistic model

The parameters of the turbulence are often defined from deterministic relationships of the mean wind speed. Nevertheless, experience from full-scaled measurements of the buffeting response on long-span bridges has shown discrepancies between the observations and the analytical models. Such discrepancies are partially attributed to the variability of the wind turbulence field, which is disregarded in the analytical models [50]–[57]. Therefore, the stochastic behaviour of the wind turbulence parameters was considered in the analysis. The turbulence parameters included in modelling are the along-wind and vertical turbulence intensities ($I_u,\ I_w$), the spectral parameters (A_u, A_w) and decay coefficients (K_u, K_w). Probabilistic modelling of the wind field was introduced to handle stochastic behaviour [20], [51]. Introducing $\boldsymbol{W}$ as the wind state vector collecting the wind parameters, its joint cumulative distribution function (CDF) can be expressed as the product of the conditional distributions:

$$F_{\boldsymbol{W}}(W) = F_V(V) * F_{I_u,I_w,A_u,A_w,K_u,K_w|V}\,(I_u, I_w, A_u, A_w, K_u, K_w|V) \tag{4}$$

$$\boldsymbol{W} = [\,V, I_u, I_w, A_u, A_w, K_u, K_w]$$

Fenerci et al. (2018) showed that the joint distribution can be expressed as the product of the Weibull distribution of the mean wind speed and a joint lognormal distribution of the turbulence parameters. The same distribution types will be utilized for the Sulafjord Bridge in this thesis. The expressions for the Weibull and joint lognormal distributions are presented as follows:

$$F_V(V) = 1 - \exp\left[\left(\frac{V}{\lambda}\right)^k\right] \quad ;\ for\ V > 0 \tag{5}$$

$$f_{logn}(x|\tilde{\mu}, \tilde{\sigma}) = \frac{1}{x\tilde{\sigma}\sqrt{2\pi}} exp\left\{\frac{-(Ln\ x - \tilde{\mu})^2}{2\tilde{\sigma}^2}\right\}$$

$$\tilde{\mu} = exp\left(\mu + \frac{\sigma^2}{2}\right),\ \tilde{\sigma}^2 = [exp(\sigma^2) - 1]\ exp\ (2\mu + \sigma^2)$$

$$\rho(x, y) = \frac{1}{N-1}\sum_{i=1}^{N}\left(\frac{x_i - \mu_x}{\sigma_x}\right)\left(\frac{y_i - \mu_y}{\sigma_y}\right) \tag{6}$$

$$\boldsymbol{R}_{xy} = \begin{bmatrix} 1 & \rho(x, y) \\ \rho(y, x) & 1 \end{bmatrix}$$

where $k\ and\ \lambda$ are the shape parameter and scale parameter, respectively, of the Weibull distribution and $f_{logn}(x|\tilde{\mu}, \tilde{\sigma})$ is the lognormal distribution of x. $\tilde{\mu}, \tilde{\sigma}$ are the lognormal mean and standard deviation, $\rho(x, y)$ is the correlation coefficient of the variables $x\ and\ y$, and $\boldsymbol{R}_{xy}$ is the correlation matrix. The parameters of the distributions were adapted from the site-specific data following the procedure explained in paper 2 of this thesis.

4 Buffeting response of long-span bridges

4.1 Theoretical estimation of the buffeting response using the Multimodal approach

Wind actions over long-span bridges can be critical if not considered properly [11], [16]. This study is focused on wind buffeting effects, i.e., vibrations in the structure due to the turbulence of the wind field. Other aerodynamic phenomena, such as instability due to galloping, flutter or vortex shedding, are beyond the scope of this thesis, with a special notation over flutter stability limits, which are estimated only to avoid the simulation of wind states outside the assumptions of the modelling.

The analysis of cable-supported bridges under the action of stochastic wind loading was introduced by Davenport [10], [48], [58]. Davenport's formulations proposed a spectral analysis in the frequency domain, which is exact and therefore will be the approach used in this thesis. Approximated analysis in the time domain is beyond the scope of this thesis. Since Davenport's original formulation, several authors have contributed to improving the modelling, and the discussion is still open in the literature. In this thesis, the buffeting response was computed in the frequency domain following the multimodal approach based on finite element formulation. The modelling contemplates the following assumptions: the bridge deck is idealized as a line-like structure; the wind field is homogenous; wind turbulence is a Gaussian and stationary process; the mean wind is orthogonal to the bridge longitudinal axis (no skew winds) and variations in the vertical angle of attack are not significant. Self-excited forces are accounted for with aerodynamic derivatives [59]. Modal coupling is considered with the multimodal approach [60]–[68]. The wind aerodynamic forces are applied to the structural elements following the discretization of the bridge finite element model [1].

Aerodynamic loading and loading effects are decomposed using the mode shapes of the finite element model as generalized coordinates. Denoting the mode shapes with $\boldsymbol{\Phi}$ and the respective generalized coordinates with $\boldsymbol{\eta}$, the global displacement vector due to buffeting actions $\boldsymbol{r}$ is:

$$\begin{aligned} &\boldsymbol{r}(x,t) = \boldsymbol{\Phi}(x)\boldsymbol{\eta}(t) && \boldsymbol{r}(x,t) = [\,\boldsymbol{r_y}\,\boldsymbol{r_z}\,\boldsymbol{r_\theta}]^T \\ &\boldsymbol{\Phi}(x) = [\,\boldsymbol{\varphi_1} \dots \boldsymbol{\varphi_i} \dots \boldsymbol{\varphi_N}]^T && \boldsymbol{\eta}(t) = [\,\boldsymbol{\eta_1} \dots \boldsymbol{\eta_i} \dots \boldsymbol{\eta_N}]^T \\ & && \boldsymbol{\varphi_i} = [\,\boldsymbol{\varphi_y}\,\boldsymbol{\varphi_z}\,\boldsymbol{\varphi_\theta}]^T \end{aligned} \tag{7}$$

where x is the coordinate of the nodes over the line-like deck; $y, z\ and\ \theta$ are the lateral, vertical and torsional displacement components; and N is the number of modes considered.

The equation of motion of the system in the frequency domain using the generalized coordinates is:

$$\widetilde{\boldsymbol{M}}_0\, G_{\ddot{\boldsymbol{\eta}}}(\omega) + (\widetilde{\boldsymbol{C}}_0 - \widetilde{\boldsymbol{C}}_{ae})\, G_{\dot{\boldsymbol{\eta}}}(\omega) + (\widetilde{\boldsymbol{K}}_0 - \widetilde{\boldsymbol{K}}_{ae}) G_{\boldsymbol{\eta}}(\omega) = G_{\boldsymbol{Q}_{buff}}(\omega) \tag{8}$$

where $\widetilde{\boldsymbol{M}}_0, \widetilde{\boldsymbol{C}}_0$ and $\widetilde{\boldsymbol{K}}_0$ are the generalized mass, damping and stiffness matrices, respectively, under still-air conditions. These structural matrices are obtained from the finite element model of the bridge under mean wind actions. $\widetilde{\boldsymbol{C}}_{ae}$ and $\widetilde{\boldsymbol{K}}_{ae}$ are the generalized aeroelastic stiffness and damping matrices, respectively, from the self-excited motion. $G_{\ddot{\boldsymbol{\eta}}}, G_{\dot{\boldsymbol{\eta}}}$and $G_{\boldsymbol{\eta}}$ are the Fourier transforms of the generalized acceleration, velocity, and displacement, respectively, and $G_{\boldsymbol{Q}_{buff}}$is the Fourier transform of the nodal buffeting forces.

The aeroelastic damping C_{ae} and stiffness K_{ae} in global coordinates are:

$$C_{ae} = \frac{1}{2}\,\rho\,\omega B^2 \begin{bmatrix} P_1^* & P_5^* & BP_2^* \\ H_5^* & H_1^* & BH_2^* \\ BA_5^* & BA_1^* & B^2A_2^* \end{bmatrix} \tag{9}$$

$$K_{ae} = \frac{1}{2}\,\rho\,\omega^2 B^2 \begin{bmatrix} P_4^* & P_6^* & BP_3^* \\ H_6^* & H_4^* & BH_3^* \\ BA_6^* & BA_4^* & B^2A_3^* \end{bmatrix} \tag{10}$$

where $P_{1,2\ldots,6}^*$ $H_{1,2\ldots,6}^*$ and $A_{1,2\ldots,6}^*$ denote the dimensionless aerodynamic derivatives, ρ is the density of the air and B is the effective width of the bridge deck. The matrices in generalize coordinates are:

$$\widetilde{\boldsymbol{C}}_{ae}(V,\omega) = \int_L \boldsymbol{\Phi}_n^T C_{ae}(V,\omega)\boldsymbol{\Phi}_m \; dx \tag{11}$$

$$\widetilde{\boldsymbol{K}}_{ae}(V,\omega) = \int_L \boldsymbol{\Phi}_n^T K_{ae}(V,\omega)\boldsymbol{\Phi}_m \; dx \tag{12}$$

4.1.1 Buffeting forces from beam finite element formulation

To apply the wind forces in the model, a beam finite element discretization approach was selected. A generic structure can be discretized with beam finite elements with 12 degrees of freedom, as shown in Figure 7 (a). Next, the wind action over a generic beam element is shown in Figure 7 (b). The three coordinate systems shown in Figure 7 comprise the global coordinate system defined by its unit vector $\{E_1, E_2, E_3\}$, the beam element local coordinate system with unit vector $\{e_1, e_2, e_3\}$ and the wind field system with unit vector $\{ev_1, ev_2, ev_3\}$. The transformation scheme from the wind reference system to the local reference system of the beam elements is presented as follows:

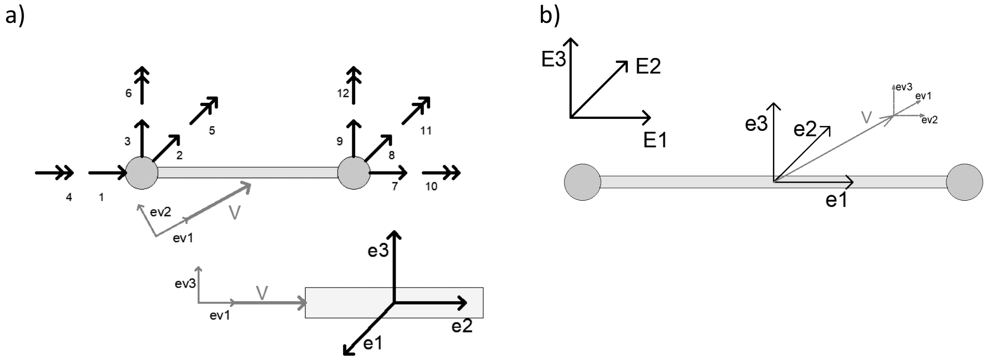

Figure 7: Local coordinate system of the beam element: a) DOF of the beam element. b) Wind actions on the beam element

$$T_{G2Le} = \begin{bmatrix} e_1^T \\ e_2^T \\ e_3^T \end{bmatrix} \tag{13}$$

$$T_{G2Lw} = \begin{bmatrix} ev_1^T \\ ev_2^T \\ ev_3^T \end{bmatrix} \tag{14}$$

$$T_{Lw2Le} = T_{G2Le}\, T_{G2Lw}^T \tag{15}$$

The vector of nodal buffeting forces ($\boldsymbol{Q}_{Le_{buff}}$) is obtained from the principle of virtual work using the shape functions $N(x)$ and denoting the wind forces in the beam element by $q_{buff}(x,t)$

$$\boldsymbol{Q}_{Le_{buff}}(t) = \int_0^L \boldsymbol{N}(x) q_{buff}(x,t)dx \tag{16}$$

$$q_{buff}(x,t) = \boldsymbol{B}_q(x)\boldsymbol{T}_{Lw2Le}\, \boldsymbol{V}_{Lw}(x,t)$$

where $\boldsymbol{V}_{Lw} = [v_1 \quad v_2 \quad v_3]^T$ is the vector that contains the wind turbulence components in the wind reference system. The matrix T_{Lw2Le} transforms the wind coordinates into the local element reference system. The aerodynamic matrix B_q contains the force coefficients that relate the turbulence components to the aerodynamic forces:

$$\boldsymbol{B}_q = \frac{1}{2}\rho B\, V \begin{bmatrix} 0 & 0 & 0 \\ 0 & 2\left(\frac{D}{B}\right)\bar{C}_D & \left\{\left(\frac{D}{B}\right)C'_D - \bar{C}_L\right\} \\ 0 & 2\bar{C}_L & \left\{\left(\frac{D}{B}\right)\bar{C}_D + C'_L\right\} \\ 0 & 2B\bar{C}_M & BC'_M \end{bmatrix} \tag{17}$$

where D is the effective depth of the girder cross-section; $\bar{C}_D, \bar{C}_L$ & $\bar{C}_M$ are the mean values of the drag, lift and moment steady-state force coefficients, respectively; and C'_D, C'_L, C'_M are their respective derivatives with respect to the angle of attack.

The nodal buffeting forces from all the elements are assembled. The dependence of element buffeting forces along the geometric coordinate x from Equation (16) is disregarded, assuming a uniform shape of the beam elements and assuming that the length of the beam elements is small compared with the size of the eddies. The global buffeting force is then:

$$\boldsymbol{Q}_{buff}(t) = \sum_i^N \boldsymbol{T}_{E2S,i}\, \boldsymbol{T}_{G2Le,i}^{\boldsymbol{T}}\, \bar{N}_i \boldsymbol{B}_{q,i} \boldsymbol{T}_{Lw2Le,i}\, \boldsymbol{V}_{Lw,i}(t) \tag{18}$$

where $\boldsymbol{T}_{E2S}$ is the assembly matrix from the local degrees of freedom of the beam element to the global degrees of freedom of the structure and $\bar{N}_i = \int_0^L \boldsymbol{N}(x)dx$.

To express the quantities in the frequency domain, the cross-spectral density of the buffeting force is obtained as the discrete Fourier transform of its cross-correlation function:

$$R_{\boldsymbol{Q}_{buff}}(\tau) = E[\boldsymbol{Q}_{buff}(t)\,\boldsymbol{Q^T}_{buff}(t+\tau)]$$

$$\boldsymbol{S}_{\boldsymbol{Q}_{buff}}(\omega) = \sum_{i}^{N}\sum_{j}^{N}\boldsymbol{T}_{E2S,i}\,\boldsymbol{T}_{G2Le,i}^{\boldsymbol{T}}\,\bar{N}_i\boldsymbol{B}_{q,i}\boldsymbol{T}_{Lw2Le,i}\,\boldsymbol{S}_V\,(\Delta x,\omega)\boldsymbol{T}_{Lw2Le,j}^{\boldsymbol{T}}\;\boldsymbol{B}_{q,j}^{\boldsymbol{T}}\,\bar{N}_j^{\boldsymbol{T}}\boldsymbol{T}_{G2Le,j}\boldsymbol{T}_{E2S,j}^{\boldsymbol{T}} \tag{19}$$

where $\boldsymbol{S}_V(\Delta\chi,\omega)$ is the cross-spectral density of Equation (1).

The buffeting forces are transformed into generalized coordinates:

$$\tilde{\boldsymbol{S}}_{\boldsymbol{Q}_{buff}}(\omega) = \boldsymbol{\Phi}(x)\boldsymbol{S}_{\boldsymbol{Q}_{buff}}(\omega)\boldsymbol{\Phi}^{\boldsymbol{T}}(x) \tag{20}$$

The buffeting response in the frequency domain is described by its cross-spectral density related to the transfer function H:

$$\tilde{\boldsymbol{S}}_R\;(\omega)\;=\Big[H(\omega)\tilde{\boldsymbol{S}}_{\boldsymbol{Q}_{buff}}(\omega)\;\Big]H^*(\omega) \tag{21}$$

$$H\;(\omega)\;=\big[-\widetilde{\boldsymbol{M}}_0\omega^2+(\widetilde{\boldsymbol{C}}_0-\widetilde{\boldsymbol{C}}_{ae}(V,\omega))i\omega+(\widetilde{\boldsymbol{K}}_0-\widetilde{\boldsymbol{K}}_{ae}(V,\omega))\big]^{-1} \tag{22}$$

where H^* is the complex conjugate of.H.

The cross-spectral density of the response in the global coordinates is then obtained with modal shapes.

$$\boldsymbol{S}_R\;(\omega)\;=\boldsymbol{\Phi}(x)\big[\tilde{\boldsymbol{S}}_R\;(\omega)\big]\boldsymbol{\Phi}^{\boldsymbol{T}}(x) \tag{23}$$

The root mean square of a single response component $-i$ can be obtained from the autospectral density as follows:

$$\begin{aligned}\sigma_{R(i,i)}(x)\;&=\sqrt{\int_{-\infty}^{+\infty}\boldsymbol{S}_{R(i,i)}\;(\omega)d\omega}\\ \sigma_{\dot{R}(i,i)}(x)\;&=\sqrt{\int_{-\infty}^{+\infty}\omega^2\boldsymbol{S}_{R(i,i)}\;(\omega)d\omega}\end{aligned} \tag{24}$$

4.2 Approximate estimation of buffeting response with machine learning

The buffeting response through the multimodal approach may be computationally demanding because of the assembly of the cross-spectral density of the buffeting force in Equation (19) and the inversion of the transfer function H^{-1} of Equation (21). The computational efficiency has a major role in the extreme buffeting response estimation through full long-term analysis since the buffeting response needs to be obtained for several wind states. Alternatives such as surrogate modelling alleviate the computational effort in optimizing the number of multimodal buffeting responses required in the analysis by approximating the underlying relationship between the buffeting response and the wind variables [1]. Figure 8 shows an example of the surrogate modelling strategy for two wind variables: the mean wind speed and the vertical turbulence intensity. The dots in the figure represent wind states used for training the model, and the crosses represent multimodal buffeting responses computed for testing the model. Model estimations are represented with a colormap.

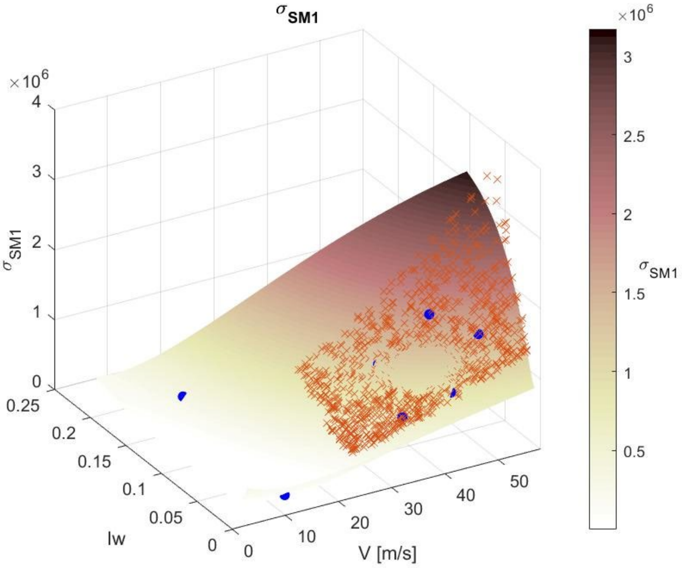

Figure 8: Surrogate modelling of the buffeting response

This study used surrogate model strategies based on machine learning. Three different strategies were utilized: models based on the multilayer perceptron (MLP), models based on support vector regression (SVR) and models based on Gaussian process regression (GPR). The concept of the surrogate modelling strategy is the same for all approaches and will be introduced in the following section. From a wind engineering perspective, the important aspects of the surrogate model strategy are listed as follows: which wind variables are utilized as the input, which responses are used as the output, how to efficiently train the model, how to obtain an estimation, and how to assess the accuracy of the estimations.

The objective of the surrogate model is to approximate the underlying function between the input variables and the output response. The input variables in the analysis are intuitively collected in the vector of wind variables $\boldsymbol{W}$ from Equation (4). The output responses of the analysis are the root mean square of any response component and its time derivative $\boldsymbol{Y} = [\ \sigma_R\ \sigma_{\dot{R}}]$. The target function in this case is the buffeting response estimation through the multimodal approach.

Machine learning models are data-driven, meaning that the model's parameters are calibrated from observed data with known input–output relationships. The initial step is to simulate certain wind states and estimate their buffeting response. The hyperparameters of the model are then optimized for the given data; this step is known as training. In this study, training of the machine learning models was achieved with the statistics and machine learning toolbox of MATLAB 2019b [69].

4.2.1 Surrogate modelling with a multilayered perceptron

An artificial neural network (ANN) is an algorithm that mimics the functioning of biological brains by assembling *layered neurons connected* to each other. A neuron (also known as a unit or node) is an operational entity that stores and distributes information [70]. The neurons are organized into sets referred to as layers, and the neurons within one layer are connected to those in the subsequent layer. The layer connections transmit information within the neurons and are mathematically the arrays that govern the transformation relationships. The value of a neuron in an arbitrary layer is the scalar product between its transformation array and the output of the neurons in the previous layer; the neuron is then activated whenever its value surpasses a certain threshold. The type of neural network applied in this study is the MLP [71], which is schematically shown in Figure 9.

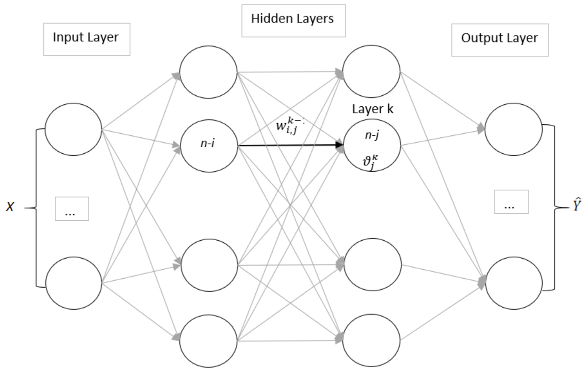

Figure 9: Architecture of an ANN

where y_j^k is referred to as the output of the j-th node in the k-th arbitrary layer of an MLP and is related to an activation bias ϑ_j^k and connection weights $w_{i,j}^{k-1}$, where x_i^{k-1} is the value of the i-th node of the previous layer. The nonlinear activation function $g(x)$ is applied to the result [72]. The feedforward mapping process is then obtained by assembling the abovementioned operations until the model's final M layer is reached:

$$y_j^k = g\left(\sum_{i=1,j=j}^{N} w_{i,j}^{k-1}\, x_i^{k-1} + \vartheta_j^k\right) \tag{25}$$

$$Y^k = g\left\{\left(W_i^{k-1}\right)^T * X^{k-1} + \theta^k\right\} \tag{26}$$

The model estimation of the output $\hat{Y}$ is then obtained:

$$\hat{Y} = f\{(W_i^{M-1})^T \ldots g\{(W_i^1)^T X^1\} + \theta^M\} \tag{27}$$

Introducing the "loss" function $L(\hat{y}_j, y_j)$ as the difference between the known response and the models' estimations, the mathematical objective of the learning process is to minimize the loss function. This minimization is achieved by sending the estimation error through all the previous layers within the network; this operation results in an iterative optimization procedure known as backpropagation [73]. Since the original input is fixed to the dataset, the only parameters to be updated in each iteration are the weights and biases; the procedure yields:

$$find\left(W^{k\in\{1:M-1\}}\ \&\ \theta^{k\in\{1:M\}}\right) \therefore L(\hat{y}_j, y_j) = \min(L) \tag{28}$$

4.2.2 Surrogate modelling with support vector regression

Support vector regression (SVR) is an extension of the *support vector approximation* algorithm to a regression problem [74]. Introducing an ε-insensitive loss function, SVR approximates y_i with a certain tolerance ε. The estimation can be obtained with a linear function as follows:

$$\hat{f}(x) = x'w + \vartheta \tag{29}$$

The ε-insensitive loss function $L(x)$ is equal to zero when the difference between the estimation $\hat{f}(x)$and the known response y is less than ε, and a constraint is added to the problem:

$$L(y - f(x,w)) = \begin{cases} 0 & if\,|y - f(x,w)| \leq \varepsilon \\ |y - f(x,w)| & otherwise \end{cases} \tag{30}$$

To make the solution feasible, the tolerance margin is softened by adding a set of slack variables ξ_i and ξ_i^*, as shown in Figure 10.

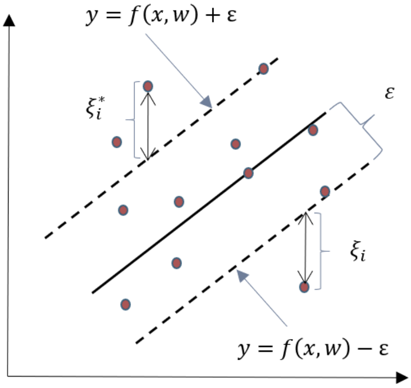

Figure 10: Schematic representation of SVR with slack variables

The optimization problem becomes:

$$\begin{aligned} &minimize && \frac{1}{2}\|w\|^2 + C\sum_{i=1}^{N} \xi_i + \xi_i^* \\ &with\ constraints: && \begin{cases} y_i - f(x,w) \leq \varepsilon + \xi_i \\ f(x,w) - y_i \leq \varepsilon + \xi_i^* \\ \xi_i, \xi_i^* \geq 0 \end{cases} \end{aligned} \tag{31}$$

where C is the box constraint, which is a positive-valued parameter that imposes a penalty on the estimations outside the ε-margin and thus helps to balance the accuracy of the model. Solving this optimization problem with inequality constraints is equivalent to finding the saddle point in the Lagrange function. By introducing α_n and α_n^* as Lagrange multipliers, the weights (w parameters) can be obtained as:

$$w = \sum_{i=1}^{N} (\alpha_i - \alpha_i^*) x_i \tag{32}$$

The model estimation is computed by expanding the support vectors:

$$\hat{f}(x) = \sum_{i=1}^{N} (\alpha_i - \alpha_i^*)(x_i{}'\,x) + \vartheta \tag{33}$$

The parameters ϑ can be obtained by exploiting the Karush–Kun–Tucker (KKT) conditions [75], which state that at the optimal solution, the product between the dual variables and the constraints vanishes.

To extend the formulation to nonlinear regression problems, the dot product $(x_i'x)$ must be replaced with a nonlinear mapping function, known as the kernel function $K(x_i'x)$.

$$f(x) = \sum_{i=1}^{N} (\alpha_i - \alpha_i^*) K(x_i{}' x) + \vartheta \tag{34}$$

4.2.3 Surrogate modelling with Gaussian process regression

Gaussian process regression is a machine learning algorithm in which the responses are assumed to behave as Gaussian processes $GP = \mathcal{N}(\boldsymbol{M}, \boldsymbol{K})$, where $\mathcal{N}$ is the multivariate normal distribution function with mean function $\boldsymbol{M}$ and covariance function $\boldsymbol{K}$.

$$\begin{gathered} y = f(\boldsymbol{w}) \approx \mathcal{N}(M(\boldsymbol{w}), K(\boldsymbol{w}, \boldsymbol{w}')) \\ M(\boldsymbol{w}) = E[f(\boldsymbol{w})] \\ K(\boldsymbol{w}_i, \boldsymbol{w}_j) = E\big[\{f(\boldsymbol{w}_i) - M(\boldsymbol{w}_i)\}\{f(\boldsymbol{w}_j) - M(\boldsymbol{w}_j)\}\text{\textasciicircum}T\big] \end{gathered} \tag{35}$$

The training data will be identified with subscript t, while the estimation data will be denoted with subscript d. The output of the GPR model in the training data is assumed to be contaminated with some standard normal noise $\varepsilon \sim \mathcal{N}(0, \sigma_n^2)$, where the standard deviation of the noise σ_n is a hyperparameter of the model. GPR establishes the joint distribution between the model estimations $\widehat{\boldsymbol{y}}_{\boldsymbol{d}}$ and the prior training data $\boldsymbol{y}_t$ as:

$$\begin{bmatrix} \boldsymbol{y}_t \\ \widehat{\boldsymbol{y}}_d \end{bmatrix} = \mathcal{N}\left(\begin{bmatrix} \boldsymbol{M}(\boldsymbol{w}_t) \\ \boldsymbol{M}(\boldsymbol{w}_d) \end{bmatrix}, \begin{bmatrix} \boldsymbol{K}(\boldsymbol{w}_t, \boldsymbol{w}_t) + \sigma_n^2 \boldsymbol{I} & \boldsymbol{K}(\boldsymbol{w}_t, \boldsymbol{w}_{\boldsymbol{d}}) \\ \boldsymbol{K}(\boldsymbol{w}_{\boldsymbol{d}}, \boldsymbol{w}_t) & \boldsymbol{K}(\boldsymbol{w}_{\boldsymbol{d}}, \boldsymbol{w}_{\boldsymbol{d}}) \end{bmatrix}\right) \tag{36}$$

The marginal probability distribution of the estimation can be written as:

$$p(\widehat{\boldsymbol{y}}_d | \boldsymbol{W}_t, \boldsymbol{y}_t, \boldsymbol{w}_{\boldsymbol{d}}) \sim \mathcal{N}(\mu_{\widehat{\boldsymbol{y}}_d}, \Sigma_{\widehat{\boldsymbol{y}}_d})$$

$$\mu_{\widehat{\boldsymbol{y}}_d} = \widehat{\boldsymbol{y}}_d = \boldsymbol{M}(\boldsymbol{w}_{\boldsymbol{d}}) + \boldsymbol{K}(\boldsymbol{w}_{\boldsymbol{d}}, \boldsymbol{w}_t)[\boldsymbol{K}(\boldsymbol{w}_t, \boldsymbol{w}_t) + \sigma_n^2 \boldsymbol{I}]^{-1}[\boldsymbol{y}_t - \boldsymbol{M}(\boldsymbol{w}_t)] \tag{37}$$

$$\Sigma_{\widehat{\boldsymbol{y}}_d} = \boldsymbol{K}(\boldsymbol{w}_{\boldsymbol{d}}, \boldsymbol{w}_{\boldsymbol{d}}) - \boldsymbol{K}(\boldsymbol{w}_{\boldsymbol{d}}, \boldsymbol{w}_t)[\boldsymbol{K}(\boldsymbol{w}_t, \boldsymbol{w}_t) + \sigma_n^2 \boldsymbol{I}]^{-1} \boldsymbol{K}(\boldsymbol{w}_t, \boldsymbol{w}_{\boldsymbol{d}})^T$$

The correlation between two estimation points is defined by the covariance, which is also known as the kernel function $K(\boldsymbol{w}_i, \boldsymbol{w}_j)$. The kernel function must be specified beforehand to train the GPR model. The literature offers a variety of functions that can be used to model the kernel function. An overview of the kernel functions used for full long-term analysis is provided in [76]. In this study, we employed the squared exponential function:

$$K(\boldsymbol{w}_i, \boldsymbol{w}_j) = \sigma_f^2 \exp\left\{-\frac{|\boldsymbol{w}_i - \boldsymbol{w}_j|^2}{2l^2}\right\} + \sigma_n^2 \tag{38}$$

where σ_f is the standard deviation of the unscaled kernel and l is the length scale. The kernel function was isotropic, and normalization of the wind variables was performed with the Rosenblatt transform [77].

In addition, the mean function of the Gaussian process was chosen as a constant:

$$M(\boldsymbol{w}) = \boldsymbol{w}^T \beta \tag{39}$$

where β is the constant hyperparameter of the modelling.

The model hyperparameters (σ_f, l, σ_n and β) were optimized from the training data using the machine learning and statistics toolbox of MATLAB [69].

5 Extreme response estimation

The procedures of chapter 4 offer different ways to estimate the short-term statistics of the buffeting response. This chapter explains how to obtain the extreme buffeting response based on statistical inferences from these short-term response estimations. The design guidelines assume that the return period of the buffeting response directly corresponds to the return period of the mean speed. The short-term interval with a mean speed equal to the extreme mean speed is sufficient for estimating the extreme buffeting response, and the method is referred to as short-term. The short-term method is a fast and approximate analysis that may not be accurate for long-span bridges, as it disregards the stochastic behaviour of the wind turbulence and the structural response. Section 5.1 explains the method in detail. The environmental contour method explained in Section 5.2 considers the stochastic behaviour of the wind turbulence yielding a more accurate solution. The method proposed an empirical way to handle the stochastic behaviour of the response with the inclusion of inflating factors. Such factors are outside the scope of this thesis. In contrast, the full long-term analysis is the most accurate method for estimating the extreme response since it considers the fluctuations in the weather conditions and their effect on the short-term statistics. In this way, the stochastic behaviour of the response and wind turbulence is considered. The analysis however is computationally demanding, and therefore, traditional application of the method results is unfeasible for practical engineering purposes. Section 5.3 explains the analysis and the efforts of this study to alleviate its computational demand.

5.1 Short-term method

The short-term method is a common approach to most of the current design guidelines for wind-resistant design [17], [18]. The approach defines the design buffeting response based on the extreme mean wind speed with the return period RP (equal to the structure's lifetime) averaged from periods of short-term duration (T_{st}). The buffeting response is assumed to be a stationary, Gaussian and narrow-banded process during T_{st}, such that the average upcrossing of a response threshold r, $V_R^+(r)$, can be obtained from the Rice formulation:

$$V_R^+(r|\boldsymbol{w}) = \frac{1}{2\pi}\frac{\sigma_{\dot{R}}}{\sigma_R}\exp\left\{-\frac{1}{2}\left(\frac{r-\mu_R}{\sigma_R}\right)^2\right\} \tag{40}$$

where μ_R *and* σ_R are the mean and standard deviation, respectively, of the buffeting response from buffeting theory, and $\dot{x}$ denotes the time derivative of x. The statistical moments of the response and its time derivative process from the buffeting response are shown in Equation (24).

Let R_{ST} be the largest value of the response during T_{st}. Assuming that the peaks in the response are independent events, the number of upcrossings in the interval T_{st} is Poisson-distributed, and the CDF of the largest peak$F_{R_{ST}}$ is:

$$Prob\{R_{ST}(T_{ST}) \leq r\} = F_{R_{ST}(T_{ST})}(r|\boldsymbol{w}) = \exp\{-V_R^+(r|\boldsymbol{w})\, T_{ST}\} \tag{41}$$

Combining Equations (40) and (41):

$$F_{R_{RP}(T_{ST})}(r|\boldsymbol{w}) = \exp\left\{-\,T_{ST}\frac{1}{2\pi}\frac{\sigma_{\dot{R}}}{\sigma_R}\exp\left\{-\frac{1}{2}\left(\frac{r-\mu_R}{\sigma_R}\right)^2\right\}\right\} \tag{42}$$

R_p is considered a stochastic variable of the peaks in R. A peak is defined as the maximum value of the response process between two consecutive zero upcrossings. The probability of R_p exceeding threshold r is equal to the number of peaks above r divided by the number of peaks. As the process is narrow-banded, the number of peaks is equal to the zero upcrossings, yielding the CDF of the peaks:

$$F_{R_P}(r|\boldsymbol{w}) = 1 - \frac{V_R^+(r)}{V_R^+(0)} \tag{43}$$

Inserting the expression of the upcrossing rate from Equation (40) in Equation (43):

$$F_{R_P}(r|\boldsymbol{w}) = 1 - \exp\left\{-\frac{1}{2}\left(\frac{r-\mu_R}{\sigma_R}\right)^2\right\} \tag{44}$$

The expected value of R_{ST} is often applied as the design buffeting response and is conveniently formulated with an approximate analytical solution based on the peak factor $\boldsymbol{\kappa}$ [78], [79]. For further details on this procedure, refer to [79]–[82].

$$E[R_{ST}] \ = \mu_R + \kappa\, \sigma_R \ \text{ and} \tag{45}$$

$$\kappa = \ \sigma_R \sqrt{2\ln[V_R^+(0)\,T_{st}]}\left\{1 + \frac{\gamma}{2\ln[V_R^+(0)\,T_{st}]} - \frac{\frac{\pi^2}{6}+\gamma^2}{8(\ln[V_R^+(0)\,T_{st}])^2} + \cdots\right\} \tag{46}$$

$$with\, \gamma \approx 0.577, the\ Euler\ constant$$

5.2 Environmental contour method

The environmental contour method is a method for drawing isoprobability lines of the environmental variables. Using the ECM, it is possible to outline the combination of wind variables with an equal joint probability of occurrence, denominated as wind states (or conditions). For each wind condition along the contour line, the extreme buffeting response is deterministically obtained with the short-term approach of 5.1. The design buffeting response according to the ECM is the maximum extreme response from the wind conditions along the contour. This method provides a more precise estimation of the buffeting response since the stochastic behaviour of the wind turbulence is considered in the analysis. However, as the uncertainty in the response is omitted, inflated contours based on the omission factor should be introduced in the modelling. These inflating factors should be calibrated empirically from estimated extreme responses; thus, they are beyond the scope of this thesis.

Denoting the vector of wind variables with joint probability $\boldsymbol{f_W}$ from the probabilistic modelling as $\boldsymbol{W}$ and R as an extreme response variable, the standard reliability problem yields:

$$p_e = \int_{\text{all } \boldsymbol{W}} P[R > R_{ST} \mid \boldsymbol{W} = \boldsymbol{w}] f_{\boldsymbol{W}}(w)dw \tag{47}$$

where p_e is the exceedance probability of the extreme event $R > R_{ST}$.

The reliability problem is usually solved with the first-order reliability method (FORM). In the method, the set of $\boldsymbol{W}$ variables is transformed into a set of independent standard normal variables $\boldsymbol{U}$ [83]. Now, the response is a function of the new set of standard normal variables, $R = R(\boldsymbol{U})$, and the distribution $f_{\boldsymbol{W}}$ conveniently becomes the normal distribution $\boldsymbol{\phi(U)}$. The integral of Equation (47) in the set of transformed variables can be solved for a given R_{ST} as the minimum distance between the origin and the limit surface. Such distance is known as the reliability index β.

For reliability-based design, however, R_{ST} is the unknown, whereas β is fixed by a design code. In such cases, an inverse FORM application can estimate the extreme response for a given reliability index [84]:

$$\text{Given } \beta\text{: Find } R_{ST} = max|R(\boldsymbol{U})|; subject\ to\ |\boldsymbol{U}| = \beta \tag{48}$$

β is associated with RP through the probability of exceedance:

$$\beta = -\Phi^{-1}(p_e)$$

$$p_e = \left[\frac{RP \text{ x } 365.25 \text{ x}24 \text{ x}60}{T_{st}}\right]^{-1} \tag{49}$$

where Φ is the standard cumulative distribution function.

IFORM estimates that all combinations of $\boldsymbol{U}$ are located distance β from the origin, resulting in a hypersphere of radius β. The environmental variables $\boldsymbol{W}$ can be obtained from $\boldsymbol{U}$ with the Rosenblatt transform [77]; the result is the surface enclosing all combinations of the wind variables with equal joint probability of occurrence, i.e., environmental contours. Subsequently, the extreme buffeting response will be the maximum short-term response along the design points of the contour. Figure 11 shows a graphical interpretation of the environmental contour for different return periods using two environmental variables. The figure on the left shows the contours from the $\boldsymbol{U}$ variables, while the figure on the right shows the transformed contours in the wind variables.

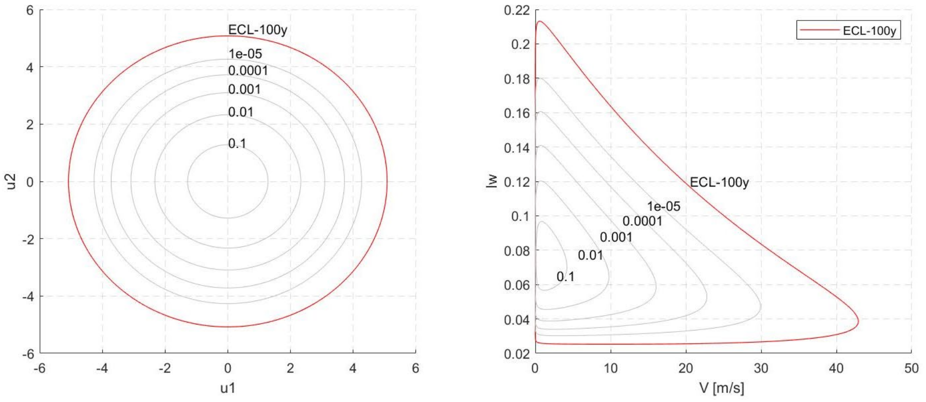

Figure 11: Graphical interpretation of IFORM

5.2.1 Transforming the variables

Since the probabilistic modelling of the wind variables includes two different distributions for the mean wind speed and turbulence parameter, two different transformation rules were applied to transform the wind variables to the $\boldsymbol{U}$ variables. The Weibull distributed mean wind speed was transformed with the Rosenblatt transform [77], while the correlated lognormal distributed turbulence parameters were transformed with a linear transform. In the following part, the transformation rules will be explained.

The Rosenblatt transformation works by obtaining the joint CDF from the product of the marginals:

$$F_{x1x2..xn}(x_1, x_2, \dots, x_n) = F_{x1}(x_1)\, F_{x2}(x_2|x_1) \dots F_{xn}(x_n|x_{n-1} \dots .\, x\_1) \tag{50}$$

Next, the variables are transformed by considering the conditional distributions individually. The mean wind speed was chosen as the first variable, as it is considered the most important variable for the buffeting response of long-span bridges [1]. The mean wind speed was transformed first.

$$F_V(V) = \Phi(u_1) \leftrightarrow \mathrm{V} = F_{\mathrm{V}}^{-1}[\Phi(u_1)] \tag{51}$$

When the stochastic variables are correlated and normally distributed, the linear transformation rule can be applied.

$$\boldsymbol{U} = \boldsymbol{A}(\boldsymbol{X} - \boldsymbol{M}_X) \leftrightarrow \boldsymbol{X} = \boldsymbol{A}^{-1}\boldsymbol{U} + \boldsymbol{M}_X \tag{52}$$

$$\boldsymbol{M}_X = [\mu_{x_1}\ \mu_{x_2}, \dots, \mu_{x_n}]$$

where A is a triangular matrix that can be constructed using the Cholesky decomposition of the covariance matrix C_{XX}, which is Hermitian and positive definite:

$$\boldsymbol{C}_{XX} = \boldsymbol{A}^{-1}\, \boldsymbol{A}^{-T} \tag{53}$$

with

$$\boldsymbol{C}_{XX} = \begin{bmatrix} \sigma_{x_1}^2 & \rho_{12}\sigma_{x_1}\sigma_{x_2} & \cdots & \rho_{1n}\sigma_{x_1}\sigma_{x_n} \\ \rho_{21}\sigma_{x_1}\sigma_{x_2} & \sigma_{x_2}^2 & \cdots & \rho_{2n}\sigma_{x_2}\sigma_{x_n} \\ \vdots & \vdots & \ddots & \vdots \\ \rho_{n1}\sigma_{x_1}\sigma_{x_n} & \rho_{n2}\sigma_{x_2}\sigma_{x_n} & \cdots & \sigma_{x_n}^2 \end{bmatrix} \tag{54}$$

For the case in which stochastic variables are correlated and lognormally distributed, the same transformation rule procedure applies, and the lognormal variables can be obtained as follows:

$$\boldsymbol{X} = \exp\,(\boldsymbol{A}^{-1}\boldsymbol{U} + \boldsymbol{M}_X) \tag{55}$$

The full set of turbulence parameters conditional on the mean wind speed are transformed in a single operation using the linear transformation rule for the case of lognormal distributed variables from Equation (55).

$$F_{I_u, I_v, I_w, A_u, A_v, A_w|V}\,(I_u, I_v, I_w, A_u, A_v, A_w|V) = \Phi(u_2, u_3, u_4, u_5, u_6, u_7) \tag{56}$$

5.3 Full long-term analysis

The full long-term analysis generalizes the short-term method considering the fluctuations in the weather conditions and their effect on the buffeting response over the lifetime of the structure. Therefore, this methodology provides a more accurate estimation of the extreme buffeting response. The long term is composed of a sequence of $\widetilde{N}$ short-term periods of duration T_{st}, $T_{LT} = \widetilde{N} T_{st}$, where $\widetilde{N}$ is a large number.

The analysis establishes the cumulative extreme value distribution of the long-term response:

$$F_{R_{RP}(T_{LT})}(r) = Prob\{R_{RP}(T_{LT}) \leq r\} \tag{57}$$

where $R_{RP}(T_{LT})$ is the largest value that the buffeting response can assume during the long-term period.

If the long-term period is taken as 1 year, Equation (57) will give the extreme value distribution of yearly maxima. For a given return period RP, the design buffeting response has a specified annual probability of exceedance p_e. The design buffeting response will be the value of r that satisfies the following condition:

$$F_{R_{RP}(T_{LT})}(r) = 1 - p_e \tag{58}$$

Alternatively, the condition could be written in terms of the long-term CDF of the short-term extreme value:

$$\begin{gathered} F_{R_{RP}(T_{ST})}(r) = (1 - p_e)^{\frac{1}{\widetilde{N}}} = 1 - \frac{p_e}{\widetilde{N}} \\ R_{RP} = F^{-1}_{R_{RP}(T_{LT})}\left(1 - \frac{1}{RP}\right) \end{gathered} \tag{59}$$

To establish the CDF of the long-term extreme response, the literature offers different approaches. The models differ in the way they handle the short-term statistics. Models are divided into models based on all peak values, models based on all short-term extremes, and models based on the upcrossing rate response [85]–[87]. The methods have been proven to be equivalent [88].

5.3.1 Models based on short-term peak distribution

If all response peaks are assumed to be independent, the long-term extreme value distribution can be formulated as:

$$F_{R_{RP}(T_{LT})}(r) = F_{R_P}(r)^{\overline{V_R^+(0)}T_{LT}} \tag{60}$$

where F_{R_P} is the long-term distribution of peaks and $\overline{V_R^+(0)}$ is the long-term average zero upcrossing obtained from all the short-term wind conditions:

$$\overline{V_R^+(0)} = \int_{\boldsymbol{W}} V_R^+(0|\boldsymbol{w})\, f_{\boldsymbol{W}}(\boldsymbol{w}) dw \tag{61}$$

Denoting the short-term peak distribution as $F_{R_P|\boldsymbol{W}}(r|\boldsymbol{w})$ given the wind condition from Equation (44), the long-term peak distribution according to the Battjes formulation [89], [90] is:

$$F_{R_P}(r) = \frac{1}{\overline{V_R^+(0)}} \int_{\boldsymbol{W}} V_R^+(0|\boldsymbol{w})\, F_{R_P|\boldsymbol{W}}(r|\boldsymbol{w})\, f_{\boldsymbol{W}}\,(\boldsymbol{w})dw \tag{62}$$

5.3.2 Models based on all short-term extremes

If the short-term extreme values are assumed to be independent, the long-term extreme value distribution can adopt the following shape:

$$F_{R_{RP}(T_{LT})}(r) = F_{R_{RP}(T_{ST})}(r)^{\tilde{N}} \tag{63}$$

where $F_{R_{RP}(T_{ST})}$denotes the long-term CDF of the short-term extreme value. This distribution is the ergodic average of the short-term response CDF given the wind condition $F_{R_{RP}(T_{ST})}(r|w)$ from Equation (42):

$$F_{R_{RP}(T_{ST})}(r) \ = \exp\left\{\int_{\boldsymbol{W}} (lnF_{R_{RP}(T_{ST})}(r|\boldsymbol{w}))\, f_{\boldsymbol{W}}\,(\boldsymbol{w})dw\right\} \tag{64}$$

5.3.3 Models based on the upcrossing rate

If the upcrossing of large values of the response threshold r are assumed to be independent, then the long-term extreme value distribution can be obtained as the average upcrossing rate of r weighted by the probability of occurrence of the short-term wind conditions:

$$F_{R_{RP}(T_{LT})}(r) = \exp\{-V_R^+(r|\boldsymbol{w})\, T_{LT}\} \tag{65}$$

$$F_{R_{RP}(T_{LT})}(r) = \ \exp\left\{-T_{LT} \int_{\boldsymbol{W}} V_R^+(r|\boldsymbol{w})\, f_{\boldsymbol{W}}\,(w)dw\right\}$$

The analytical solution of the full long-term methodology involves numerical integration and large computational effort, regardless of the model selected. Hence, the motivation in the wind engineering and structural reliability literature is to implement an alternative solution that can be both fast and accurate.

5.3.4 Long-term formulation based on ISMC

Monte Carlo simulations evaluate the short-term responses for simulated wind states and reformulate Equation (65) as a statistical average that converges to the exact solution:

$$F_{r_{RP}(T_{LT})}(r) = \exp\left\{-\frac{T_{LT}}{N_{sim}}\sum_{i=1}^{N_{sim}} V_R^+(r|\boldsymbol{w}_i)\right\} \tag{66}$$

where N_{sim} is the number of simulations to be checked with the convergence criterion.

The crude Monte Carlo method converges slowly and hence motivates the implementation of an importance sampling strategy [91]. The approach works by generating the wind states from the importance sampling distribution function $h_{\boldsymbol{W}}$, which is chosen to generate wind states with significant contributions to the full long-term analysis. $h_{\boldsymbol{W}}$ is determined from engineering judgement. Equation (66) becomes:

$$F_{r_{RP}(T_{LT})}(r) = \exp\left\{-\frac{T_{LT}}{N_{sim}}\sum_{i=1}^{N_{sim}} V_R^+(r|\boldsymbol{w}_i)\frac{f_{\boldsymbol{W}}(\boldsymbol{w}_i)}{h_{\boldsymbol{W}}(\boldsymbol{w}_i)}\right\} \tag{67}$$

The simulation scheme was further simplified by generating the samples as independent standard normally distributed variables, $\boldsymbol{U}$, which are then transformed into the wind state variables through the Rosenblatt transformation rule [77]:

$$F_{r_{RP}(T_{LT})}(r) = exp\left\{-\frac{T_{LT}}{N_{sim}}\sum_{i=1}^{N_{sim}} V_R^+(r|\boldsymbol{u}_i)\frac{f_{\boldsymbol{U}}(\boldsymbol{u}_i)}{h_{\boldsymbol{U}}(\boldsymbol{u}_i)}\right\} \tag{68}$$

It is common practice to use a normal distribution as an importance sampling distribution function. This practice, however, is not feasible in this case since it will render extremely high wind velocities, in which the buffeting response model applied in this thesis will yield inaccurate results. Therefore, a uniform distribution was utilized since this alternative is the simplest. The sampling function was chosen as an $N-sized$, multiple uncorrelated uniform distribution:

$$h_{\boldsymbol{U}}(\boldsymbol{u}) = \prod_{k=1}^{N} \mathcal{U}_k(x|a_k, b_k) \tag{69}$$

where $k = \{1,2,\dots,N\}$ is an index of the stochastic variables and $\mathcal{U}(a,b)$ is the uniform distribution with lower and upper limits a, b:

$$\mathcal{U}(x) = \begin{cases} \frac{1}{b-a}, for\ x \in [a,b] \\ 0 \quad , else\ where \end{cases} \tag{70}$$

The distribution limits a, b are chosen such that the generated wind states are within the domain where the model of response prediction is accurate.

5.3.5 Long-term formulation based on ISMC and Gaussian process regression

As shown in Equation (65), the contribution of each wind state to the long-term extreme response is the product of its probability of occurrence and the upcrossing rate of its short-term buffeting response:

$$\eta(r, \boldsymbol{w}) = V_R^+(r|\boldsymbol{w}) f_{\boldsymbol{W}}(\boldsymbol{w}) \tag{71}$$

GPR can be trained to estimate any short-term response statistics. $\hat{V}_R^+$ can be obtained from the GPR estimations of $\hat{\sigma}_R$ and $\hat{\sigma}_{\dot{R}}$. The contribution to the long-term analysis from the surrogate model estimation is:

$$\hat{\eta}(r, \boldsymbol{w}) = \hat{V}_R^+(r|\boldsymbol{w}) f_{\boldsymbol{W}}(\boldsymbol{w}) \tag{72}$$

$\hat{\eta}$ is then normalized with its maximum value:

$$\hat{\eta}(r = R_{st}, \boldsymbol{w}) = \frac{\hat{V}_R^+(r = R_{st}|\boldsymbol{w}) f_{\boldsymbol{W}}(\boldsymbol{w})}{\max\left[\hat{V}_R^+(r = R_{st}|\boldsymbol{w}) f_{\boldsymbol{W}}(\boldsymbol{w})\right]} \tag{73}$$

The set $\boldsymbol{w}_d$ of wind states with relevant contributions to the extreme wind response can be obtained for a given level of normalized contribution ζ as:

$$\boldsymbol{w}_d \in \boldsymbol{W} \, \{\hat{\eta} \geq \zeta\} \tag{74}$$

Next, the limits of the sampling function of the ISMC framework are chosen such that all the generated samples belong to the set $\boldsymbol{w}_d$.

The estimations from GPR are probability distributions with a direct measure of the estimation's uncertainty. The uncertainty in the estimation can be employed as a Bayesian updating approach. The surrogate model can decide to perform a new multimodal buffeting response estimation at the wind state with higher estimation uncertainty. The model will be sequentially updated until a convergence of the extreme response is achieved. The Bayesian updating approach can be generalized with the concept of the learning function $\boldsymbol{\Omega}$. A learning function will consider not only the GPR estimation's uncertainty but also the contribution of any candidate wind state to the analysis. For the case study, the learning function was adopted as the weighted product between the normalized contribution to the buffeting response $\hat{\eta}$ and the norm of $\boldsymbol{\Sigma}$, which is a vector that contains the standard deviation of $\hat{\sigma}_R$ and $\hat{\sigma}_{\dot{R}}$ for each wind state, as shown in [92]. Next, the learning function for the $i-th$ GPR model is:

$$\Omega_{GP_i}(\boldsymbol{w}) = \hat{\eta}_{GP_i}(r = R_{st}, \boldsymbol{w})^{1-s} \ \left|\boldsymbol{\Sigma}_{GP_i}(\boldsymbol{w})\right|^{s/2} \tag{75}$$

where $GP_{i=1} = \mathcal{N}\left(M(\boldsymbol{w}_t), K(\boldsymbol{w}_t, \boldsymbol{w}_t')\right)$ is the initial model and $0 \leq s \leq 1$ is the weighting parameter. As s tends to 0, more weight is given to the normalized contribution, s tends to 1, and more weight is given to the norm of the standard deviation.

The Bayesian updating is restricted to the wind states within $\boldsymbol{w}_d$ with relevant contributions to the analysis:

$$\boldsymbol{w}_{next} = \arg\max\left\{\Omega_{GP_i}(\boldsymbol{w_d}|GP_i)\right\} \tag{76}$$

The buffeting response with the multimodal approach will be computed for $\boldsymbol{w}_{next}$, and the surrogate model will be updated with the new observation:

$$GP_{i+1} = \mathcal{N}(M([\boldsymbol{w}_t;\ \boldsymbol{w}_{next}]), K([\boldsymbol{w}_t;\ \boldsymbol{w}_{next}], [\boldsymbol{w}_t;\ \boldsymbol{w}_{next}]')) \tag{77}$$

The extreme buffeting response $R_{RP}(GP_i)$ from the GPR model will be obtained and compared with the previous estimation $R_{RP}(GP_{i-1})$. The percent difference between the updated model estimation and the previous model estimation will be obtained as:

$$\Delta_i = \frac{|R_{RP}(GP_i) - R_{RP}(GP_{i-1})|}{R_{RP}(GP_{i-1})} \tag{78}$$

The sequential updating procedure can be repeated until Δ is below a given tolerance level tol for n-consecutive updates.

6 Summary of the appended papers

6.1 Declaration of Authorship

In paper 1, all coauthors contributed to the planning of the paper. Dario Fernandez Castellon wrote the manuscript, while Aksel Fenerci and Ole Andre Øiseth provided feedback and contributed to improvements in the manuscript. Dario Fernande Castellon carried out all the calculations included in the paper and developed all the code for the machine learning algorithms. Professor Ole Andre Øiseth provided the code for the buffeting response with the multimodal approach.

In paper 2, all coauthors contributed to the planning of the paper. Dario Fernandez Castellon processed the data from the Sulafjord Bridge site. He also implemented all necessary code and performed all numerical calculations. Aksel Fenerci and Ole Andre Øiseth contributed to discussions of the obtained results and suggestions for improvements. Dario Fernandez Castellon wrote the manuscript, while Aksel Fenerci and Ole Andre Øiseth provided feedback and contributed to improving the manuscript.

In papers 3 and 4, Dario Fernandez Castellon planned the work with contributions from Aksel Fenerci, Ole Andre Øiseth and Øyvind Wiig Petersen. Ole Andre Øiseth provided a buffeting response code using the multimodal approach. Øyvind Wiig Petersen made the finite element model of the bridge. Dario Fernandez Castellon developed the code for the long-term analysis and wrote the manuscript. All coauthors contributed to improving the manuscript.

6.2 Paper 1

A comparative study of wind-induced dynamic response models of long-span bridges using artificial neural networks, support vector regression and buffeting theory

This paper tested the accuracy of machine learning surrogate models for buffeting response estimations. Two different models were developed based on the multilayered perceptron and support vector regression. The paper discussed different strategies to format the data and properly train the surrogate models. The model estimations were compared with analytical models and full-scale measurements. The results showed remarkable accuracy for the analytical model-based multimodal approach. Regarding the full-scale measurements, data from the Hardanger Bridge were utilized. The models' estimation showed large scatter as the observed data. The estimations had good accuracy on the same order of magnitude as the other analytical models; however, the surrogate model strategy consumed only a fraction of the execution time.

6.3 Paper 2

Environmental contours for wind-resistant bridge design in complex terrain.

This paper provides the wind field characterization of the Sulafjord site in a probabilistic way. The study applies the environmental contours method to draw curves of the isoprobability of the different wind variables. The paper showed the probable wind conditions that can be expected at the Sulafjord site for different return periods in contrast to the traditional approach, which shows only single values of mean wind speed and turbulence parameters from deterministic relationships. In this way, using the same date typically available for the design of long-span bridges, we showed a more complete yet intuitive representation of the wind field at Sulafjord.

6.4 Paper 3

Investigations of the long-term extreme buffeting response of long-span bridges using importance sampling Monte Carlo simulations.

Owing to the probabilistic wind characterization of the Sulafjord site, it was possible to expand the traditional deterministic response estimation method to a more reliable full long-term analysis. This paper reports the investigations of three significant internal forces of the Sulafjord bridge model due to wind loading. In this paper, different extreme response estimation methods were employed and compared. Since the main disadvantage of the full long-term analysis is its high computational demand, in this paper, we also propose a framework based on importance sampling Monte Carlo simulations that is designed to alleviate the long-term analysis procedure. The results showed that the extreme responses from the full long-term analysis were 25% larger than the responses from the short-term method employed in most of the current wind resistance design guidelines.

6.5 Paper 4

Full long-term buffeting analysis of suspension bridges using Gaussian process surrogate modelling and importance sampling Monte Carlo simulations.

After declaring the importance of full long-term analysis, a major challenge arose: making long-term analysis feasible for the wind-resistant design of long-span bridges. Although the importance sampling framework of paper 3 alleviated the long-term analysis procedure, most of the computational demand is still on the time-consuming evaluations of the buffeting response. The experience with surrogate modelling (paper 1) showed the potential of this alternative for buffeting response estimations since remarkably fast and accurate response estimations were obtained for several wind states. Nevertheless, optimizing the training procedure was a key factor discovered in that initial study. Therefore, in paper 4, we proposed an efficient and reliable framework for full long-term analysis that combines the strategies of paper 1 and paper 3. A machine learning surrogate model (Gaussian process regression) was implemented to estimate the short-term buffeting responses, and the full long-term analysis was performed with importance sampling Monte Carlo simulations. The framework showed significant accuracy up to 99.6% compared with the traditional full long-term analysis, which uses less than 1% of computational demand.

7 Conclusions

The papers enclosed in this thesis propose a framework for full long-term analysis that is efficient and reliable for the wind-resistant design of long-span bridges. The framework was successfully employed to estimate the extreme buffeting response of the Sulafjord Bridge, and the following conclusions were drawn:

- Environmental contours are a more efficient strategy for characterising the wind field in long-span bridge projects located in complex terrain than the traditional practice of reporting extreme wind speeds and the corresponding turbulence parameters. The environmental contours provide a more complete yet intuitive description of the wind field at the bridge site than the current design methodology. The contours presented in this thesis reasonably captured the variability in the wind variables compared with the site measurements.

- Including the stochastic behaviour of the wind turbulence in the analysis provided an increased degree of reliability. The extreme response from the environmental contour method was on average 14% higher than that of the common practice based on the short-term method.

- Surrogate models proved to be an accurate alternative to reducing the computational effort of the time-consuming evaluations of the buffeting response (multimodal approach). The complement of the mean absolute percent error (MAPE) exceeded 98% for the multilayer perceptron model and the supporting vector regression model compared with the analytical buffeting responses of the Hardanger Bridge. The Gaussian process regression model of the Sulafjord Bridge showed a good estimation accuracy as well, with the additional feature of optimizing the number of simulations required for training.

- The extreme response from the full long-term analysis was higher than the response from the short-term method. The difference between the two approaches was on average above 25% for the analysed responses. This finding shows that using the full long-term analysis for long-span bridge design enhances safety as wind loading effects increase.
- An efficient full long-term analysis framework for estimating the design buffeting response of long-span bridges was successfully developed. The framework combined two major strategies: Gaussian process regression to increase the computational efficiency of short-term response estimations and importance sampling Monte Carlo to reduce the time of the full long-term analysis. The results show that the proposed framework required less than 1% of the computational effort required by the traditional full long-term analysis based on numerical integration.

8 Future research

Extend the modelling to other long-span bridge locations to determine if the findings of this thesis are features of the Sulafjord site or if major trends exist that are worth publishing.

- Generalize the concept of the importance sampling distribution function defined by engineering criterion. It should be possible to make an automated criterion for the sampling function that is not based on project-specific observations.
- Expand the framework of the full long-term analysis with other reliability methods, such as subset simulations and Markov chains.
- Explore enhanced surrogate model strategies, such as ensembles of neural networks that can also estimate responses as probability distributions.
- Propose alternative analysis in the time domain to properly account for nonlinearities in the modelling, as these could govern the design if the sensitivity of the deck to the angle of attack starts to have a major role in the analysis.
- Calculate the empirical inflating factors for the environmental contours and propose a dimensioning criterion of these coefficients that can be utilized in other projects and integrated into design guidelines.

9 References

[1] D. F. Castellon, A. Fenerci, and O. Øiseth, “A comparative study of wind-induced dynamic response models of long-span bridges using artificial neural networks, support vector regression and buffeting theory,” *J. Wind Eng. Ind. Aerodyn.*, vol. 209, p. 104484, 2021, doi: https://doi.org/10.1016/j.jweia.2020.104484.

[2] D. Castellon, A. Fenerci, and Ø. Ole, “Environmental contours for wind-resistant bridge design in complex terrain,” *J. Wind Eng. Ind. Aerodyn.*, vol. 224, no. January, 2022, doi: 10.1016/j.jweia.2022.104943.

[3] D. F. Castellon, O. A. Øiseth, A. Fenerci, and Ø. W. Petersen, “Investigations of the long-term extreme buffeting response of long-span bridges using importance sampling Monte Carlo simulations,” *Sent J. Publ. Struct.*, 2022.

[4] D. Castellon, A. Fenerci, Ø. Petersen, and O. Oiseth, “Full long-term buffeting analysis of suspension bridges using Gaussian process surrogate modelling and importance sampling Monte Carlo simulations,” *Sent J. Publ. Eng. Syst. Saf.*

[5] D. F. Castellon, A. Fenerci, and O. A. Øiseth, “A study on the evaluation of wind induced vibration of long-span suspension bridges with artificial neural networks,” *Proc. Int. Conf. Struct. Dyn. , EURODYN*, vol. 1, pp. 1958–1967, 2020, doi: 10.47964/1120.9159.18554.

[6] D. F. Castellon, Aksel Fenerci, and O. Øiseth, “A PROBABILISTIC ANALYSIS OF THE WIND FIELD AT SULAFJORDEN BRIDGE SITe,” in *ANCRiSST:14th International Workshop on Advanced Smart Materials and Smart Structures Technology*, 2019, pp. 115–118, [Online]. Available: https://doi.org/10.13133/9788893771146.

[7] C. C. Caprani and J. De Maria, “Long-span bridges: analysis of trends using a global database,” *Struct. Infrastruct. Eng.*, vol. 16, no. 1, pp. 219–231, Jan. 2020, doi: 10.1080/15732479.2019.1639773.

[8] H. E. Fairclough, M. Gilbert, A. V. Pichugin, A. Tyas, and I. Firth, “Theoretically optimal forms for very long-span bridges under gravity loading,” *Proc. R. Soc. A Math. Phys. Eng. Sci.*, vol. 474, no. 2217, 2018, doi: 10.1098/rspa.2017.0726.

[9] Y.-L. Xu, “Wind Storms and Cable-Supported Bridges,” *Wind Effects on Cable-Supported Bridges*. pp. 1–23, Mar. 19, 2013, doi: https://doi.org/10.1002/9781118188293.ch1.

[10] A. G. DAVENPORT, “THE RESPONSE OF SLENDER, LINE-LIKE STRUCTURES TO A GUSTY WIND.,” *Proc. Inst. Civ. Eng.*, vol. 23, no. 3, pp. 389–408, 1962, doi: 10.1680/iicep.1962.10876.

[11] R. H. Scanlan and R. H. Gade, “Motion of Suspended Bridge Spans under Gusty Wind,” *J. Struct. Div.*, vol. 103, pp. 1867–1883, 1977.

[12] R. H. Scanlan, “The action of flexible bridges under wind, I: Flutter theory,” *J. Sound Vib.*, vol. 60, no. 2, pp. 187–199, 1978, doi: https://doi.org/10.1016/S0022-460X(78)80028-5.

[13] Y. K. Lin and J. N. Yang, “Multimode Bridge Response to Wind Excitations,” *J. Eng. Mech.*, vol. 109, no. 2, pp. 586–603, 1983, doi: 10.1061/(asce)0733-9399(1983)109:2(586).

[14] X. Chen, M. Matsumoto, and A. Kareem, “AERODYNAMIC COUPLING EFFECTS ON FLUTTER AND BUFFETING OF BRIDGES,” vol. 126, no. January, pp. 17–26, 2000.

[15] X. Chen, M. Matsumoto, and A. Kareem, “Time Domain Flutter and Buffeting Response Analysis of Bridges,” *J. Eng. Mech.*, vol. 126, no. 1, pp. 7–16, 2000, doi: 10.1061/(asce)0733-9399(2000)126:1(7).

[16] T. Miyata, “Historical view of long-span bridge aerodynamics,” *J. Wind Eng. Ind. Aerodyn.*, vol. 91, no. 12, pp. 1393–1410, 2003, doi: https://doi.org/10.1016/j.jweia.2003.09.033.

[17] CEN, *Eurocode 1: Actions on structures - Part 1-4: General actions - Wind actions*, vol. 1, no. 2005. 2004.

[18] Statens Vegvesen, *Håndbok N400 Bruprosjektering*. 2015.

[19] Y. Xu, O. Øiseth, T. Moan, and A. Naess, “Prediction of long-term extreme load effects due to wave and wind actions for cable-supported bridges with floating pylons,” *Eng. Struct.*, vol. 172, no. June, pp. 321–333, 2018, doi: 10.1016/j.engstruct.2018.06.023.

[20] T. M. Lystad, A. Fenerci, and O. Øiseth, “Buffeting response of long-span bridges considering uncertain turbulence parameters using the environmental contour method,” *Eng. Struct.*, vol. 213, no. March, p. 110575, 2020, doi: 10.1016/j.engstruct.2020.110575.

[21] Norwegian Public Roads Administration, “National Transport Plan 2014 - 2023,” vol. 26, p. 37, 2013, [Online]. Available: http://www.ntp.dep.no/English/_attachment/527975/binary/850289?_ts=14149e8f1a8.

[22] K. K. Dunham, “Coastal Highway Route E39 - Extreme Crossings,” *Transp. Res. Procedia*, vol. 14, no. 2352, pp. 494–498, 2016, doi: 10.1016/j.trpro.2016.05.102.

[23] Statens Vegvesen, “E39 Sulafjorden Multispan suspension bridge om GBS Feasibility studies-Presentation.” 2016, [Online]. Available: https://www.vegvesen.no/_attachment/1545452/binary/1135150?fast_title=16+Flerspenns+hengebru+på+fast+fundament+%28GBS%29.pdf.

[24] R. N. Møller, “Aerodynamic Stability of Long Span Bridges PhD Thesis,” DTU, 2019.

[25] R. N. Møller, S. Krenk, and M. N. Svendsen, “Time simulation of aerodynamic response of long-span bridges to turbulent wind,” *J. Wind Eng. Ind. Aerodyn.*, vol. 199, no. December 2019, 2020, doi: 10.1016/j.jweia.2019.104060.

[26] B. R. Furevik, H. Agustsson, A. Lauen Borg, Z. Midjiyawa, F. Nyhammer, and M. Gausen, “Meteorological observations in tall masts for the mapping of atmospheric flow in Norwegian fjords,” *Earth Syst. Sci. Data*, vol. 12, no. 4, pp. 3621–3640, 2020, doi: 10.5194/essd-12-3621-2020.

[27] Z. Midjiyawa, E. Cheynet, J. Reuder, H. Ágústsson, and T. Kvamsdal, “Potential and challenges of wind measurements using met-masts in complex topography for bridge design: Part I – Integral flow characteristics,” *J. Wind Eng. Ind. Aerodyn.*, vol. 211, no. October 2020, 2021, doi: 10.1016/j.jweia.2021.104584.

[28] Gill Instruments, “Software bug affecting ‘w’ wind component of the WindMaster family,” pp. 1–6, 2016, [Online]. Available: www.gillinstruments.com.

[29] T. von Karman, “PROGRESS IN THE STATISTICAL THEORY OF TURBULENCE,” *Proc. N. A. S.*, vol. 34, pp. 530–539, 1948.

[30] G. Naito, “Spatial structure of surface wind over the ocean,” *J. Wind Eng. Ind. Aerodyn.*, vol. 13, pp. 67–76, 1983.

[31] H. R. Olesen, S. E. Larsen, and J. Højstrup, “Modelling velocity spectra in the lower part of the planetary boundary layer,” *Boundary-Layer Meteorol.*, vol. 29, no. 3, pp. 285–312, 1984, doi: 10.1007/BF00119794.

[32] P. HA and M. RA, “The spectrum of vertical velocity near the surface,” *Q. J. R. Meteorol. Soc.*, vol. 86, no. 370, pp. 495–503, 1960.

[33] J. Mann, “The spatial structure of neutral atmospheric surface-layer turbulence,” *J. Fluid Mech.*, vol. 273, pp. 141–168, 1994, doi: 10.1017/S0022112094001886.

[34] H. W. Tieleman, “Wind characteristics in the surface layer over heterogeneous terrain,” *J. Wind Eng. Ind. Aerodyn.*, vol. 41, no. 1–3, pp. 329–340, 1992, doi: 10.1016/0167-6105(92)90427-C.

[35] H. W. Tieleman, “Universality of velocity spectra,” *J. Wind Eng. Ind. Aerodyn.*, vol. 56, no. 1, pp. 55–69, 1995, doi: https://doi.org/10.1016/0167-6105(94)00011-2.

[36] H. A. Panofsky *et al.*, “Spectra of velocity components over complex terrain,” *Q. J. R. Meteorol. Soc.*, vol. 108, pp. 215–230, 1982.

[37] H. W. Teunissen, “Structure of mean winds and turbulence in the planetary boundary layer over rural terrain,” *Boundary-Layer Meteorol.*, vol. 19, no. 2, pp. 187–221, 1980, doi: 10.1007/BF00117220.

[38] H. A. Panofsky, “The Pennsylvania State University, University Park, Pa., U.S.A.,” vol. 11, no. 1964, pp. 355–361, 1976.

[39] N. E. Busch and H. A. Panofsky, “Recent spectra of atmospheric turbulence,” *Q. J. R. Meteorol. Soc.*, vol. 94, no. 400, pp. 132–148, 1968, doi: 10.1002/qj.49709440003.

[40] A. G. Davenport, “The spectrum of horizontal gustiness near the ground in high winds,” *Q. J. R. Meteorol. Soc.*, vol. 87, pp. 194–211, 1961.

[41] B. G. Solari, “functions are rendered explicit . The literature is full of analytical models aimed at offering a correct description of both these quantities . One can in particular assert that , with the passage of time , these models have been progressively improved t,” vol. 113, no. 7, pp. 1550–1569, 1987.

[42] G. Solari and G. Piccardo, “Probabilistic 3-D turbulence modeling for gust buffeting of structures,” *Probabilistic Eng. Mech.*, vol. 16, no. 1, pp. 73–86, 2001, doi: 10.1016/S0266-8920(00)00010-2.

[43] J. C. Kaimal, J. C. Wyngaard, Y. Izumi, and O. R. Coté, “Spectral characteristics of surface-layer turbulence,” *Q. J. R. Meteorol. Soc.*, vol. 98, no. 417, pp. 563–589, 1972, doi: https://doi.org/10.1002/qj.49709841707.

[44] ESDU 086010, *Characteristics of Atmospheric Turbulence Near the Ground. Part 1: Definitions and General Information. Part II: Single Point Data for Strong Winds (neutral Atmosphere). Part III: Variations in Space and Time for Strong Winds (neutral Atmosphere).* Engineering Sciences Engineering Sciences, 1974.

[45] J. Mann, “The spectral velocity tensor in moderately complex terrain,” *J. Wind Eng. Ind. Aerodyn.*, vol. 88, no. 2–3, pp. 153–169, 2000.

[46] A. J. Bowen, R. G. J. Flay, and H. A. Panofsky, “Vertical coherence and phase delay between wind components in strong winds below 20 m,” *Boundary-Layer Meteorol.*, vol. 26, no. 4, pp. 313–324, 1983, doi: 10.1007/BF00119530.

[47] N. O. Jensen and L. Kristensen, “Lateral Coherence in Isotropic Turbulence and in the Natural Wind,” *Boundary-Layer Meteorol.*, vol. 17, no. 3, pp. 353–373, 1979, doi: 10.1007/BF00117924.

[48] A. G. Davenport, “Buffetting of a Suspension Bridge by Storm Winds,” *J. Struct. Div.*, vol. 88, no. 3, 1962, doi: https://doi.org/10.1061/JSDEAG.0000773.

[49] A. Fenerci and O. Øiseth, “Measured Buffeting Response of a Long-Span Suspension Bridge Compared with Numerical Predictions Based on Design Wind Spectra,” *J. Struct. Eng.*, vol. 143, no. 9, p. 04017131, 2017, doi: 10.1061/(asce)st.1943-541x.0001873.

[50] A. Fenerci, O. Øiseth, and A. Rønnquist, “Long-term monitoring of wind field characteristics and dynamic response of a long-span suspension bridge in complex terrain,” *Eng. Struct.*, vol. 147, pp. 269–284, 2017, doi: 10.1016/j.engstruct.2017.05.070.

[51] A. Fenerci and O. Øiseth, “Site-specific data-driven probabilistic wind field modeling for the wind-induced response prediction of cable-supported bridges,” *J. Wind Eng. Ind. Aerodyn.*, vol. 181, no. June, pp. 161–179, 2018, doi: 10.1016/j.jweia.2018.09.002.

[52] X. Meng *et al.*, “Design and implementation of a new system for large bridge monitoring—geoshm,” *Sensors (Switzerland)*, vol. 18, no. 3, 2018, doi: 10.3390/s18030775.

[53] J.-L. Song, J.-W. Li, and R. Flay, “Field measurements and wind tunnel investigation of wind characteristics at a bridge site in a Y-shaped valley,” *J. Wind Eng. Ind. Aerodyn.*, vol. 202, p. 104199, Jul. 2020, doi: 10.1016/j.jweia.2020.104199.

[54] H. Wang, T. Tao, Y. Gao, and F. Xu, “Measurement of Wind Effects on a Kilometer-Level Cable-Stayed Bridge during Typhoon Haikui,” *J. Struct. Eng.*, vol. 144, no. 9, p. 04018142, 2018, doi: 10.1061/(asce)st.1943-541x.0002138.

[55] W. M. Zhang, Z. W. Wang, and Z. Liu, “Joint Distribution of Wind Speed, Wind Direction, and Air Temperature Actions on Long-Span Bridges Derived via Trivariate Metaelliptical and Plackett Copulas,” *J. Bridg. Eng.*, vol. 25, no. 9, p. 04020069, 2020, doi: 10.1061/(ASCE)BE.1943-5592.0001608.

[56] Y.-M. Zhang, H. Wang, J.-X. Mao, Z.-D. Xu, and Y.-F. Zhang, “Probabilistic Framework with Bayesian Optimization for Predicting Typhoon-Induced Dynamic Responses of a Long-Span Bridge,” *J. Struct. Eng.*, vol. 147, no. 1, p. 04020297, 2021, doi: 10.1061/(asce)st.1943-541x.0002881.

[57] E. Cheynet, J. B. Jakobsen, and J. Snæbjörnsson, “Buffeting response of a suspension bridge in complex terrain,” *Eng. Struct.*, vol. 128, pp. 474–487, 2016, doi: 10.1016/j.engstruct.2016.09.060.

[58] A. G. Davenport, “THE APPLICATION OF STATISTICAL CONCEPTS TO THE WIND LOADING OF STRUCTURES.,” 1961.

[59] R. H. Scanlan and J. J. Tomko, “Airfoil and Bridge Deck Flutter Derivatives,” *J. Eng. Mech. Div.*, vol. 97, no. 6, pp. 1717–1737, 1971, [Online]. Available: https://cedb.asce.org/CEDBsearch/record.jsp?dockey=0017902.

[60] W. Petersen, O. Øiseth, and E. Lourens, “Investigation of dynamic wind loads on a long-span suspension bridge identified from measured acceleration data,” *J. Wind Eng. Ind. Aerodyn.*, vol. 196, no. March 2019, 2020, doi: 10.1016/j.jweia.2019.104045.

[61] W. Tu, *Basic principles of statistical inference.*, vol. 404. 2007.

[62] M. D. C. Moura, E. Zio, I. D. Lins, and E. Droguett, “Failure and reliability prediction by support vector machines regression of time series data,” *Reliab. Eng. Syst. Saf.*, vol. 96, no. 11, pp. 1527–1534, 2011, doi: 10.1016/j.ress.2011.06.006.

[63] Ø. W. Petersen and O. Øiseth, “Finite element model updating of a long span suspension bridge,” *Geotech. Geol. Earthq. Eng.*, vol. 47, no. January, pp. 335–344, 2019, doi: 10.1007/978-3-319-78187-7_25.

[64] X. Chen, “Analysis of Multimode Coupled Buffeting Response of Long-Span Bridges to Nonstationary Winds with Force Parameters from Stationary Wind,” *J. Struct. Eng.*, vol. 141, no. 4, p. 04014131, 2015, doi: 10.1061/(asce)st.1943-541x.0001078.

[65] X. Chen, A. Kareem, and M. Matsumoto, “Multimode coupled flutter and buffeting analysis of long span bridges,” *J. Wind Eng. Ind. Aerodyn.*, vol. 89, no. 7–8, pp. 649–664, 2001, doi: 10.1016/S0167-6105(01)00064-2.

[66] A. Jain, N. P. Jones, and R. H. Scanlan, “Coupled Flutter and Buffeting Analysis of Long-Span Bridges,” *J. Struct. Eng.*, vol. 122, no. 7, pp. 716–725, 1996, doi: 10.1061/(asce)0733-9445(1996)122:7(716).

[67] H. Katsuchi, N. P. Jones, R. H. Scanlan, and H. Akiyama, “Multi-mode flutter and buffeting analysis of the Akashi-Kaikyo bridge,” *J. Wind Eng. Ind. Aerodyn.*, vol. 77–78, pp. 431–441, 1998, doi: 10.1016/S0167-6105(98)00162-7.

[68] O. Øiseth, A. Rönnquist, and R. Sigbjörnsson, “Simplified prediction of wind-induced response and stability limit of slender long-span suspension bridges, based on modified quasi-steady theory: A case study,” *J. Wind Eng. Ind. Aerodyn.*, vol. 98, no. 12, pp. 730–741, 2010, doi: 10.1016/j.jweia.2010.06.009.

[69] I. The Matworks, “Statistics and Machine Learning ToolBox.” https://se.mathworks.com/products/statistics.html.

[70] F. Rosenblatt, “The perceptron: A probabilistic model for information storage and organization in the brain,” *Psychol. Rev.*, vol. 65, no. 6, pp. 386–408, 1958, doi: 10.1037/h0042519.

[71] A. A. Mullin and F. Rosenblatt, “Principles of Neurodynamics.,” *Am. Math. Mon.*, vol. 70, no. 5, p. 586, 1963, doi: 10.2307/2312103.

[72] Bishop, *Pattern Recognition and Machine Learning*. Springer-Verlag New York, 2006.

[73] D. E. Rumelhart, G. E. Hinton, and R. J. Williams, “Learning representations by back-propagating errors,” *Nature*, vol. 323, no. 6088, pp. 533–536, 1986, doi: 10.1038/323533a0.

[74] VAPNIK and V. N., “The Nature of Statistical Learning,” *Theory*. 1995, [Online]. Available: https://ci.nii.ac.jp/naid/10020951890.

[75] H. W. Kuhn and A. W. Tucker, “Nonlinear programming,” in *Proceedings of the {S}econd {B}erkeley {S}ymposium on {M}athematical {S}tatistics and {P}robability, 1950*, 1951, pp. 481–492.

[76] F. Kang and J. Li, “Displacement Model for Concrete Dam Safety Monitoring via Gaussian Process Regression Considering Extreme Air Temperature,” *J. Struct. Eng.*, vol. 146, no. 1, p. 05019001, 2020, doi: 10.1061/(asce)st.1943-541x.0002467.

[77] M. Rosenblatt, “Remarks on a Multivariate Transformation Author (s): Murray Rosenblatt Published by : Institute of Mathematical Statistics Stable URL : http://www.jstor.org/stable/2236692 REFERENCES Linked references are available on JSTOR for this article :,” *Ann. Math. Stat.*, vol. 23, no. 3, pp. 470–472, 1952.

[78] S. O. Rice, “Mathematical Analysis of Random Noise,” *Bell Syst. Tech. J.*, vol. 24, no. 1, pp. 46–156, 1945, doi: 10.1002/j.1538-7305.1945.tb00453.x.

[79] A. G. DAVENPORT, “Note on the Distribution of the Largest Value of a Random Function With Application To Gust Loading.,” *Proc. Inst. Civ. Eng.*, vol. 28, no. 2, pp. 187–196, 1964, doi: 10.1680/iicep.1964.10112.

[80] M. F. Huang, C. M. Chan, W. J. Lou, and K. C. S. Kwok, “Statistical extremes and peak factors in wind-induced vibration of tall buildings,” *J. Zhejiang Univ. Sci. A*, vol. 13, no. 1, pp. 18–32, 2012, doi: 10.1631/jzus.A1100136.

[81] A. Kareem, “Wind effects on structures: a probabilistic viewpoint,” *Probabilistic Eng. Mech.*, vol. 2, no. 4, pp. 166–200, 1987, doi: 10.1016/0266-8920(87)90009-9.

[82] K. R. Gurley, M. A. Tognarelli, and A. Kareem, “Analysis and simulation tools for wind engineering,” *Probabilistic Eng. Mech.*, vol. 12, no. 1, pp. 9–31, 1997, doi: 10.1016/s0266-8920(96)00010-0.

[83] A. M. Hasofer and N. C. Lind, “An exact and invariant first order reliability format,” *J. Eng. Mech. Div.*, vol. 100, no. July, pp. 111–121, 1974.

[84] S. R. Winterstein, T. C. Ude, C. a Cornell, P. Bjerager, and S. Haver, “Environmental Parameters for Extreme Response: Inverse Form with Omission Factors,” *Icossar-93*, no. August, pp. 9–13, 1993.

[85] A. Naess, “Technical note: On the long-term statistics of extremes,” *Appl. Ocean Res.*, vol. 6, pp. 227–228, 1984.

[86] L. E. Borgman, “Probabilities for Highest Wave in Hurricane,” *J. Waterw. Harb. Coast. Eng. Div.*, vol. 99, no. 2, p. Pg. 185-207, 1973.

[87] Nordenström, “Methods for predicting long-termdistributions of wave loads and probability of failure for ships DnV report no. 69-21-S. Det Norske Veritas (Høvik),” 1969.

[88] L. V. S. Sagrilo, A. Naess, and A. S. Doria, “On the long-term response of marine structures,” *Appl. Ocean Res.*, vol. 33, no. 3, pp. 208–214, 2011, doi: 10.1016/j.apor.2011.02.005.

[89] J. A. Battjes, “Long-Term Wave Height Distribution,” 1970.

[90] J. A. Battjes, “Long-term wave height distributions at seven stations around the British Isles,” 1972.

[91] Robert E. Melchers and A. T. Beck, “Integration and Simulation Methods,” *Structural Reliability Analysis and Prediction*. pp. 63–93, Oct. 02, 2017, doi: https://doi.org/10.1002/9781119266105.ch3.

[92] T. M. Lystad, “Long-term extreme buffeting response investigations for longspan bridges considering uncertain turbulence parameters based on field measurements,” NTNU, 2021.

Castellon D., Fenerci A., Øiseth O.

I

A comparative study of wind-induced dynamic response models of long-span bridges using artificial neural networks, support vector regression and buffeting theory

Journal of Wind Eng. Ind. Aerodyn. (p. 104484, vol. 209 2021)

Journal of Wind Engineering & Industrial Aerodynamics 209 (2021) 104484

Contents lists available at ScienceDirect

Journal of Wind Engineering & Industrial Aerodynamics

journal homepage: www.elsevier.com/locate/jweia

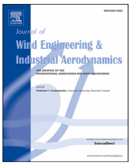

A comparative study of wind-induced dynamic response models of long-span bridges using artificial neural networks, support vector regression and buffeting theory

Dario Fernandez Castellon [*], Aksel Fenerci, Ole Øiseth

Department of Structural Engineering, Norwegian University of Science and Technology, Trondheim, Norway

A R T I C L E I N F O

Keywords:
Long-span bridges
Full-scaled measurements
Buffeting response
Multilayer perceptron
Supporting vector regression

A B S T R A C T

Long-span cable-supported bridges are structures susceptible to high dynamic responses due to the buffeting phenomenon. The current state-of-the-art method for buffeting response estimation is the buffeting theory. However, previous research has shown discrepancies between buffeting theory estimates and full-scale measured response, revealing a weakness in the theoretical models. In cases where wind and structural health monitoring data are available, machine learning algorithms may enhance the buffeting response estimation speed with less computational effort by bypassing the analytical model's assumptions. In this paper, multilayer perceptron and support vector regression models were trained with synthetic and full-scale measured data from the Hardanger Bridge. The analytical response was also computed from buffeting theory applied to a finite element model of the bridge, and the estimates are compared. The prediction accuracy was evaluated with the normalized root mean square error, the mean absolute percent error and the coefficient of determination (R2). The machine learning models trained with synthetic datasets achieved very high accuracy with normalized root mean square errors ranging from 1.46E-04 to 7.21E-03 and are therefore suitable for efficient surrogate modeling. Further, the support vector regression model trained with the full-scale measured dataset achieved the best accuracy compared with the other methods.

1. Introduction

The current state-of-the-art method for buffeting response prediction of long-span bridges is to use buffeting theory, which was first introduced by (Davenport A., 1962). Since Davenport's early works, the theory has been further developed by many researchers. Current advanced models are based on finite element formulations, which can account for unsteady self-excited forces (Scanlan and Tomko, 1971) (Davenport A., 1962) (Jain et al., 1996), nonlinearities (Diana et al., 2008) (Diana et al., 2005) (Chen and Kareem, 2003), skew winds (Zhu and Xu, 2005) and non-stationary winds (Hu, Xu, & Huang, Typhoon-induced non-stationary buffeting response of long-span bridges in complex terrain, 2013) (Hu et al., 2017). However, owing to the recent emergence of a large number of structural health monitoring (SHM) projects on prominent suspension bridges around the world, researchers have reported discrepancies in dynamic responses between their analytical predictions based on buffeting theory and the SHM data (Bietry et al., 1995) (Macdonald, 2003) (Xu and Zhu, 2005) (Cheynet et al., 2016) (Fenerci and Øiseth, 2017). Such discrepancies expose the weakness of analytical modeling of the complex phenomenon, presumably due to several assumptions inherent to buffeting theory.

In cases where monitoring data are present, an alternative solution may be found in using data-driven models based on machine learning. Machine learning is the scientific discipline of developing *algorithms* that can *learn* from data, which allows *prediction* based on existing trends within datasets. Therefore, such algorithms offer an approximation of a process by bypassing the complexity of its physics (Bishop C. M., 2006) (Alpaydin, 2020). The potential of machine learning algorithms in civil engineering applications has been recognized by many researchers, and their use is becoming increasingly common as more user-friendly software is becoming available. For instance, machine learning algorithms can be trained to replace the analytical load-response relationships by means of surrogate models. Such a strategy saves significant computational effort when many simulations are needed. Recently, such successful efforts have also been presented in the wind engineering community, (Fang et al., 2020) compared the capabilities of three machine learning surrogate models trained with a simulated dataset of

---

[*] Corresponding author.
E-mail address: dario.r.f.castellon@ntnu.no (D.F. Castellon).

https://doi.org/10.1016/j.jweia.2020.104484
Received 7 September 2020; Received in revised form 25 November 2020; Accepted 4 December 2020

Nomenclature

$\boldsymbol{Y}$	Machine learning output dataset
$\boldsymbol{X}$	Machine learning Input dataset
y_j^k	Output of a generic node
x_i^k	Input of a generic node
ϑ_j^k	Bias of a generic node
ε	SVR tolerance margin
C	Box constraint
α_i, α_i^*	Lagrange multipliers
$w_{i,j}^k$	Weight of a generic connection between two nodes
ξ_i, ξ_i^*	Slack variables
$\boldsymbol{r}$	Displacement vector in Cartesian coordinates
$\boldsymbol{\Phi}, \boldsymbol{\phi}_n$	Vibration modes
$\boldsymbol{\eta}$	Generalized coordinates
$\boldsymbol{M}, \boldsymbol{C}, \boldsymbol{K}$	Mass, damping and stiffness matrices, respectively
$\boldsymbol{Q}_n$	Wind load vector
$E_1E_2E_3$	Unit vector of the global coordinates
$e_1e_2e_3$	Unit vector of the local beam element
$ev_1ev_2ev_3$	Unit vector of the wind element coordinates
$\boldsymbol{T}_{G2Le}$	Transformation from global to local beam element
$\boldsymbol{T}_{G2Lw}$	Transformation from global to local wind element
$\boldsymbol{T}_{Lw2Le}$	Transformation from a local wind element to a local beam element
$\boldsymbol{T}_{E2S}$	Assembly matrix from local DOF to global DOF
q	Element wind load vector
$\boldsymbol{B}_q$	Buffeting load coefficient matrix
$\boldsymbol{V}_{Lw}$	Local wind velocity vector
D, B	Height and width of the girder
$C_D\ C_L\ C_M$	Force coefficients
R	Autocorrelation function
$\boldsymbol{S}$	Auto or cross-spectral density matrix
Coh	Square root of the coherence function
ρ	Air density
A_n	Spectral quantities
z	Height above the ground
$\boldsymbol{H}$	Frequency response matrix
$\sigma_y\ \sigma_z\ \sigma_\theta$	RMS of the structural response
$\chi, \Delta\chi$	Span-wise coordinate
V	Mean wind speed
I_n	Turbulence intensity
K_n	Decay coefficient
α	Vertical angle of attack
α_r, β_r	Rayleigh coefficients
ω, f	Circular and ordinary frequency

Subscripts

ae	Aerodynamic
Buff	Buffeting
Le	Local beam element
Se	Self-excited
Tot	Total
0	Still-air
u, w	Wind direction
r	response
k	Generic layer
i,j	Generic neuron or data sample index
y, z, θ	Horizontal, vertical and torsional responses

Superscripts

$\widehat{\blacksquare}$	Model estimation
$\overline{\blacksquare}$	Constant value, mean or specific for the case
$\tilde{\blacksquare}$	Modal property
$\dot{\blacksquare}$	Derivative with respect to time
$\blacksquare'$	Derivative
$\blacksquare^*$	Complex conjugate
$\blacksquare^{-1}$	Matrix inverse
$\blacksquare^T$	Matrix transpose

Functions

$g(\blacksquare)$	Activation function
$f(\blacksquare)$	governing function
$L(\blacksquare)$	Loss or cost function
$K(\blacksquare)$	Kernel function
$N(\blacksquare)$	Shape function

Abbreviations

SVR	Supporting vector regression
ANN	Artificial neural network
MLP	Multilayer perceptron
WIV	Wind induced vibration
R2	Coefficient of determination
MAPE	Mean average percentual error
RMS	Root mean square
RMSE	Root mean square error
NRMSE	Normalized Root mean squared error
BFT	Buffeting theory
CFD	Computational fluid dynamics
KKT	Karush–Kun–Tucker conditions
CLHS	Correlated latin hypercube sampling
SD	Standard Deviation

non-stationary wave and wind loads of a cable-stayed bridge to improve the efficiency of the response estimation. (Bernardini et al., 2015) proposed an alternative to wind tunnel testing based on surrogate models for computational fluid dynamics (CFD)-based aerodynamic shape optimization of bidimensional profiles using an evolutionary algorithm to update ordinary kriging surrogates. Furthermore (Wu and Kareem, 2011), showed how machine learning can be used to simulate complex nonlinearities in aerodynamic behavior by developing an approach to model aerodynamic nonlinearities in the time domain utilizing an artificial neural network (ANN) framework with embedded cellular automata (CA) applied to the hysteretic nonlinear behavior of aerodynamic systems, (Wang and Wu, 2020) proposed a knowledge-enhanced deep learning (KEDL) algorithm to simulate wind-induced linear/nonlinear structural dynamic responses in simulated dynamic systems. (Le and Caracoglia, 2020) used simulated datasets of a tornado-like wind field to develop an ANN-based surrogate model to approximate the structural fragilities of vertical structures subjected to tornadic wind loads. Surrogate models of flutter derivatives with ANN models trained with wind tunnel test data have been reported by (Chen et al., 2008) and (Rizzo and Caracoglia, 2020), while (Cid Montoya et al., 2018) developed a kriging surrogate model from CFD-based aeroelastic characterization of a bridge cross section and validated it with wind tunnel test measurements. (Nieto et al., 2020) extended the CFD-based kriging surrogate modeling approach proposed by (Cid Montoya et al., 2018) to assess the flutter response of bridges with twin-deck cross-sections. Additionally, the potential of machine learning to enhance automated response prediction tools from SHM systems is promising. Full-scale measurements of wind responses in bridges have recently been used for training machine learning algorithms, (Li et al., 2018) estimated vortex-induced vibrations on full-scale measured data of a cable-stayed bridge with machine learning, while (Wang et al., 2020) trained an ensemble model comprising a random forest (RF), long-short term memory (LSTM), and

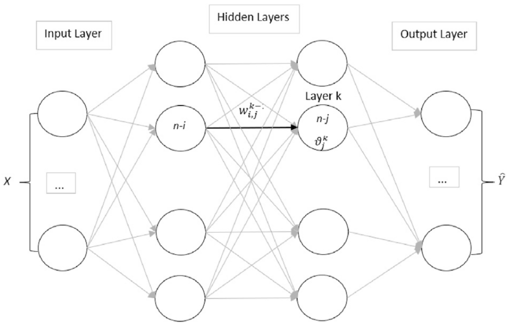

Fig. 1. Architecture of an ANN

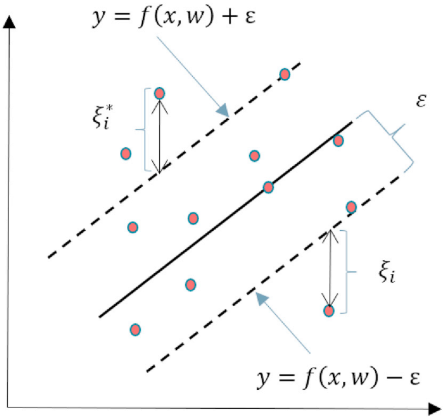

Fig. 2. Schematic representation of SVR with slack variables.

Gaussian process regression (GPR) with measured wind data from the cable-stayed Sutong Yangtze River Bridge in China to forecast wind gusts affecting traffic operations. However, neither of these directly addressed the effect of buffeting responses. Therefore, many uncertainties must be explored as there are no relevant studies based on full-scale measurements for buffeting response estimation in long-span bridges. The deployment and operativity of machine learning algorithms in this field are among the primary challenges to assess. Nonetheless, the effectiveness of machine learning tools shall be explored in terms of which type of algorithm yields better estimates and whether it can provide any improvement with respect to the existing analytical models.

Therefore, this study intends to provide further insight toward understanding the buffeting phenomena of long-span bridges by implementing machine learning algorithms trained with full-scale monitoring data. To address this aim, long-term wind and acceleration monitoring data from the Hardanger Bridge in Norway are used. Two different machine learning techniques, namely, support vector regression (SVR) and multilayer perceptron (MLP) models, are used to model the wind-response relationship. First, the models are trained using analytical predictions to test their capabilities. The remarkable accuracy of these models in predicting the analytical response suggests surrogate modeling based on machine learning is certainly a viable option in cases where many simulations are needed. Owing to the confidence gained from synthetic data, the models are then trained using full-scale monitoring data. The results show that reasonably accurate predictions of the dynamic response can be reached by using only wind characteristics data. Finally, the predictions based on machine learning algorithms are compared to the analytical results based on buffeting theory.

2. Machine learning methods for buffeting response prediction

2.1. Modeling the wind-response relationship

The buffeting responses of long-span suspension bridges can be predicted analytically using buffeting theory. In the frequency domain, the wind field is modeled by a cross-spectral density matrix defined by the time-averaged wind speed and several turbulence-related parameters. Then, by means of buffeting theory, the root mean square (RMS) of the dynamic response components are obtained.

Here, an alternative data-driven approach using machine learning algorithms will be used to estimate the dynamic response of a long-span suspension bridge. The objective of machine learning is to find patterns within a dataset to then make predictions based on the discovered patterns. Applied to buffeting response estimation, machine learning can approximate the unknown function, $f(X)$, between the wind parameters of the cross-spectral density function and the RMS of the bridge's dynamic responses, defined as the input tensor (X) and the target tensor (Y), respectively. Machine learning algorithms fit $f(X)$ over a large amount of data samples in the three different stages of the so-called learning procedure: training, validation, and testing. Hence, the dataset is divided into training, validation, and testing sets. The training dataset comprises the samples used for fitting the model parameters (Ripley, 1996). The validation dataset comprises samples that are used to evaluate the performance of the fitted trained model (James et al., 2013) and subsequently adjust the model hyperparameters (Ripley, 1996). Finally, the test dataset comprises the samples that follows the same probabilistic distribution of the training dataset but has not been fed into the model, therefore evaluating the generalization ability of the model (Ripley, 1996).

Equation (1) shows the machine learning process for the wind-response relationship.

$$\text{Given } X_i \text{ and } Y_i \text{ Find } f(X) \therefore Y \cong f(X) \;\; \widehat{Y}_j = f(X_j) \tag{1}$$

The indexes i and j represent the training and testing datasets, respectively.

Two different machine learning models were implemented. The first model is an ANN called an MLP, which was use because of its simplicity and common use in the literature. The second was SVR, which was used because of its remarkable generalization ability and performance (Awad and Khanna, 2015). Further details will be given in this section.

2.2. Artificial neural networks (ANN) – multilayer perceptron (MLP) model

An ANN is an algorithm that mimics the functioning of biological brains by assembling *layered neurons connected* to each other. A neuron (also known as a unit or node) is an operational entity that stores and distributes information (Rosenblatt, 1958). The neurons are organized in sets called layers, and the neurons within one layer are connected to those in the subsequent layer. The layer connections transmit information within the neurons and, mathematically, are the arrays governing the transformation relationships. The value of a neuron in an arbitrary layer is the scalar product between its transformation array and the output of the neurons in the previous layer; then, the neuron is activated whenever its value surpasses a certain threshold (Rosenblatt, 1958). The type of neural network used in this study is the so-called MLP (Rosenblatt, 1961), which is schematically shown in Fig. 1.

In Equation (2), y_j^k is the output of the j-th node in the k-th arbitrary layer of an MLP and is related to an activation bias ϑ_j^k and connection weights $w_{i,j}^{k-1}$, where x_i^{k-1} is the value of the i-th node of the previous layer. Then, a nonlinear activation function, $g(x)$, is applied to the result

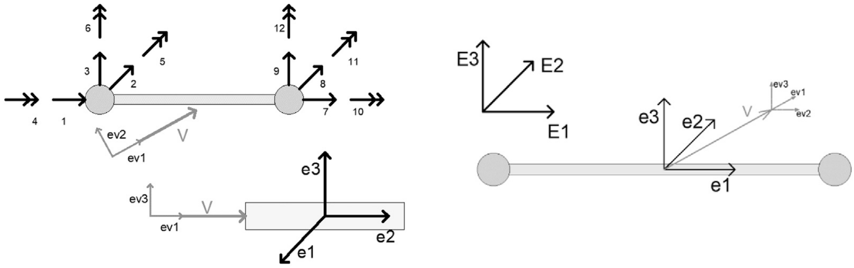

(a) (b)

Fig. 3. Local coordinate system of the beam element: (a) DOF of the beam element. (b) Wind actions on the beam element.

$$\boldsymbol{T}_{G2Le} = \begin{bmatrix} \boldsymbol{e}_1^T \\ \boldsymbol{e}_2^T \\ \boldsymbol{e}_3^T \end{bmatrix} \tag{15}$$

$$\boldsymbol{T}_{G2Lw} = \begin{bmatrix} \boldsymbol{ev}_1^T \\ \boldsymbol{ev}_2^T \\ \boldsymbol{ev}_3^T \end{bmatrix} \tag{16}$$

$$\boldsymbol{T}_{Lw2Le} = \boldsymbol{T}_{G2Le}\boldsymbol{T}_{G2Lw}^T \tag{17}$$

Table 1
Range and intervals for the uniform grid simulated training dataset.

Wind Feature	Minimum	Maximum	Number of Intervals
V	4	35	10
σ_u	0.2	5.2	10
σ_w	0.1	2	10
K_u	2.5	15	5
K_w	1.5	25	5

Table 2
Synthetic datasets features summary.

Dataset	Simulation strategy	Distribution	Size
Training uniform	Uniform grid	Uniform	25,000
Training CLHS	CLHS	Observed	3500
Testing CLHS	CLHS	observed	500

(Bishop C. M., 1994). The subsequent operations in matrix notation are presented in Equation (3). The feedforward mapping process (Equation (4)) is then obtained by assembling the abovementioned operations until the model's final M layer is reached and by computing the model estimation of the output $\widehat{Y}$, where $f(X)$ is the process-governing function.

$$y_j^k = g\left(\sum_{i=1,j=j}^{N} w_{i,j}^{k-1} x_i^{k-1} + \vartheta_j^k\right) \tag{2}$$

$$Y^k = g\left\{\left(W_i^{k-1}\right)^T * \ X^{k-1} + \theta^k\right\} \tag{3}$$

$$\widehat{Y} = f\left\{\left(W_i^{M-1}\right)^T \dots g\left\{\left(W_i^1\right)^T X^1\right\} + \theta^M\right\} \tag{4}$$

The actual output of the process or target is known in the training stage. Thus, the ANN performance is obtained by comparing the target with the model estimation with a "loss" function $L(\widehat{y}_j, y_j)$.

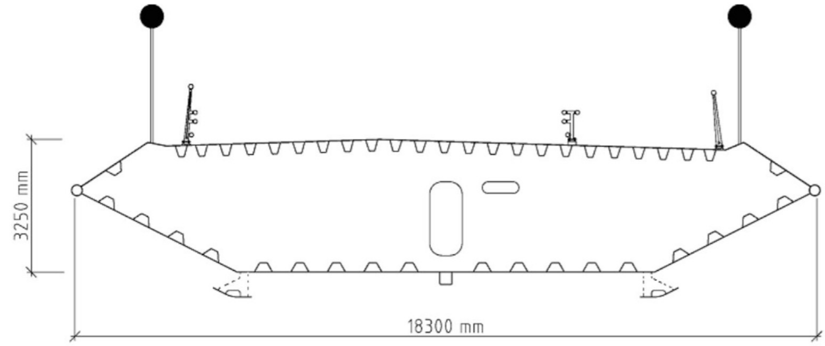

Fig. 4. Cross section of the Hardanger bridge.

Table 3
Natural frequencies of the still-air mode.

Mode	Frequency Hz	Circular Frequency	Damping Ratio	Characteristic
1	0.050	0.315	0.32%	Symmetric lateral vibration of the deck
2	0.098	0.616	0.41%	Asymmetric lateral vibration of the deck
3	0.110	0.694	0.45%	Asymmetric vertical vibration of the deck
4	0.141	0.884	0.54%	Symmetric vertical vibration of the deck
5	0.169	1.062	0.63%	Symmetric lateral vibration of the deck
6	0.197	1.239	0.72%	Symmetric vertical vibration of the deck
7	0.211	1.326	0.76%	Asymmetric vertical vibration of the deck
8	0.225	1.414	0.81%	Symmetric lateral vibration of the cables
9	0.233	1.461	0.84%	Asymmetric lateral vibration of the cables
10	0.234	1.468	0.84%	Asymmetric lateral vibration of the deck and the cables
11	0.244	1.533	0.87%	Symmetric lateral vibration of the deck and the cables
12	0.272	1.709	0.97%	Symmetric vertical vibration of the deck
13	0.293	1.841	1.04%	Asymmetric lateral vibration of the deck
14	0.33	2.073	1.16%	Asymmetric vertical vibration of the deck
15	0.36	2.262	1.27%	Symmetric torsional vibration of the deck

Table 4
Load coefficients from wind tunnel testing

Load Coefficients	$\overline{C}_D$	$C_D^{'}$	$\overline{C}_L$	$C_L^{'}$	$\overline{C}_M$	$C_M^{'}$
Value	1.05	0.00	−0.363	2.2	−0.017	0.786

The mathematical objective of the learning process is to minimize the loss function. This minimization is achieved by sending the estimation error of Equation (4) through all the previous layers within the network; this operation results in an iterative optimization procedure known as backpropagation (Rumelhart et al., 1986). It is worth noting that the backpropagation procedure refers to only the error feeding step and is independent of the optimization algorithm used.

The original input signals are fixed to the dataset; therefore, the only parameters to be updated in each iteration are the network weights and biases. Thus, the optimization problem can be written as Equation (5).

$$find\left(W^{k\in\{1\ :M-1\}}\ \&\ \theta^{k\in\{1:M\}}\right)\therefore L\left(\widehat{y}_j,\ y_j\right)=\min(L) \tag{5}$$

2.3. Supporting vector regression (SVR) model

SVR is the application of the support vector approximation to a regression problem using an ε-insensitive loss function (Vapnik, 1995). The objective of the tool is to find a function $f(x)$ that, from a given dataset of input and output features $\{x_i,y_i|\ldots|x_n,y_n\}$, approximates y_i with a certain tolerance ε. The regression estimation can be obtained with the linear function shown in Equation (6).

$$f(x)=x^{'}w+\vartheta \tag{6}$$

Introducing the ε-insensitive loss function L equal to zero when the difference between the estimation $f(x)$ and the target is less than ε, a constraint shown in Equation (7) is added to the problem.

$$L(y-f(x,w))=\begin{cases}0 & if|y-f(x,w)|\le\varepsilon\\ |y-f(x,w)| & otherwise\end{cases} \tag{7}$$

To make the solution more feasible, the tolerance margin is softened by adding a set of slack variables ξ_i and ξ_i^*, as shown in Fig. 2.

The optimization problem becomes Equation (8), where C is the so-called box constraint, which is a positive-valued parameter that imposes a penalty on the estimations outside the ε-margin and thus helps to balance the accuracy of the model.

$$\begin{aligned}&minimize && \frac{1}{2}w^2+C\sum_{i=1}^{N}\xi_i+\xi_i^*\\ &with\ constraints: && \begin{cases}y_i-f(x,w)\le\varepsilon+\xi_i\\ f(x,w)-y_i\le\varepsilon+\xi_i^*\\ \xi_i,\xi_i^*\ge 0\end{cases}\end{aligned} \tag{8}$$

Solving this optimization problem with inequality constraints is equivalent to finding the saddle point in the Lagrange function. By introducing α_n and α_n^* as Lagrange multipliers, the weights (w parameters) can be found by Equation (9), and the model estimation is computed by expanding the so-called support vectors in Equation (10).

$$w=\sum_{i=1}^{N}(\alpha_i-\alpha_i^*)x_i \tag{9}$$

$$f(x)=\sum_{i=1}^{N}(\alpha_i-\alpha_i^*)(x_i^{'}x)+\vartheta \tag{10}$$

The parameters ϑ can be obtained by exploiting the Karush–Kun–Tucker (KKT) conditions (William, 1939) (Kuhn and Tuker, 1951), which state that at the optimal solution, the product between the dual variables and constraints vanishes. Then the constraints of Equation (11) are added to the optimization problem.

$$\begin{aligned}&\alpha_i\left(\varepsilon+\xi_i-y_i+x_i^T\ w+\vartheta\right)=0\\ &\alpha_i^*\left(\varepsilon+\xi_i^*+y_i-x_i^T\ w-\vartheta\right)=0\\ &\xi_i(\mathrm{C}-\alpha_i)=0\\ &\xi_i^*\left(\mathrm{C}-\alpha_i^*\right)=0\end{aligned} \tag{11}$$

To extend the formulation to nonlinear regression problems, the dot product $(x_i^{'}x)$ must be replaced with a nonlinear mapping function, known as the kernel function $K(x_i^{'}x)$.

$$f(x)=\sum_{i=1}^{N}(\alpha_i-\alpha_i^*)K(x_i^{'}x)+\vartheta \tag{12}$$

3. Training data

3.1. Synthetic data: analytical predictions

Before extending the model to full-scale measurements, it was tested on an ideal case of simulated datasets. The datasets were obtained by simulating random wind fields and calculating the corresponding RMS dynamic response of the bridge using multimode buffeting theory in the frequency domain.

3.1.1. Multimode buffeting theory in the frequency domain

The buffeting response of the bridge was computed in the frequency domain following classical multimode theory (Chen et al., 2000) (Jain et al., 1996) (Katsuchi et al., 1998). The theory requires the following assumptions: The bridge is idealized as a line-like structure, the wind field is approximated as homogenous and stationary, and the wind action

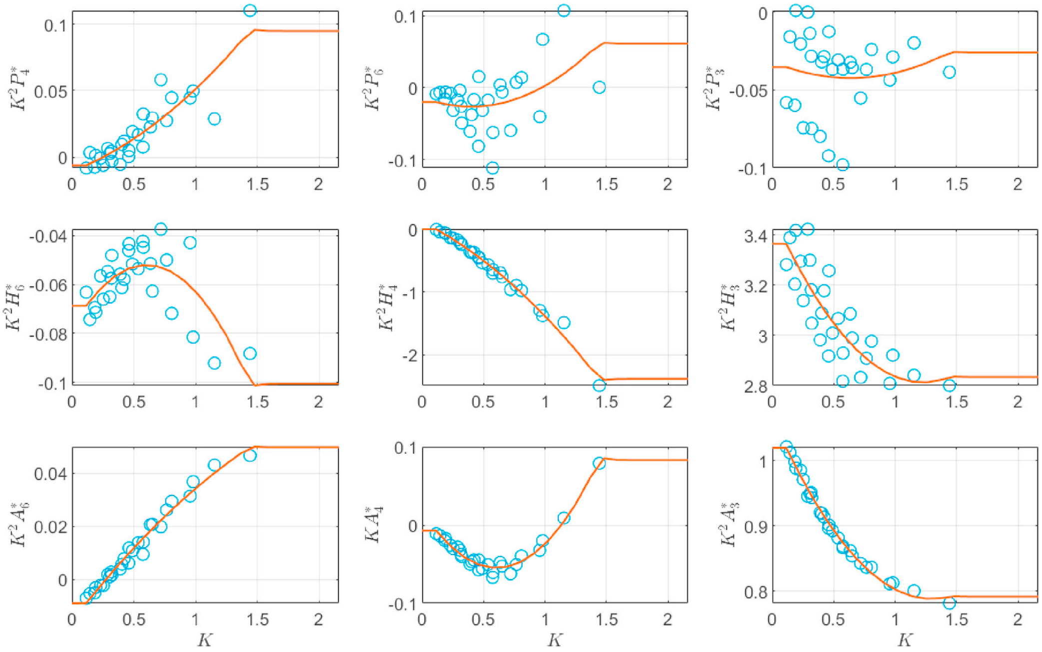

Fig. 5. Dimensionless aerodynamic derivatives related to aeroelastic stiffness as function of reduced frequency. Points are experimental data, continuous line fitted function.

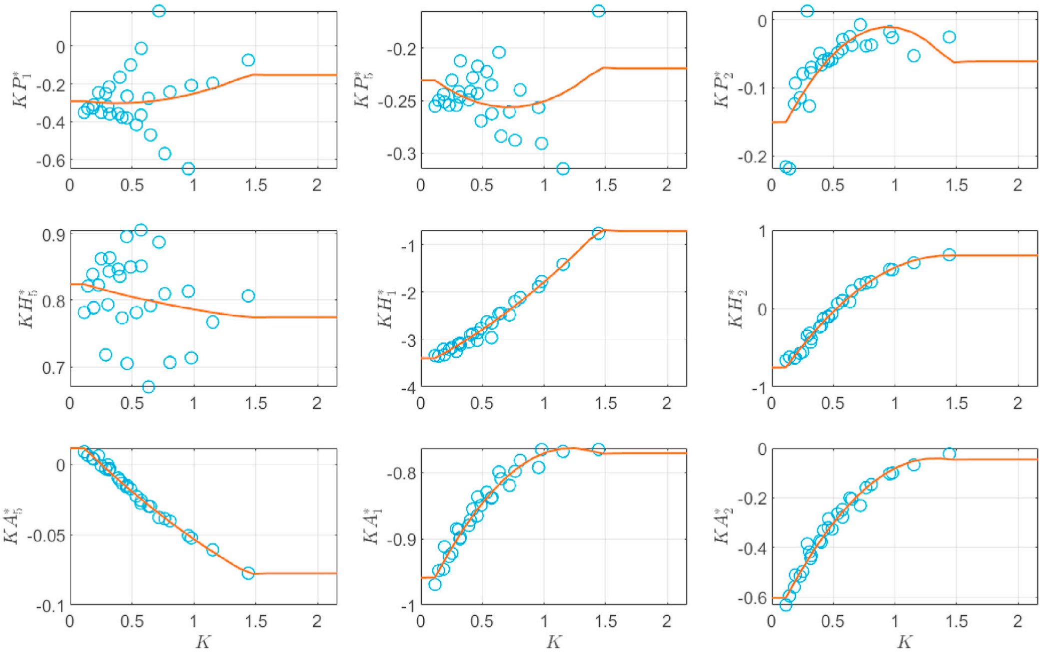

Fig. 6. Dimensionless aerodynamic derivatives related to aeroelastic damping as function of reduced frequency. Points are experimental data, continuous line fitted function.

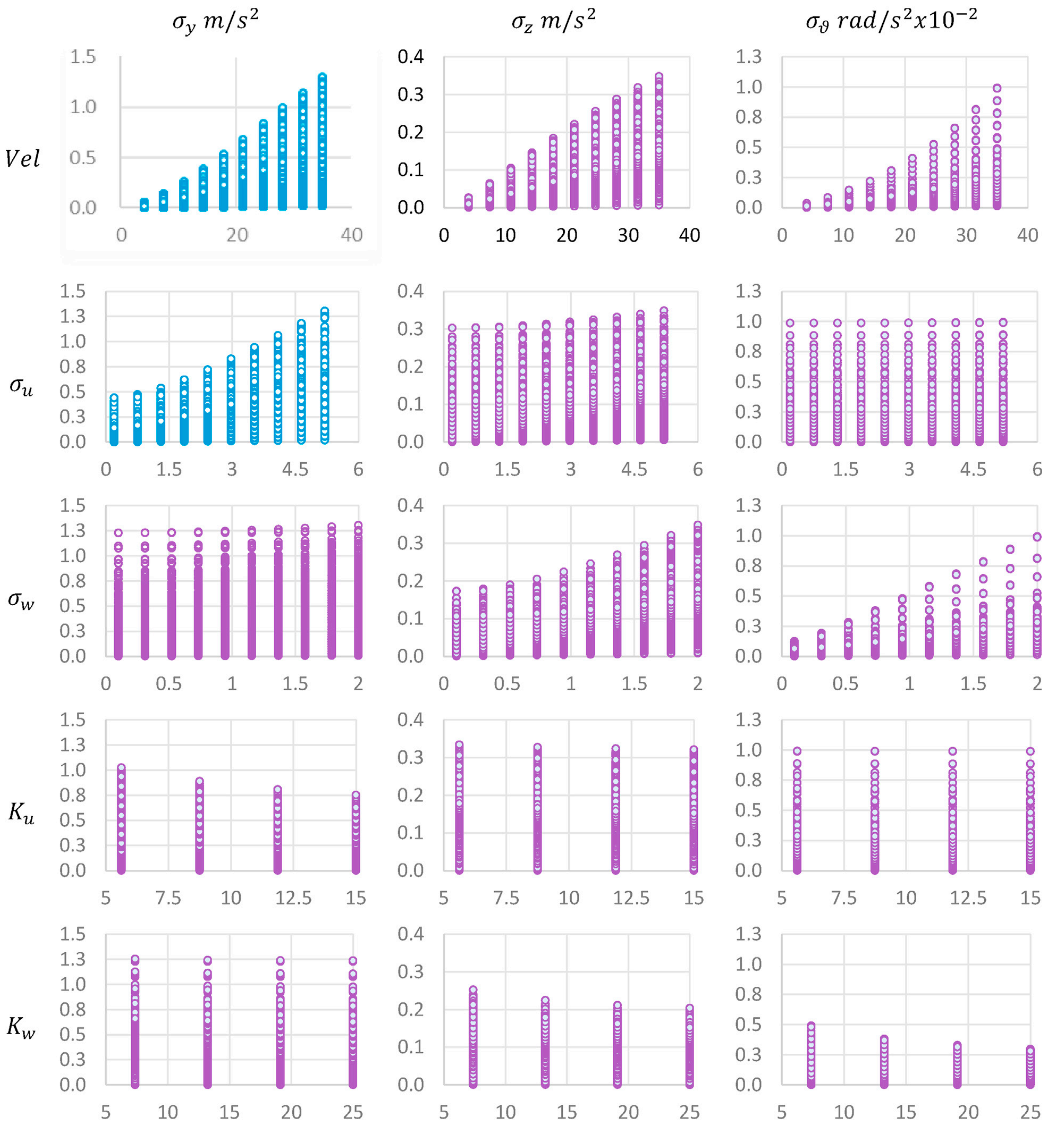

Fig. 7. Uniform grid training dataset (simulated data).

and displacements are referred to as the shear center of the bridge girder and can be separated into a time-invariant mean and a randomly fluctuating part. For surrogate model trained with the synthetic datasets, the aeroelastic forces were computed with the quasi-steady theory. In contrast, aerodynamic derivatives were included in the formulation for the case of comparison with full-scaled measurements. In both cases the experimental data came from the wind tunnel test reported by (Siedziako et al., 2017).

Multimodal theory represents the structural quantities using the mode shapes as generalized coordinates. Then, the structural displacements due to buffeting, $\boldsymbol{r}$, in a Cartesian coordinate system are represented by the sum of the products of the selected natural mode shapes, $\boldsymbol{\Phi}$, and the respective generalized coordinates$\boldsymbol{\eta}$, as in Equation (13).

$$\boldsymbol{r}(\chi,t) = \boldsymbol{\Phi}(\chi)\boldsymbol{\eta}(t)\ \boldsymbol{\Phi}(\chi) = [\,\boldsymbol{\phi}_1 \dots \boldsymbol{\phi}_i \dots \boldsymbol{\phi}_N]^T\ \boldsymbol{r}(\chi,t) = [\,r_y\ r_z\ r_\theta]^T\ \boldsymbol{\eta}(t) = [\,\eta_1 \dots \eta_i \dots \eta_N]^T\ \boldsymbol{\phi}_i = .[\,\boldsymbol{\phi}_y\ \boldsymbol{\phi}_z\ \boldsymbol{\phi}_\theta]^T \tag{13}$$

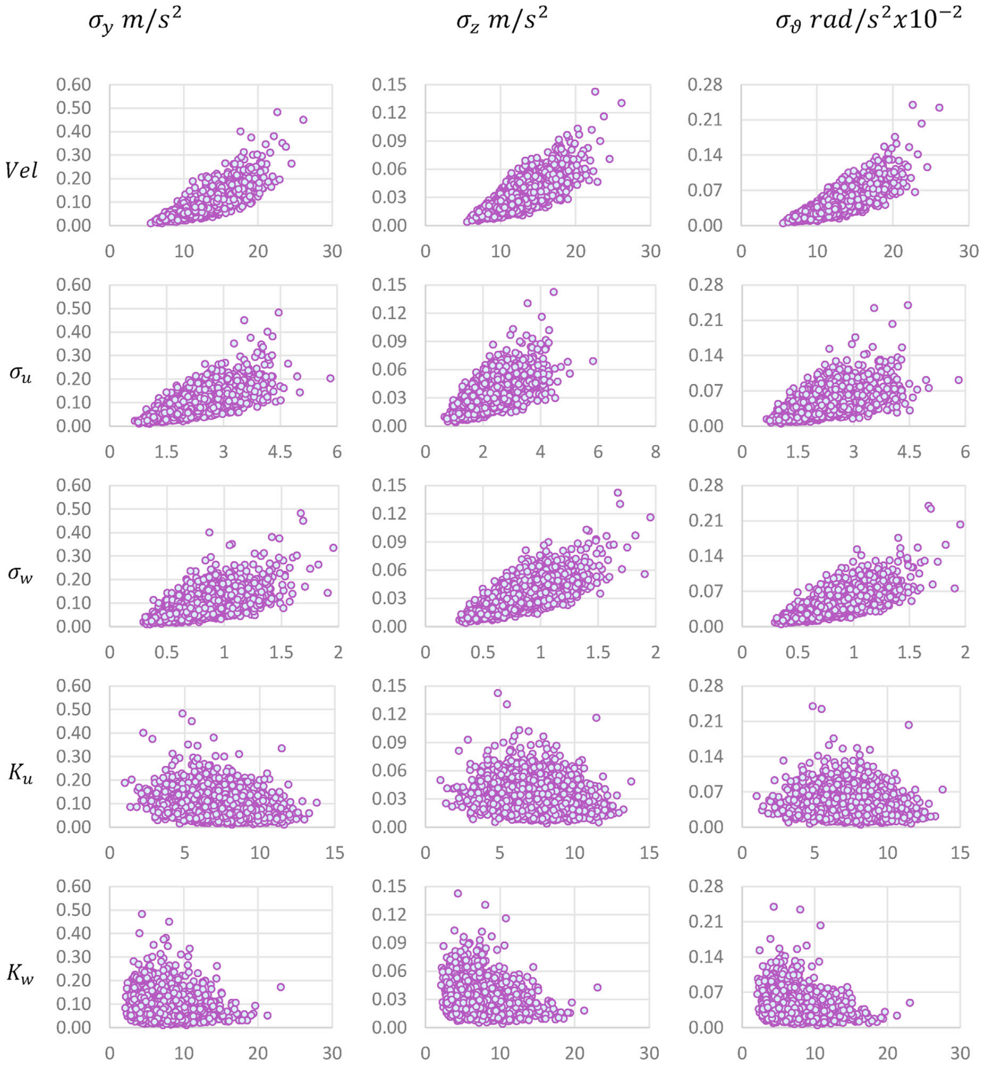

Fig. 8. Random CLHS training dataset (simulated data).

Then, the system's generalized equation of motion is as shown in Equation (14).

$$\begin{aligned}&\tilde{\boldsymbol{M}}_0\,\ddot{\boldsymbol{\eta}}(t)+\left(\tilde{\boldsymbol{C}}_0\right)\dot{\boldsymbol{\eta}}(t)+\left(\tilde{\boldsymbol{K}}_0\right)\boldsymbol{\eta}(t)=\tilde{\boldsymbol{Q}}_{Tot}(t)\\&\boldsymbol{Q}_{Tot}(t)=\boldsymbol{Q}_{buff}(t)+\boldsymbol{Q}_{se}(t)\end{aligned}\tag{14}$$

Here, $\tilde{\boldsymbol{M}}_0, \tilde{\boldsymbol{C}}_0$ and $\tilde{\boldsymbol{K}}_0$ represent the structural still-air generalized mass, damping and stiffness matrices, respectively, which are diagonal matrices. These structural matrices are obtained from a finite element model of the Hardanger Bridge. Finally, the term $\tilde{\boldsymbol{Q}}_{Tot}$ stands for the total generalized wind load including the buffeting and the self-excited forces.

3.1.2. Buffeting force using finite element discretization

Multimodal theory assumes that the structures are line-like. However, suspension bridges have complex shapes; therefore, here, the use of a beam finite element discretization approach is proposed to apply the wind forces in Equation (14). Furthermore, the beam element forces can be transformed into generalized coordinates using the multimodal approach.

A generic structure can be discretized with beam finite elements with 12 degrees of freedom, as shown in Fig. 3 (a). Then, the wind action over a generic beam element is shown in Fig. 3 (b). The three coordinate systems shown in Fig. 3 are the global coordinate system defined by its unit vector $\{E_1, E_2, E_3\}$, the beam element local coordinate system with unit vector $\{e_1, e_2, e_3\}$ and the wind field system with unit vector $\{ev_1, ev_2, ev_3\}$. The transformation scheme from the global coordinate system to the local coordinate system of the beam element is shown in Equation (15) and to the wind field local coordinate system is shown in Equation (16). Hence, Equation (17) shows the transformation from the wind system to the local coordinate system of the beam element.

The vector of nodal buffeting forces is obtained from the principle of virtual work using the shape functions $N(\chi)$ and denoting the wind forces

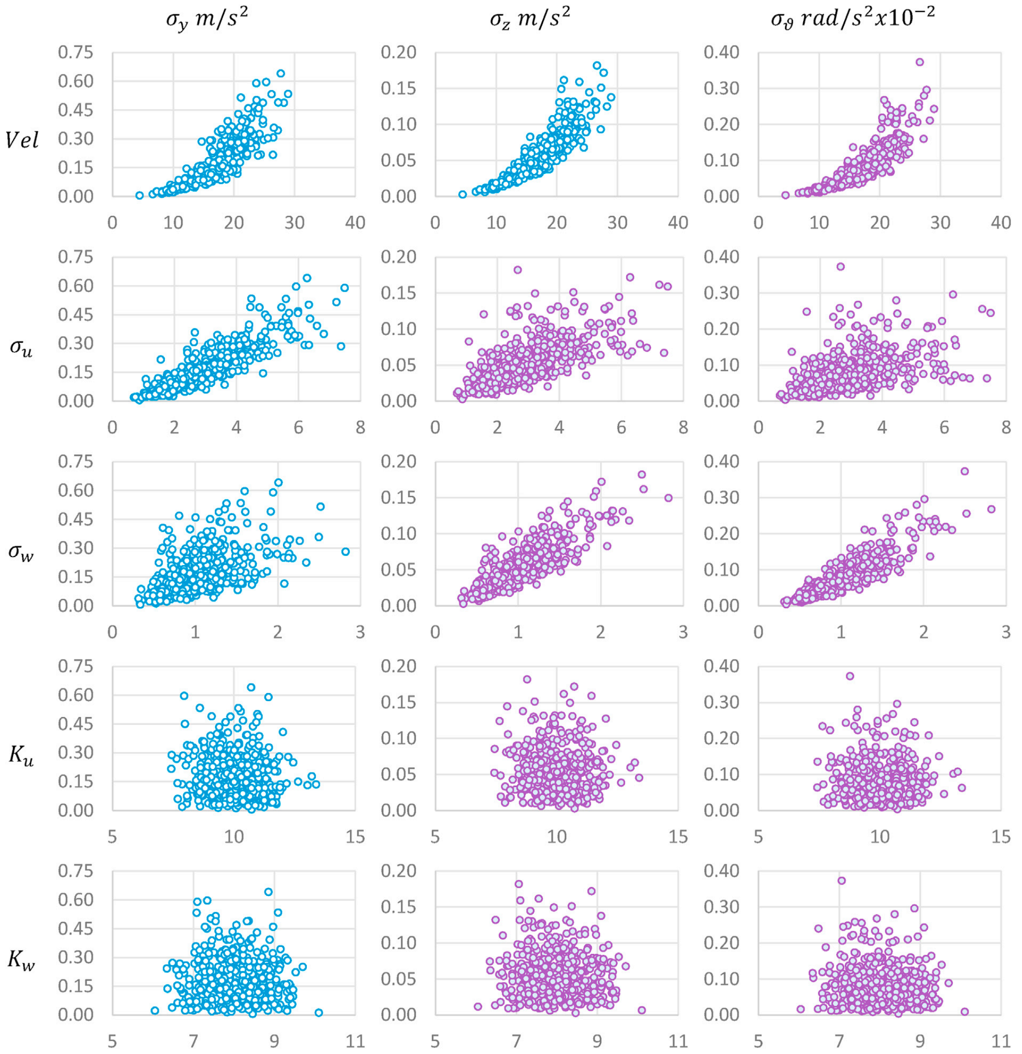

Fig. 9. Testing dataset (simulated data).

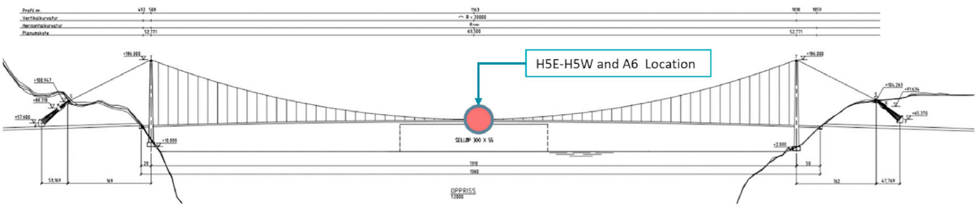

Fig. 10. Hardanger Bridge sensor layout.

in the beam element by $q_{buff}(\chi,t)$ (Equation (18)).

$$\boldsymbol{Q}_{\boldsymbol{Le\ buff}}(\boldsymbol{t}) = \int_0^L \boldsymbol{N}(\boldsymbol{\chi})\boldsymbol{q}_{\boldsymbol{buff}}(\boldsymbol{\chi},\boldsymbol{t})\boldsymbol{d\chi}\ q_{buff}(\chi,t) = \boldsymbol{B}_q(\chi)\boldsymbol{T}_{Lw2Le}\ \boldsymbol{V}_{Lw}(\chi,t) \tag{18}$$

$\boldsymbol{V}_{Lw} = [v_1\quad v_2\quad v_3]^T$ is the vector containing the wind turbulence component in the wind coordinate system, and thus, it shall be transformed into the local coordinate system of the beam. Furthermore, matrix $\boldsymbol{B}_q$can be obtained from Equation (19).

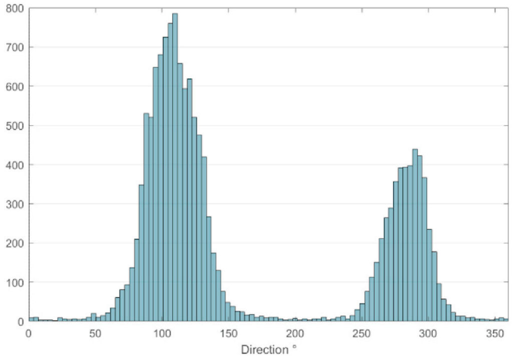

Fig. 11. Histogram of the incoming wind directions from the A6 midspan anemometer of the Hardanger Bridge.

$$\boldsymbol{B}_q(\omega) = \frac{1}{2}\rho B\,\overline{V}\begin{bmatrix} 0 & 0 & 0 \\ 0 & 2\left(\frac{D}{B}\right)\overline{C}_D & \left\{\left(\frac{D}{B}\right)C_D' - \overline{C}_L\right\} \\ 0 & 2\overline{C}_L & \left\{\left(\frac{D}{B}\right)\overline{C}_D + C_L'\right\} \\ 0 & 2B\overline{C}_M & BC_M' \end{bmatrix} \tag{19}$$

where ρ the density of the air, ω the circular frequency, D and B the effective depth and width of the girder cross section, respectively. $\overline{V}$ is the mean wind speed. $\overline{C}_D, \overline{C}_L$ & $\overline{C}_M$ are the drag, lift and moment coefficients at the linearization position from the wind tunnel test and C'_D,C'_L,$C'_M$are their respective derivates with respect to the angle of attack, these coefficients are given in Table 4 from experimental data and the quantity $\frac{D}{B}$ is introduced as a normalization term.

To assemble the complete vector of nodal buffeting forces, the contribution of all the beam element local forces are transformed into the global coordinate system and summed (Equation (20)). Furthermore, the dependence of $\boldsymbol{B}_q$ and $\boldsymbol{V}_{Lw}$ on the integration variable x is ignored by assuming a uniform shape of the beam elements and that their length is small compared to the spatial variations in the wind field.

$$\boldsymbol{Q}_{buff}(t) = \sum_i^N \boldsymbol{T}_{E2S,i}\,\boldsymbol{T}^T_{G2Le,i}G_i\boldsymbol{B}_{q,i}\boldsymbol{T}_{Lw2Le,i}\,\boldsymbol{V}_{Lw,i}(t) \tag{20}$$

where $\boldsymbol{T}_{E2S}$ is the assembly matrix from the local degrees of freedom of beam element to the global degrees of freedom of the structure and $G_i = \int_0^L N(\chi)d\chi$.

To express the quantities in the frequency domain, the cross-spectral density of the buffeting force is obtained as the discrete Fourier transform of its cross-correlation function

$$R_{\boldsymbol{Q}_{buff}}(\tau) = E\left[\boldsymbol{Q}_{buff}(t)\,\boldsymbol{Q}^T{}_{buff}(t+\tau)\right]\;S_{\boldsymbol{Q}_{buff}}(\omega) = \sum_i^N$$

$$\times\sum_j^N \boldsymbol{T}_{E2S,i}\,\boldsymbol{T}^T_{G2Le,i}G_i\boldsymbol{B}_{q,i}\boldsymbol{T}_{Lw2Le,i}\,S_V(\Delta x,\omega)\boldsymbol{T}^T_{Lw2Le,j}\,\boldsymbol{B}^T_{q,j}\,\boldsymbol{G}^T_j\boldsymbol{T}_{G2Le,j}\boldsymbol{T}^T_{E2S,j} \tag{21}$$

where $S_V(\Delta\chi,\omega)$ represents the cross-power spectral density (CPSD) matrix of the wind field. Then, the cross-spectral density of the buffeting force can be transformed into the generalized coordinate system:

$$\tilde{S}_{Q_{buff}}(\tau) = \boldsymbol{\Phi}(\chi)S_{Q_{buff}}(\omega)\boldsymbol{\Phi}^T(\chi) \tag{22}$$

Applying a similar approach to the self-excited forces, Equation (23) shows the nodal vector of self-excited forces and the wind forces $q_{se}(x,t)$ in the beam element.

$$\boldsymbol{Q}_{Le\,se}(\boldsymbol{t}) = \int_0^L \boldsymbol{N}(\boldsymbol{\chi})\boldsymbol{q}_{se}(\boldsymbol{\chi},\boldsymbol{t})\boldsymbol{d\chi}\;q_{se} = C_{ae}\dot{\boldsymbol{r}}(\chi,t) + K_{ae}\boldsymbol{r}(\chi,t) \tag{23}$$

where $C_{ae}\,and\,K_{ae}$ are the aeroelastic damping and stiffness matrices, respectively, and are given in Equations (24) and (25). Equations (26) and (27) present the matrices in the generalized coordinate system.

$$C_{ae} = \frac{1}{2}\rho\,\omega B^2\begin{bmatrix} P_1^* & P_5^* & BP_2^* \\ H_5^* & H_1^* & BH_2^* \\ BA_5^* & BA_1^* & B^2A_2^* \end{bmatrix} \tag{24}$$

$$K_{ae} = \frac{1}{2}\rho\,\omega^2B^2\begin{bmatrix} P_4^* & P_6^* & BP_3^* \\ H_6^* & H_4^* & BH_3^* \\ BA_6^* & BA_4^* & B^2A_3^* \end{bmatrix} \tag{25}$$

$$\tilde{C}_{ae} = \int_L \boldsymbol{\phi}_n^T C_{ae}(\omega^*)\boldsymbol{\phi}_m\,d\chi \tag{26}$$

$$\tilde{K}_{ae} = \int_L \boldsymbol{\phi}_n^T K_{ae}(\omega^*)\boldsymbol{\phi}_m\,d\chi \tag{27}$$

Were $P^*_{1,2\ldots,6}H^*_{1,2\ldots,6}andA^*_{1,2\ldots,6}$ Denote the dimensionless aerodynamic derivatives.

Finally, the cross-spectral density of the response in the global Cartesian coordinate system is:

$$S_r(\omega,\chi_r) = \Phi(\chi_r)\left\{\left[H(\omega)S_{\tilde{Q}_{buff}}(\omega)\right]H^*(\omega)\right\}\Phi^T(\chi_r) \tag{28}$$

with the following transfer function:

$$H(\omega) = \left[-\tilde{M}_0\omega^2 + \left(\tilde{C}_0 - \tilde{C}_{ae}\right)i\omega + \left(\tilde{K}_0 - \tilde{K}_{ae}\right)\right] \tag{29}$$

By extracting the response spectrum at midspan and integrating over the frequency, it is possible to obtain the standard deviation of the responses and thus the target output features:

$$Y_i = \left[\sigma_y\;\sigma_z\;\sigma_\theta\right]_i = \sigma_r = \int_{-\infty}^{\infty} S_r\left(\omega,\chi_{r\,midspan}\right)d\omega \tag{30}$$

3.1.3. Wind field modeling

3.1.3.1. Cross spectral density function. The cross-spectral density function of the wind turbulent field, $S_V(\Delta\chi,\omega)$, required in Equation (21) is defined as:

$$\boldsymbol{S}_V(\boldsymbol{\Delta\chi},\boldsymbol{\omega}) = \begin{bmatrix} \boldsymbol{S}_{uu}(\boldsymbol{\Delta\chi},\boldsymbol{\omega}) & \boldsymbol{S}_{wu}(\boldsymbol{\Delta\chi},\boldsymbol{\omega}) \\ \boldsymbol{S}_{uw}(\boldsymbol{\Delta\chi},\boldsymbol{\omega}) & \boldsymbol{S}_{ww}(\boldsymbol{\Delta\chi},\boldsymbol{\omega}) \end{bmatrix} \tag{31}$$

$$S_{nm}(\Delta\chi,\omega) = Coh_{nm}(\Delta\chi,\omega)\sqrt{S_n(f)S_m(f)} \tag{32}$$

The terms $S_n,\ n\in\{u,w\}$ and $S_m,\ m\in\{u,\ w\}$represent the auto-spectral density function of the turbulence components at an element location x_i. The normalized cospectrum is represented by Coh_{nm}. Furthermore, $S_{nm}\;n,m\in\{u,w\}$ represents the cross-spectral density function of the beam elements separated by a distance $\Delta\chi$.

The variability of S_V is considered in the wind model parameters. Applied to buffeting response estimation with machine learning, the chosen input features (X) are the incoming mean wind speed (V), the along-wind and vertical turbulence standard deviation $(\sigma_{u,}\ \sigma_w)$ and the decay coefficients $(K_{u,}K_w)$. Furthermore, the auto-spectral density is

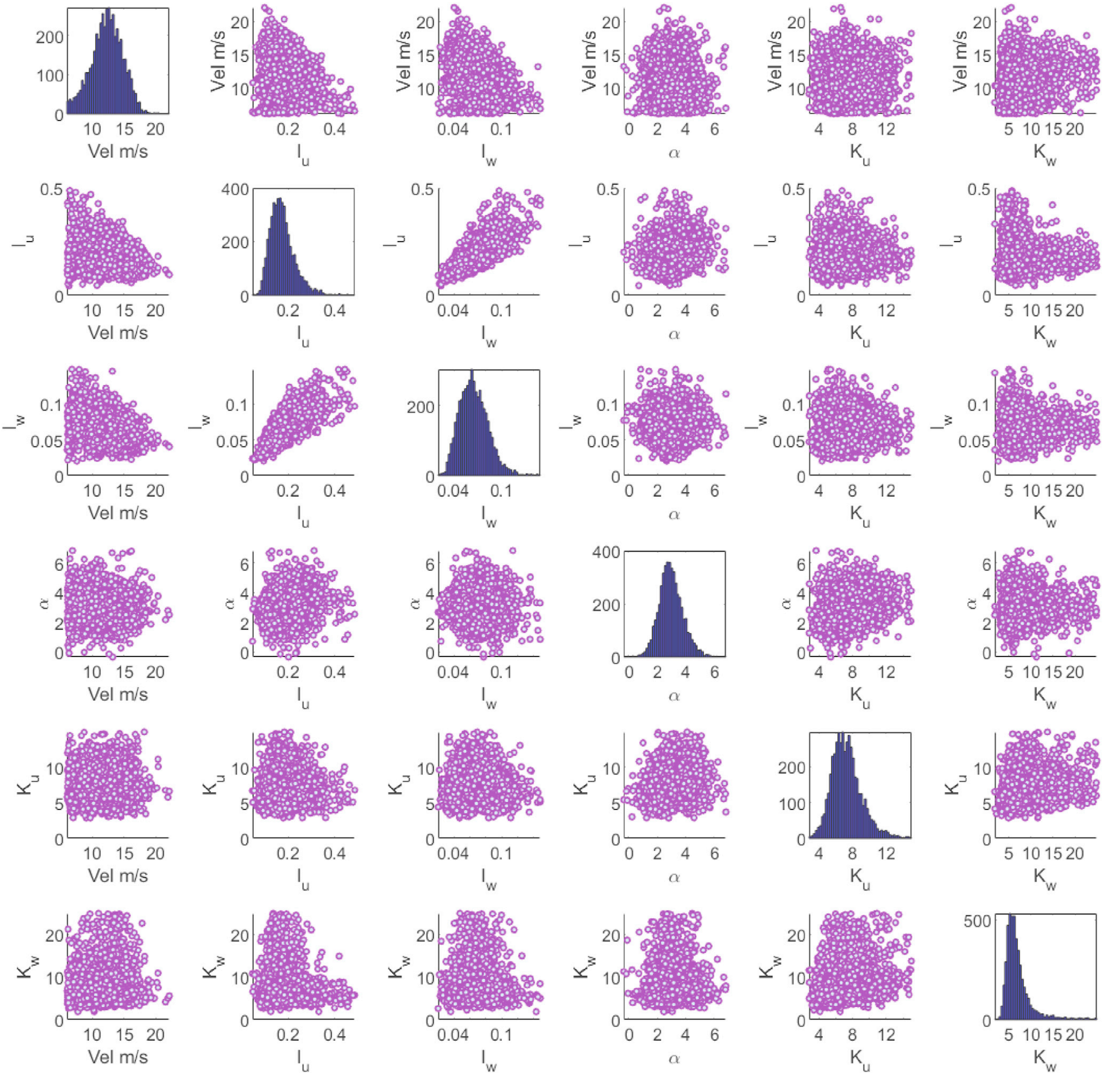

Fig. 12. Matrix plot of the histogram and correlations from the A6 midspan anemometer for the easterly winds dataset.

modeled as a Kaimal-type spectrum (Kaimal et al., 1972) Equation (33), while the normalized co-spectrum is modeled as a Davenport-type (Davenport A. G., 1961) (Equation (34)).

$$\frac{S_n f}{(V\,I_n)^2}=\frac{A_n f_z}{(1+1.5A_n f_z)^{5/3}},\ f_z=\frac{zf}{V},\ I_n=\frac{\sigma_n}{V} \tag{33}$$

$$Coh_{nm}(\Delta\chi,\omega)=exp\left(-K_n\frac{\Delta\chi f}{V}\right) \tag{34}$$

where the subscripts $n,m\in\{u,w\}$ indicate the along-wind and vertical turbulence components, z is the reference height, f is the frequency and A_n is the set of spectral peak parameters. For the Hardanger Bridge, (Fenerci, 2018) determined that an $A_u$of 30, an A_w of 3 and a z of 60 m are acceptable spectral quantities. I_n represents the turbulence intensities. Furthermore, the cross-coherence and cross-spectral terms associated with Coh_{nm} and S_{nm} when $n\neq m$ are ignored, and thus, only the spatial coherence was considered.

3.2. Synthetic datasets

The corresponding target output (Y) was chosen as the RMS of the lateral, vertical and torsional response components (σ_y, σ_z, σ_θ). Thus, a sample point i in the dataset i represented by the pair X_i, Y_i, as shown in Equation (35).

$$X_i=[V\ \sigma_u\ \sigma_w\ K_u\ K_w]_i \text{ and } Y_i=\left[\sigma_y\ \sigma_z\ \sigma_\theta\right]_i \tag{35}$$

To create the synthetic data using analytical predictions, two training datasets and one testing dataset were created. Each input sample $X_i$contains the wind features applied homogenously to all the wind elements. Furthermore, two different strategies were implemented to simulate the input.

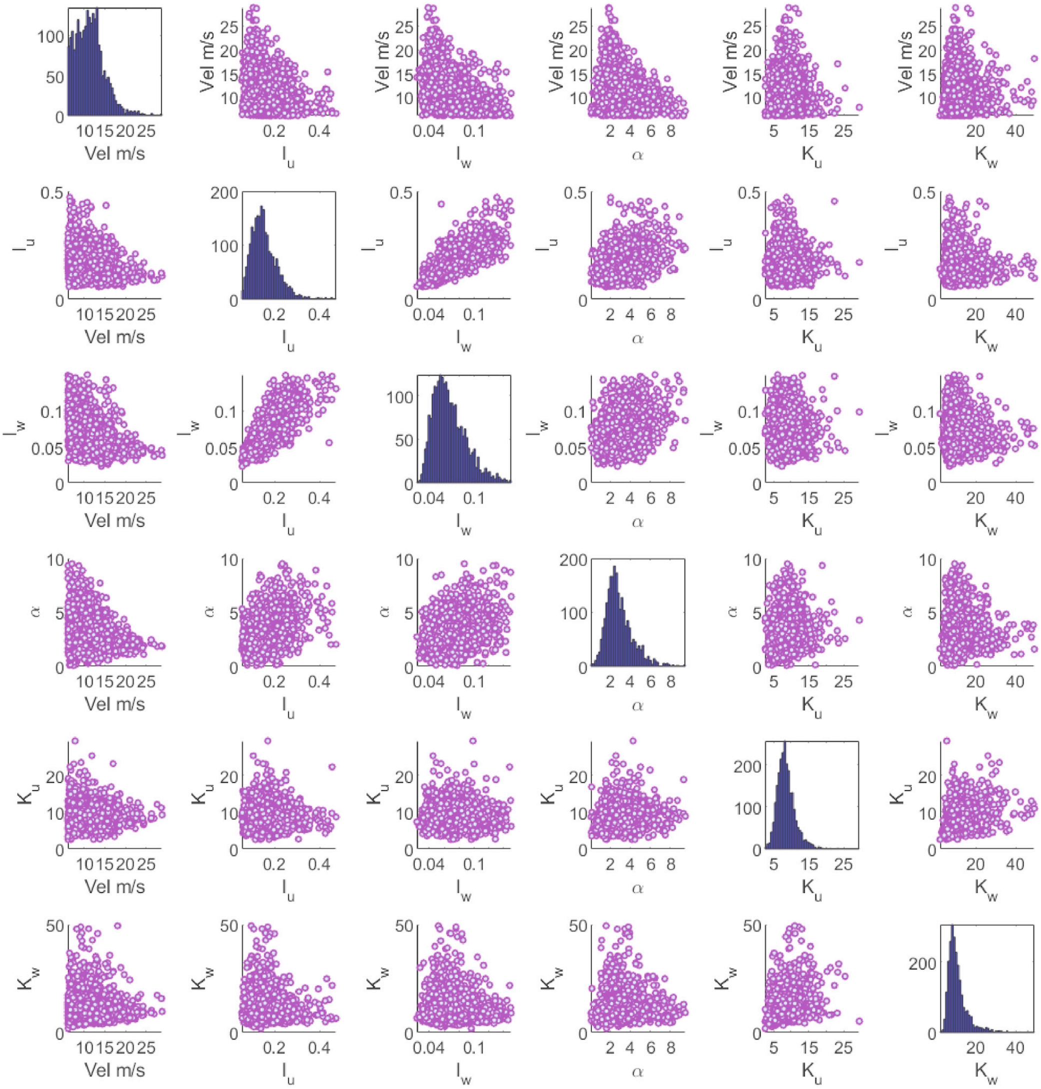

Fig. 13. Matrix plot of histogram and correlations from the A6 midspan anemometer for the westerly winds dataset.

The first strategy is to use a uniform grid of the wind parameters to ensure complete coverage inside the range of the full-scale measurements. Therefore, from the dataset collected by (Fenerci and Øiseth, 2018), the maximum and minimum values bounding each of the wind model parameters were extracted. The resulting discretization range and number of intervals for each variable are reported in Table 1, and with the reported discretization, 25,000 sample points were simulated.

The input from the uniform grid dataset from Table 1 covers the parameter space in a regular manner, which is not the case in the full-scale measurements, where the data are concentrated in certain regions of the parameter space. Therefore, to mimic the real dataset and to investigate how the machine learning algorithms handle such clustering of data points, a second input dataset is generated. This set was created using the extension of the standard Latin hypercube sampling approach (McKay et al., 1979) to correlated variables, correlated Latin hypercube sampling (CLHS) (Olsson et al., 2003). The average size of the directional training datasets to be introduced in the following section is 3500 samples. Therefore, for this dataset, the same number of samples was generated using the CLHS approach following the probability distribution functions and correlation coefficients from the full-scale measurements reported by (Fenerci and Øiseth, 2018).

Finally, following the CLHS generation scheme, a third dataset was generated to test the models. This set allows the validation of the models' generalization ability by examining their performance for the same task. Five hundred samples were generated for this dataset. A summary of the synthetic datasets features is reported in Table 2.

3.2.1. *Analytical prediction of the dynamic response of the Hardanger Bridge*

A schematic technical drawing of the Hardanger bridge's cross section is as shown in Fig. 4. Additionally, the eigenvalue analysis was performed to obtain the still-air modes using a finite element model of the Hardanger Bridge supplied by the Norwegian Public Roads

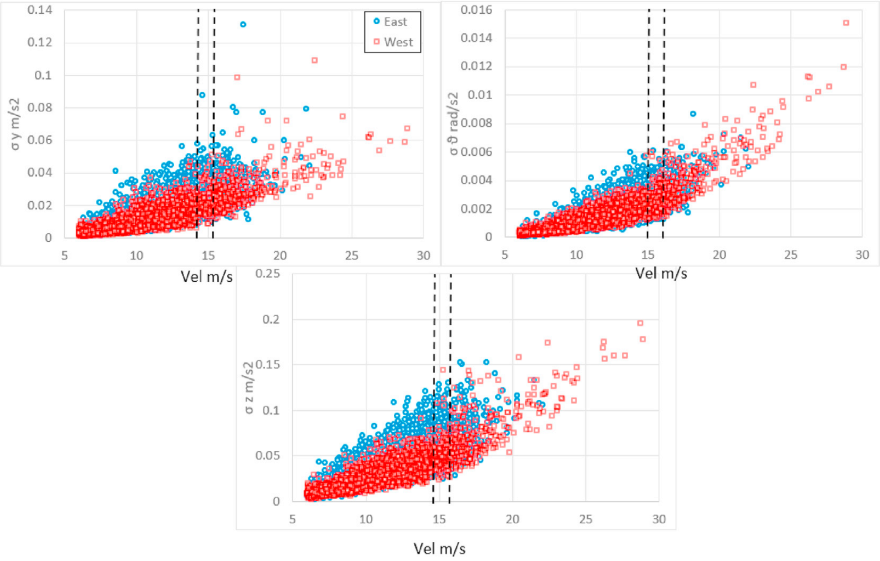

Fig. 14. Training datasets.

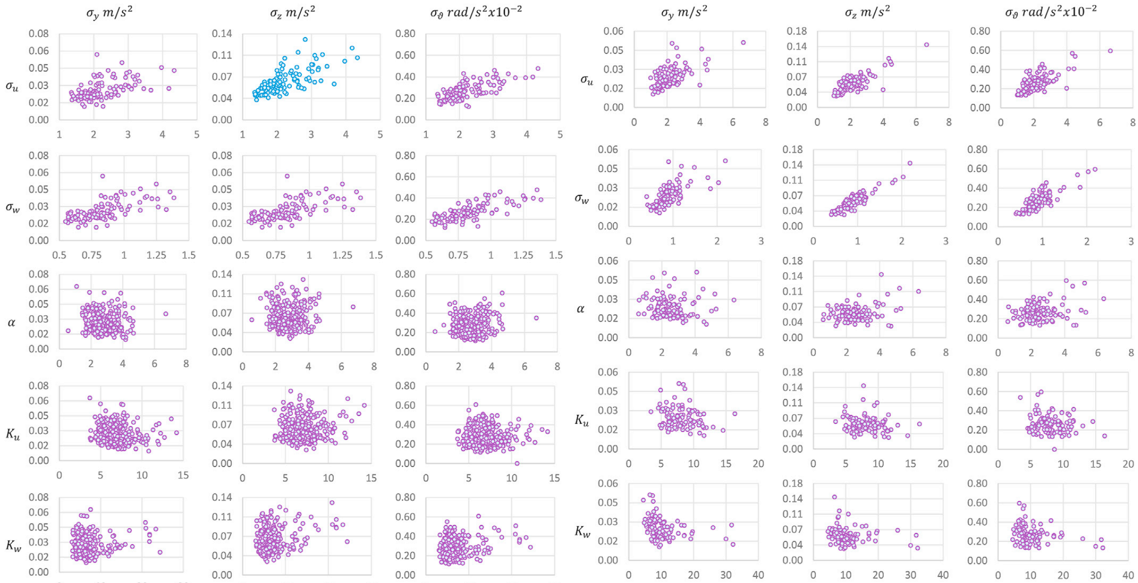

(a) Easterly winds

(b) Westerly winds

Fig. 15. Training dataset from 15 to 16 m/s a) easterly b) westerly winds.

Administration reported in (Fenerci et al., 2017). Both the girder and cable modal displacements were extracted for this analysis. The first 100 modes were considered in the analysis. The natural frequencies of the first 15 modes are reported in Table 3, the reader is referred to (Fenerci et al., 2017) (Lystad et al., 2020) (Petersen et al., 2017) further details of the bridge's modal behavior. Structural damping was modeled with the Rayleigh damping approach (Chopra, 2000) using the parameters $\alpha_r =$ 0.0009 and $\beta_r =$ 0.01102. Furthermore, the effective width B and height D of the Hardanger Bridge section are 18.3 and 3.2 m, respectively.

The load coefficients used in the analysis were those reported by (Fenerci and Øiseth, 2018) from wind tunnel testing set up of (Siedziako et al., 2017) and are shown in Table 4. The test was performed with Reynolds number of 2.01x10^5. The scaled cross section of the model was equipped with handrails and the pedestrian path was located upstream.

Additionally (Siedziako et al., 2017), reported the aerodynamic

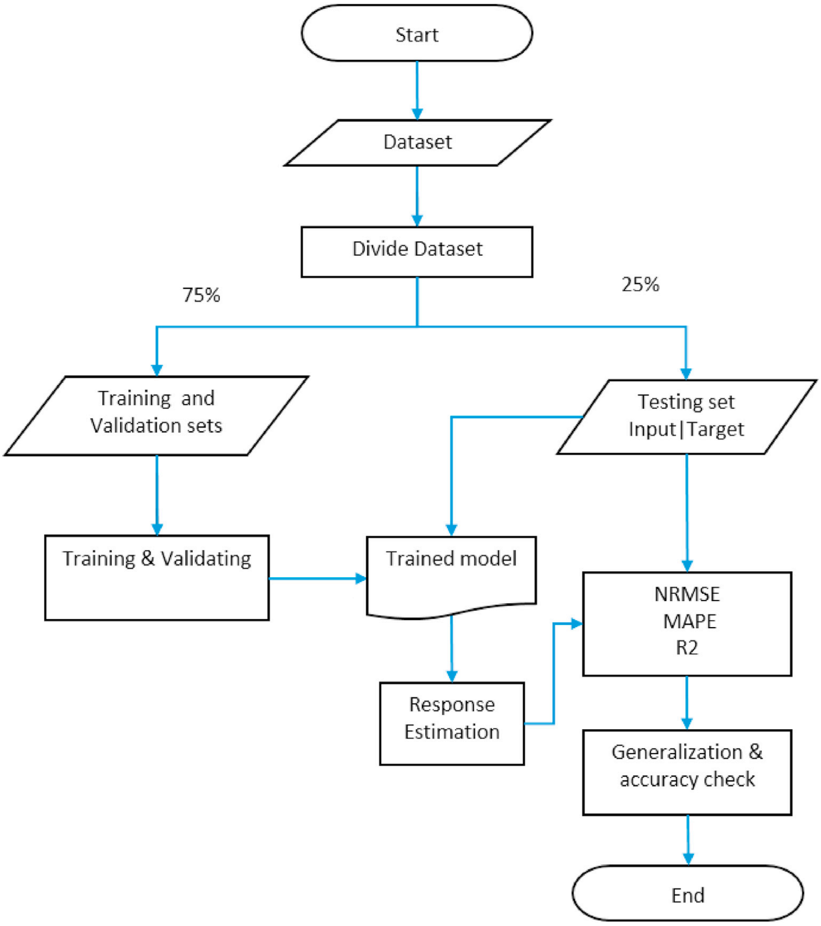

Fig. 16. Flowchart of the model training and comparison steps.

Table 5
ANN settings.

Setting	MLP
Activation function	Rectified linear unit
Cost function	Mean squared error
Optimization	Bayesian-adaptative moment
Number of hidden layers	2
Sizes	8–8
Batch size	10% of the dataset
Learning rate	Min = 1E-7
Number of epochs	1000

Table 6
Grid settings for the SVR hyperparameters.

Setting	Minimum	Maximum	Number of Intervals
Box constraint	1E-5	100	10E14
ε	$1e^{-4}\overline{\varepsilon}$	$1e^{2}\overline{\varepsilon}$	10E14
Polynomial degree	3	6	3

derivatives of the bridge cross section from the wind tunnel test. Fig. 5 and Fig. 6 show the experimental results of the 18 aerodynamic derivatives fitted a polynomial function that tends constant values outside the experimental data range. In the figures the reduced frequency $K = \frac{\omega B}{V}$ is introduced in the notation to enhance the presentation of the aerodynamic derivatives. Nonetheless, for the purposes of the surrogate modelling with synthetic datasets the use of the quasi steady theory showed to be sufficient. Therefore, the aerodynamic derivatives formulation was used just for the full-scaled measurements.

Finally, using the three simulated wind inputs described in the previous section (two inputs are used for training, one input is used for testing), the dynamic response of the Hardanger Bridge, namely, the RMS of the lateral, vertical and torsional components, was obtained using multimodal buffeting theory. The scatter plots showing the resulting input-output relationships are shown in Figs. 7-9 for the training uniform, training CLHS and testing CLHS datasets, respectevely.

3.3. Full-scale measurement data from the Hardanger Bridge

3.3.1. Overview of the measurements

The buffeting responses of the Hardanger Bridge were measured with an extensive measurement system composed of 9 ultrasonic anemometers that measure the wind speed in the range from 0 to 65 m/s with a 0.001 m/s resolution at a 32 Hz sampling frequency and 20 triaxial accelerographs that measure accelerations on the interval of ±4g at a

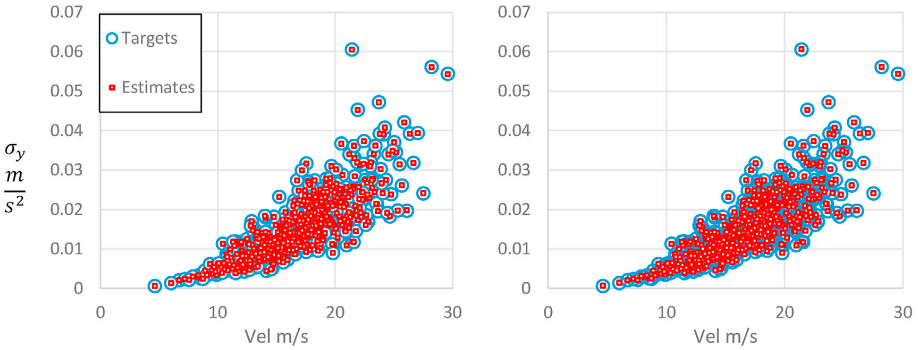

a) SVR σ_y

b) MLP σ_y

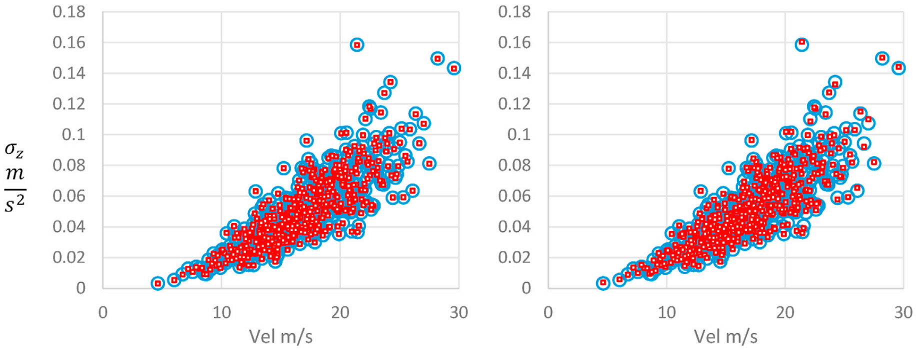

c) SVR σ_z

d) MLP σ_z

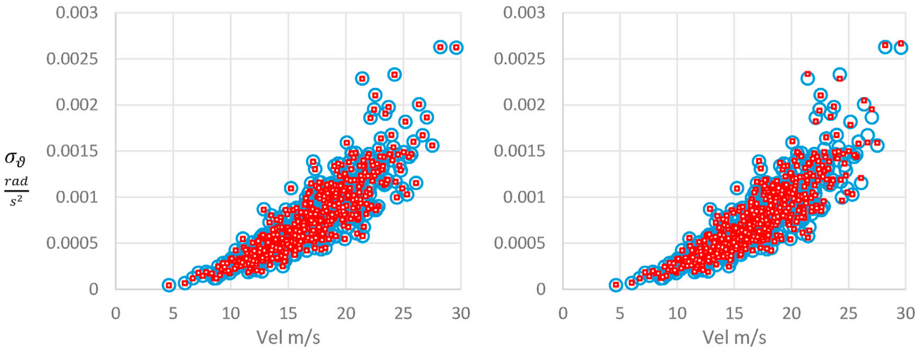

e) SVR σ_ϑ

f) MLP σ_ϑ

Fig. 17. Response panel plot for models trained with a uniform grid dataset for the (a) SVR σ_y (b) MLP σ_y (c) SVR σ_z (d) MLP σ_z (e) SVR σ_ϑ (f) MLP $\sigma_\vartheta$models.

200 Hz sampling frequency. More details on the Hardanger Bridge measurement system and dataset management procedure are given in (Fenerci, 2018), the dataset is available in open access (https://doi.org/10.21400/5ng8980s) (Fenerci et al., 2018). The installed anemometers record the incoming wind velocity in polar coordinates, while the coupled arrangement of the accelerometers register the triaxial bridge response (Fenerci et al., 2017).

3.3.2. Wind field modeling and turbulence parameters

The wind parameters were extracted from the measurement system at the A6 anemometer location (Fig. 10). Previous research campaigns at the site (Fenerci and Øiseth, 2018) (Fenerci et al., 2017) (Lystad et al., 2018) reported two data clusters in the mean wind direction histogram (Fig. 11). This phenomenon poses a challenge to the analysis due to the topography-related difference between the wind features depending on the incoming wind direction (Fenerci et al., 2017). Thus, in a similar manner as the previous campaigns, the WIVs from both clusters were studied separately.

Fig. 12 and Fig. 13 show the wind parameter matrix plots for the easterly and westerly wind datasets; the subfigures on the diagonal contain each input variable histogram, and the figures on the off-diagonal show the scatter plots between the parameters. Furthermore, the angle of attack, α, is introduced as an input parameter for this case, unlike the synthetic data.

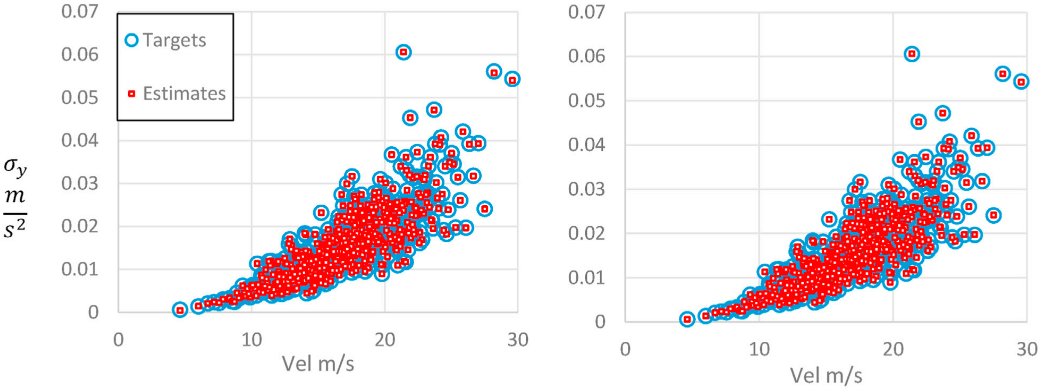

a) SVR σ_y

b) MLP σ_y

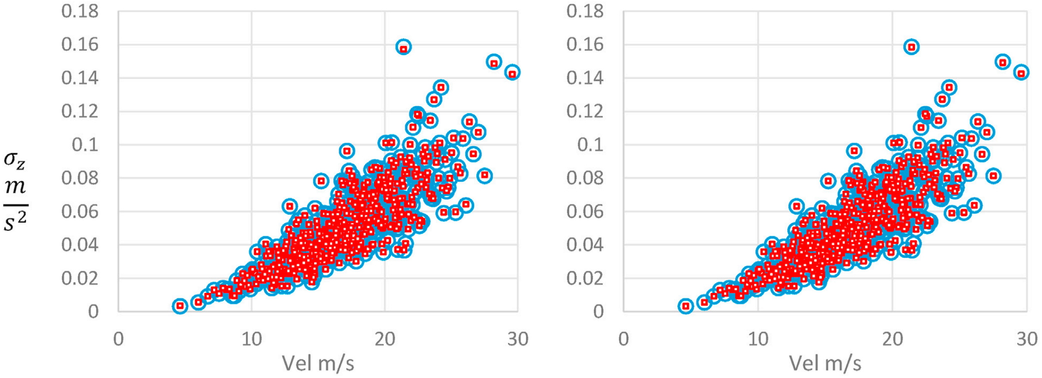

c) SVR σ_z

d) MLP σ_z

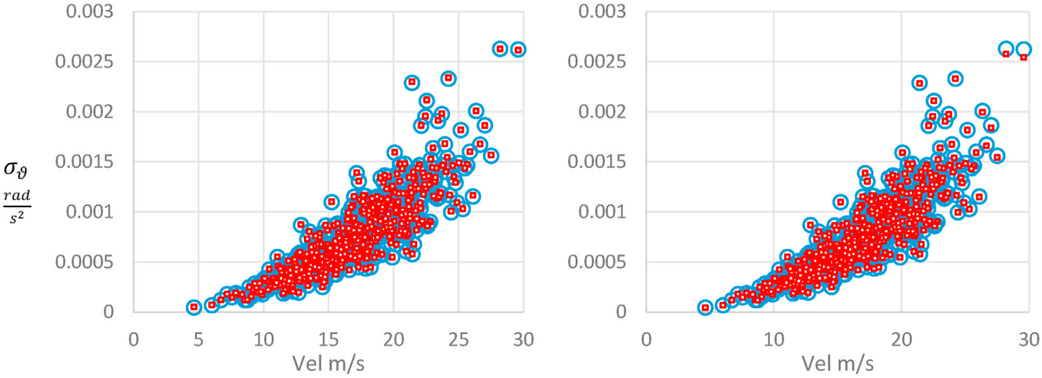

e) SVR σ_ϑ

f) MLP σ_ϑ

Fig. 18. Response scatter plot comparison for the models trained with the CLHS dataset for the (a) SVR $\boldsymbol{\sigma_y}$ (b) MLP $\boldsymbol{\sigma_y}$ (c) SVR $\boldsymbol{\sigma_z}$ (d) MLP $\boldsymbol{\sigma_z}$ (e) SVR $\boldsymbol{\sigma_\vartheta}$ (f) MLP $\boldsymbol{\sigma_\vartheta}$models.

3.3.3. Root mean square (RMS) of the responses at the midspan

The response of the Hardanger Bridge was measured at the same location as the wind input using the accelerometer coupled sensors H5 shown in Fig. 10. The lateral and vertical components of the acceleration were obtained as the average from the sensors at both sides of the girder, while the torsional component was computed by dividing the difference between the two vertical signals by their distance (13 m). Fig. 14 shows the panel plots of the training datasets for the westerly and easterly winds. These plots contain the structural responses at the midspan of Hardanger Bridge from the accelerometer coupled sensors H5 as described in (Fenerci et al., 2017). The figures show quadratic trends between the velocities and the responses, as expected. Fig. 15, on the

Table 7

Comparison of the evaluation metrics on the simulated datasets.

Model		NRMSE			MAPE			R2		
		σ_y	σ_z	σ_ϑ	σ_y	σ_z	σ_ϑ	σ_y	σ_z	σ_ϑ
Uniform grid	MLP	1.02E-03	5.87E-03	7.21E-03	0.4751	1.7468	1.936	1.00	0.99	0.99
Uniform grid	SVR	5.14E-04	1.66E-03	7.70E-04	0.1853	0.5748	0.303	1.00	1.00	1.00
Random CLHS	MLP	1.46E-04	3.51E-04	1.76E-03	0.0092	0.0120	0.036	1.00	1.00	1.00
Random CLHS	SVR	4.97E-04	8.90E-04	6.62E-04	0.1465	0.1233	0.115	1.00	1.00	1.00

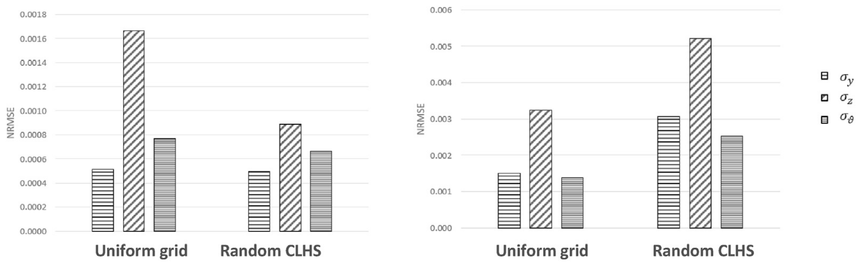

(a) NRMSEs for the different SVR models

(b) NRMSEs for the different SVR models (outliers only)

Fig. 19. (a) NRMSEs for the different SVR models (b) NRMSEs for the different SVR models (outliers only).

other hand, shows the variation in the structural responses as a function of the complementary wind input parameters for the velocity range from 15 to 16 m/s of the a) easterly and b) westerly winds. This figure shows linear trends between the responses and the turbulence intensities, and no apparent trend can be observed for the other parameters.

4. Training, validation and testing datasets

The training datasets correspond to the division of the data that will be fed into the machine learning models; for this type of application, it is deemed appropriate to take 65% of the dataset for training. Furthermore, 10% of the dataset was used as a validation dataset for tuning the model hyperparameters and optimizing the global performance. Thus, an additional 25% remained for the testing data. The schematic flowchart of the analysis is shown in Fig. 16.

4.1. Model hyperparameters and settings

In ANN models, the network architecture, function selection and optimization scheme affect the results. Thus, Equation (5) minimizes the loss function for a given network setting. With the aim of avoiding overtraining, the MLP model was trained using the batch training strategy; i.e., every optimization cycle was performed on a different division of the dataset. The configuration found to be appropriate for training the MLP models is reported in Table 5.

Analogously, for the SVR model, Equation (12) will give rise to different estimation functions if changes are made to the kernel function, box constraint C, and slack parameters ξ, among other settings. For this application, experience suggests the use of a polynomial function as the kernel function, as given in Equation (36), and half the width of the ε-insensitive band, $\bar{\varepsilon}$, is computed by Equation (37). Then, a built-in grid search optimization algorithm is used to find the configuration that minimizes the loss functions with the grid setting reported in Table 6. Further studies on hyperparameter optimization for buffeting response modeling are beyond the scope of this paper but may be the objective of future research.

$$K(x_i{'}x) = \left(1 + x_i{'}x_j\right)^d \tag{36}$$

$$\bar{\varepsilon} = \frac{interquartile\ \{range(\mathbf{y})\}}{13.49} \tag{37}$$

5. Performance assessment and comparison

5.1. Performance metrics

Three metrics were used to compare the estimates and targets: the normalized root mean square error (NRMSE, Equation (38)) (Amstrong and Collopy, 1992), the mean absolute percent error (MAPE, Equation (39)) and the coefficient of determination (R2, Equation (40)). The NRMSE (Amstrong and Collopy, 1992) becomes representative of the modeling since it is the normalized version of the square root of the mean squared error (MSE), which is used as the loss function for the MLP. On the other hand, the MAPE results are more intuitive since they present the deviation as a percent. Finally, R2 allows the weight of the deviation of the estimates according to their variance.

$$NRMSE = \sqrt{\frac{1}{N}\sum_{j=1}^{N}\left(\widehat{y}_j - y_j\right)^2} \Big/ \{max(Y) - \min(Y)\} \tag{38}$$

$$MAPE = \frac{1}{N}\sum_{j=1}^{N}\frac{\left|\widehat{y}_j - y_j\right|}{y_j} \tag{39}$$

$$R2 = 1 - \sum_{j=1}^{N}\left(\widehat{y}_j - y_j\right)^2 \Big/ \left(y_j - \overline{y}\right)^2 \tag{40}$$

5.2. Synthetic data

5.2.1. Uniform grid training dataset

The panels in Fig. 17 show the comparison between the targets from the testing dataset and estimates for the machine learning models trained with the linearly spaced dataset for the SVR response models and for the MLP. In the figure, the X-axis is the velocity, and the Y-axis is the RMS of the response component. The figures show a complete matching of the estimation and target over the entire wind speed range. The satisfactory

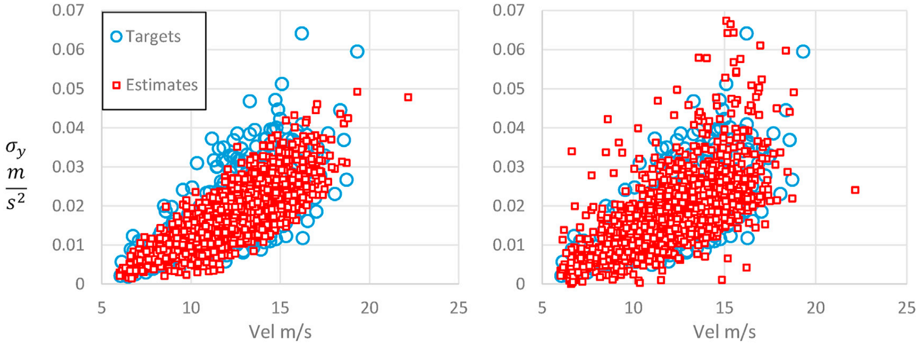

a) Easterly winds σ_y b) Westerly winds σ_y

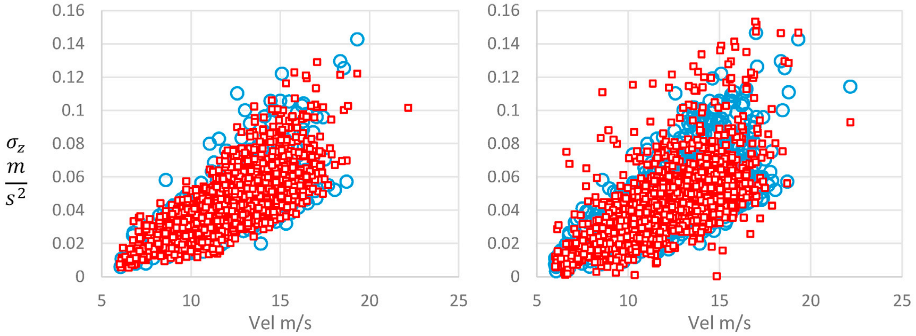

c) Easterly winds σ_z d) Westerly winds σ_z

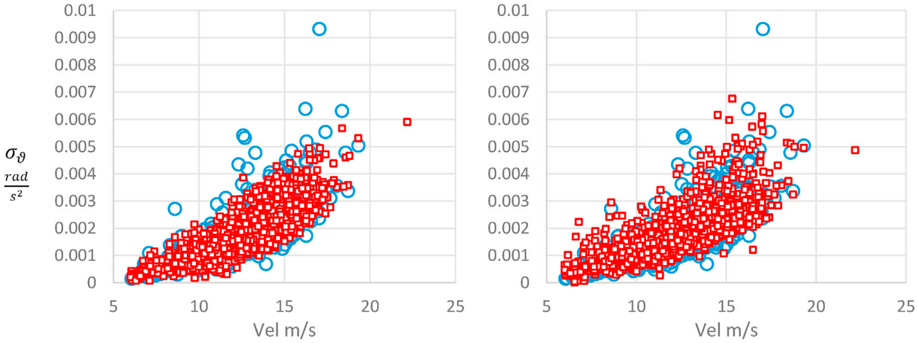

e) Easterly winds σ_ϑ f) Westerly winds σ_ϑ

Fig. 20. Response comparisons SVR models (a) Easterly σ_y (b) Westerly σ_y (c) Easterly σ_z (d) Westerly σ_z (e) Easterly σ_ϑ (f) Westerly.σ_ϑ

performance of the machine learning models on the simulated dataset shows the effectiveness of the method in modeling the buffeting phenomenon and encourages its application to the full-scale data.

5.2.2. *Random training dataset*

Analogously, the comparison of the scatter plots between the randomly generated dataset target from the testing dataset and its corresponding machine learning estimates is shown in Fig. 18. Despite the clustering of the data points around the moderate wind speeds, the algorithm is successful in predicting the response in the entire wind speed range.

Table 7 extends the graphical overview and reports the evaluation metrics of the three response components (i.e., σ_y, σ_z and σ_ϑ) for the two machine learning models (i.e., the MLP and SVR models) on the two different datasets (i.e., the uniform grid and random CLHS datasets). With the given evaluation metrics, the SVR models perform better than MLP models in the uniform grid dataset, whereas the opposite occurs in the random CLHS dataset. Nevertheless, the order of magnitude of the NRMSE is approximately 10E-4, stating an appreciably good general performance level, with the lowest error of 1.46E-04 for the MLP/CLHS/σ_y response and the highest of 7.21E-03 in MLP/uniform grid/σ_ϑ. Moreover, the highest and lowest MAPE values of 1.936% and 0.0092% agree with the NRMSE results.

Estimation of extreme responses is especially important for long-span

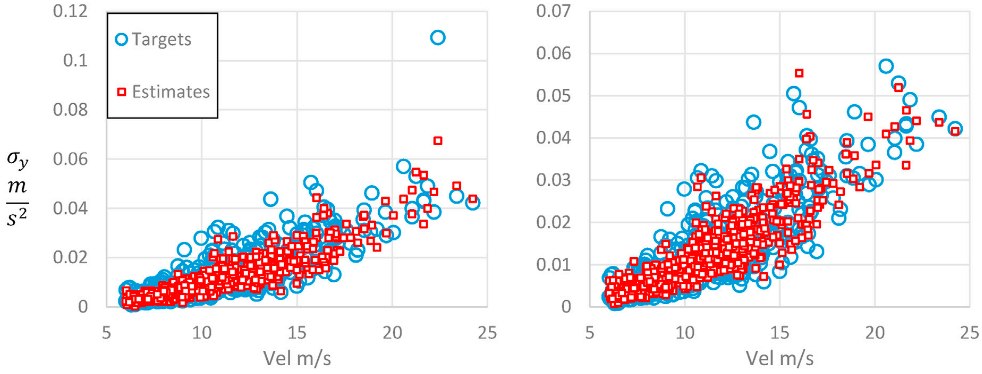

a) Easterly winds σ_y

b) Westerly winds σ_y

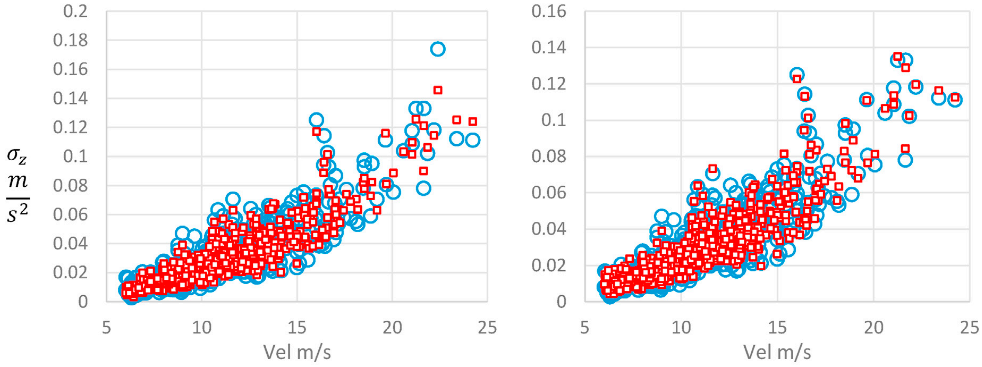

c) Easterly winds σ_z

d) Westerly winds σ_z

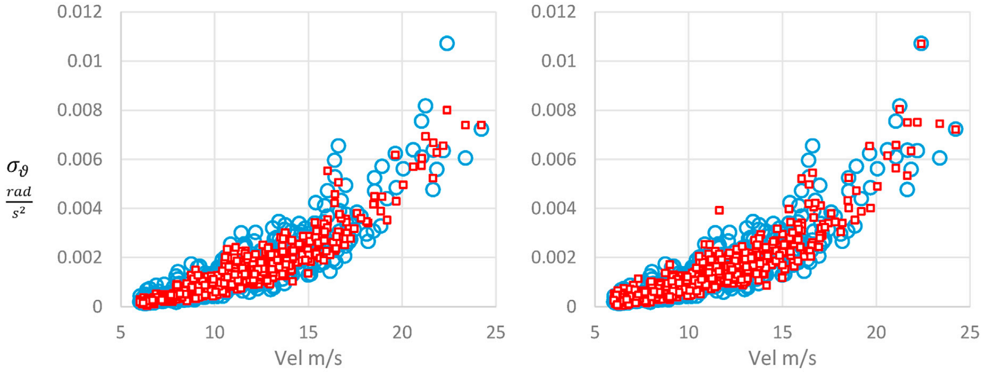

e) Easterly winds σ_ϑ

f) Westerly winds σ_ϑ

Fig. 21. Response comparisons MLP models (a) Easterly $\boldsymbol{\sigma_y}$ (b) Westerly $\boldsymbol{\sigma_y}$ (c) Easterly $\boldsymbol{\sigma_z}$ (d) Westerly $\boldsymbol{\sigma_z}$ (e) Easterly $\boldsymbol{\sigma_\vartheta}$ (f) Westerly.$\boldsymbol{\sigma_\vartheta}$

bridge buffeting response modeling. Thus, a comparison limited to the maximum values given by $\sigma_y > 0.3$, $\sigma_z > 0.1$ and $\sigma_\vartheta > 0.018$ is presented. To highlight the difference in the performance, Fig. 19 (a) reports the NRMSE of the SVR models in the general case and (b) reports the maximum values. Overall, the models trained with the random CLHS dataset showed less error compared to their uniform grid counterparts. However, for the outliers, the uniform grid models performed better because the CLHS dataset concentrates the data points in the central region, leaving fewer data points in the maximum value region, resulting in better predictions for moderate wind speeds and compromising the accuracy of the extreme values. On the other hand, the uniform grid dataset presents a better accuracy in the region of the outliers. It should be noted that both methods provide reasonably accurate results.

Table 8
Evaluation metrics for the directional models on real datasets.

Model	NRMSE			MAPE			R2		
	σ_y	σ_z	σ_ϑ	σ_y	σ_z	σ_ϑ	σ_y	σ_z	σ_ϑ
West MLP	6.87E-02	5.39E-02	3.79E-02	26.8	10.7	19.5	0.89	0.95	0.92
West SVR	5.14E-02	3.06E-02	3.28E-02	21.6	14.1	22.2	0.84	0.94	0.92
East MLP	8.87E-02	1.06E-01	5.74E-02	42.0	36.4	29.1	0.44	0.59	0.72
East SVR	5.98E-02	5.65E-02	4.87E-02	22.9	13.9	19.4	0.69	0.84	0.80

Table 9
Constant input values for the directional model comparisons.

Wind feature	Symbol	Constant value
Along-turbulence SD	σ_u	0.1*V
Vertical turbulence SD	σ_w	0.06*V
Angle of attack	α	2.9
Along-wind decay coefficient	K_u	8.6
Vertical decay coefficient	K_w	10.7

5.3. Full-scale measurement data

The techniques verified with the synthetic data case were extended to full-scale measurements. For this aim, the scatter plots the response comparisons from the different models are shown in Figs. 20 and 21. Additionally, Table 8 shows the evaluation of the three response components (σ_y, σ_z and σ_ϑ) for the two machine learning models (MLP and SVR) in the two different datasets (westerly and easterly winds).

The easterly and westerly wind model estimates were compared. The input was varying mean wind speeds, with linearly dependent $\sigma_{u,}\sigma_w$ (to retain the observed trend in the real data), and the other parameters were held constant. Table 9 reports the input parameter settings. Fig. 22 shows the plots comparing the predictions of both directional models for the three response components σ_y, σ_z and σ_ϑ from the SVR algorithm, while Fig. 23 reports a similar comparison for the MLP model.

Both figures show that the model trained with the easterly wind dataset yields a higher response estimation for the same input conditions. This is consistent with the behavior observed in the full-scale measurements reported in Fig. 14.

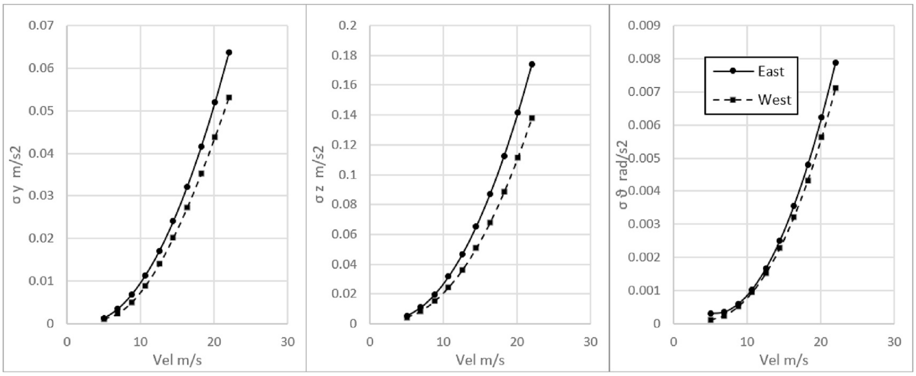

(a) (b) (c)

Fig. 22. Prediction comparison for the directional SVR models on common input: (a) σ_y, (b) σ_z and (c).σ_ϑ

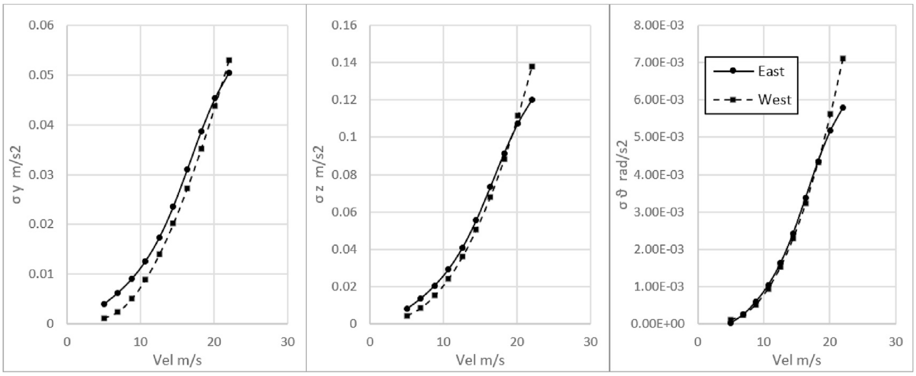

(a) (b) (c)

Fig. 23. Prediction comparison for the directional MLP models on common input: (a) σ_y, (b) σ_z and (c).σ_ϑ

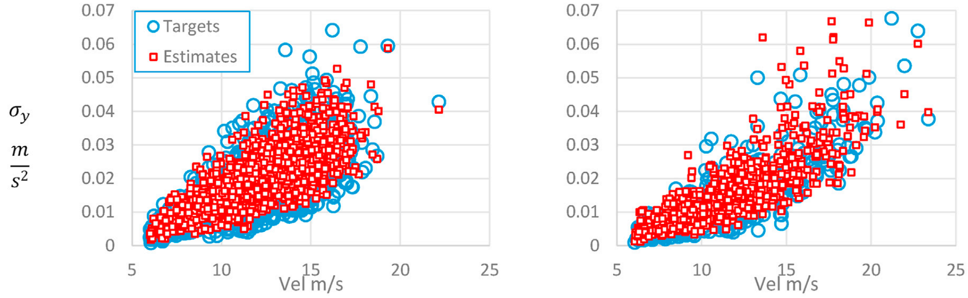

a) Easterly winds σ_y		b) Westerly winds σ_y

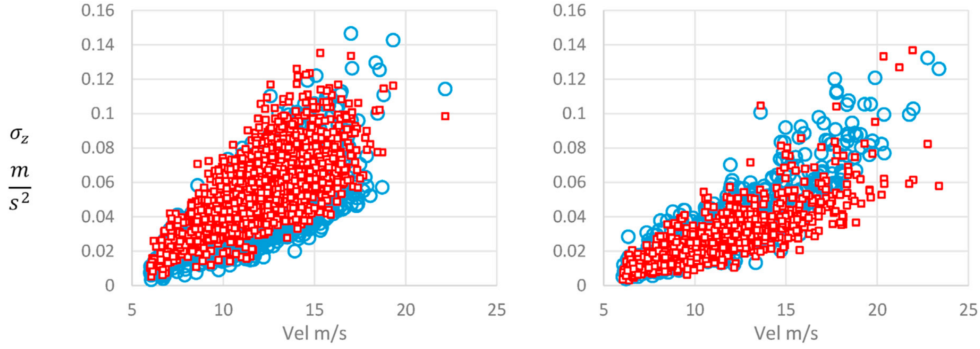

c) Easterly winds σ_z		d) Westerly winds σ_z

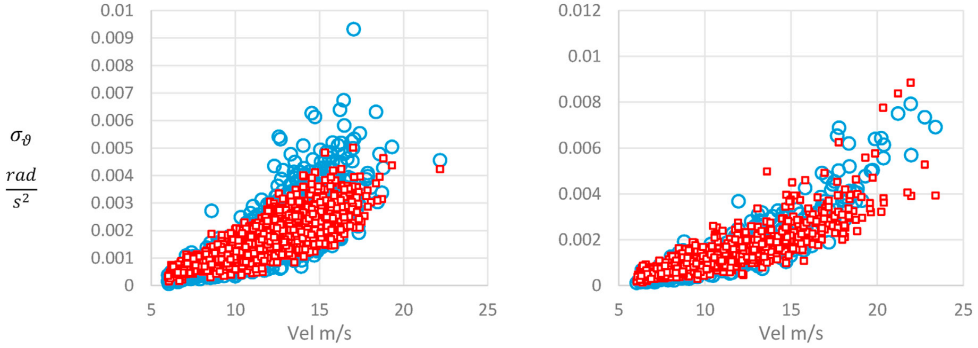

e) Easterly winds σ_ϑ		f) Westerly winds σ_ϑ

Fig. 24. Response comparison computed with buffeting theory (a) Easterly $\boldsymbol{\sigma_y}$ (b) Westerly $\boldsymbol{\sigma_y}$ (c) Easterly $\boldsymbol{\sigma_z}$ (d) Westerly $\boldsymbol{\sigma_z}$ (e) Easterly $\boldsymbol{\sigma_\vartheta}$ (f) Westerly.$\boldsymbol{\sigma_\vartheta}$

Table 10
Evaluation metrics for the estimates from buffeting theory.

Model	NRMSE			MAPE			R2		
	σ_y	σ_z	σ_ϑ	σ_y	σ_z	σ_ϑ	σ_y	σ_z	σ_ϑ
West BFT	7.65E-02	6.27E-02	5.47E-02	38.68	19.13	34.17	0.82	0.85	0.83
East BFT	7.62E-02	1.12E-01	5.97E-02	33.58	35.41	24.81	0.54	0.73	0.72

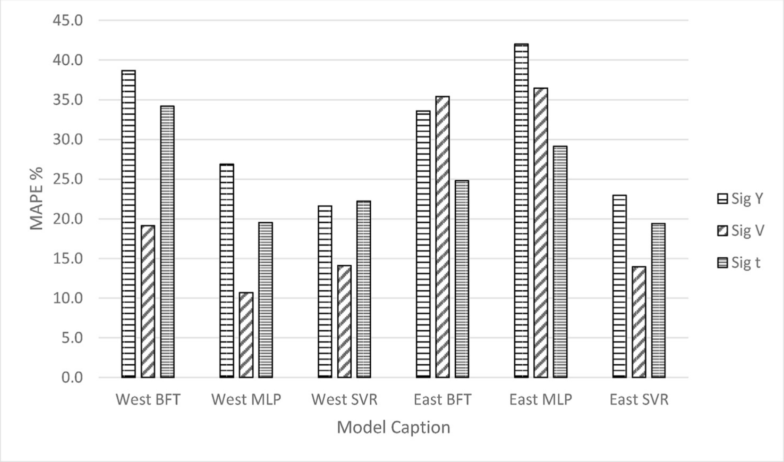

Fig. 25. MAPEs computed with buffeting theory and machine learning.

5.4. *Machine learning vs. buffeting theory*

Finally, the response of the Hardanger Bridge was estimated analytically using buffeting theory and the wind input from the full-scale measurements. The response comparison between the measured response and the buffeting theory estimation is shown in Fig. 24, and the corresponding evaluation metrics are reported in Table 10. A graphical comparison in terms of the MAPE between the estimates obtained with machine learning reported in Table 8 and the estimates obtained with buffeting theory is shown in Fig. 25.

The SVR estimates yield more accurate results than the MLP and buffeting theory on both directional datasets. Moreover, for the westerly winds dataset, both machine learning models predicted more accurate estimate than buffeting theory. Using the MAPE, the greater difference between buffeting theory and the SVR model was 17% for σ_y and the lowest difference was approximately 5% for σ_z on the easterly winds' dataset. In general, the estimates of the full-scale observations show a slight decrease in the performance compared with the ideal case, mainly because uncertainties in the dynamic behavior, such as the inhomogeneities and non-stationarity of the wind field, traffic and temperature effects are not completely captured by analytical models.

A difference in the error metrics between easterly and westerly wind related responses is exposed for both cases, estimations with machine learning (Table 8) and buffeting theory estimation (Table 10). For example, R2 metrics for the σ_y responses in Table 8 vary from 0.44 (easterly) to 0.89 (westerly) for MLP and 0.69 (easterly) to 0.84 (westerly) for SVR whereas Table 10 shows a variation from 0.54 (easterly) to 0.82 (westerly) for the same response component. The main reason for this behavior is that the aerodynamic properties of the bridge, namely the steady-state force coefficients (Table 4) and the aerodynamic derivatives (Figs. 5–6) were obtained for the case of winds approaching from the west, which are the strongest. This partly explains the poor performance of the analytical predictions for the easterly winds. Further, the easterly winds are more affected by the more complex topography, which typically causes higher angles of attack. Such issues are handled implicitly by the machine learning models, where the buffeting theory is more challenging.

6. Conclusion

In this paper, accurate buffeting response estimations were computed from analytical and machine learning models. The wind input dataset was obtained from full-scale measurements and simulated data following the probabilistic model of the observed wind turbulence field. Then, the quality of the estimates was evaluated, leading to the following conclusions:

- Estimations from machine learning models (i.e., the SVR and MLP models) on the synthetic datasets were reasonably accurate. Therefore, the good quality of the estimates makes the technique suitable for surrogate model development such as those required in reliability analyses.
- The models trained with the full-scale datasets were less accurate than the models trained with the synthetic datasets. The main reasons for this are the various uncertainties in the dynamic behavior that are not captured by the monitoring system, such as the inhomogeneities and non-stationarity of the wind field, traffic and temperature effects. However, as data-driven models bypass some of the limitations of buffeting theory, machine learning-based estimates were more accurate than the analytical predictions.
- Considering the slightly different behavior observed under easterly and westerly winds, two different machine learning models were trained for the two directions. The models trained on the easterly winds predicted higher responses under the same wind input, capturing the observed behavior.
- The SVR model yielded better response predictions than the MLP model on both the simulated and full-scale measurements. Furthermore, the method was more accurate that the analytical response estimates with the multimodal approach.

CRediT authorship contribution statement

Dario Fernandez Castellon: Writing - original draft, Software, Methodology, Formal analysis. **Aksel Fenerci:** Writing - review & editing, Data curation, Investigation. **Ole Øiseth:** Conceptualization, Supervision, Project administration.

Declaration of competing interest

The authors declare that they have no known competing financial interests or personal relationships that could have appeared to influence the work reported in this paper.

Acknowledgements

The research presented in this paper was financially supported by the Norwegian Public Roads Administration (Statens Vegvesen) as a part of the E-39 coastal highway project.

References

Fenerci, A., Øiseth, O., 2018. Site-specific data-driven probabilistic wind field modelling for wind-induced response prediction of cable-supported bridges. J. Wind Eng. Ind. Aerod. 181, 161–179.

Alpaydin, E., 2020. Introduction to Machine Learning, fourth ed. Massachusetts Institute of Technology, Cambridge, Massachusetts.

Amstrong, J.S., Collopy, F., 1992. Error measures for generalizing about forecasting. Int. J. Forecast. 8 (1), 69–80.

Awad, M., Khanna, R., 2015. Support vector regression. In: Efficient Learning Machines. apress, Berkeley, CA.

Bernardini, E., Spence, S.M., Wei, D., Kareem, A., 2015. Aerodynamic shape optimization of civil structures: a CFD-enabled Kriging-based approach. J. Wind Eng. Ind. Aerod. 144, 154–164.

Bietry, J., Delaunay, D., Conti, E., 1995. Comparison of full-scale measurement and computation of wind effects on a cable-stayed bridge. J. Wind Eng. Ind. Aerod. 57 (2–3), 225–235.

Bishop, C.M., 1994. Neural Networks for Pattern Recognition. Oxford University Press, Inc, New York.

Bishop, C.M., 2006. Pattern Recognition and Machine Learning. Springer Science+ Business Media, LLC, New York.

Chen, X., Kareem, A., 2003. New frontiers in aerodynamic tailoring of longspan bridges: an advanced analysis framework. J. Wind Eng. Ind. Aerod. 91, 1511–1528.

Chen, X., Matsumoto, M., Kareem, A., 2000. Aerodynamic coupling effects ON flutter and buffeting OF bridges. J. Eng. Mech. ASCE 17–26.

Chen, C.H., Wu, J.C., Chen, J.H., 2008. Prediction of flutter derivatives by artificial neural networks. J. Wind Eng. Ind. Aerod. 96, 1925–1937.

Cheynet, E., Jakobsen, J.B., Snæbjörnsson, J., 2016. Buffeting response of a suspension bridge in complex terrain. Eng. Struct. 128, 474–487.

Chopra, A.K., 2000. Dynamics of Structures. Prentice Hall, Upper Saddl River.

Cid Montoya, M., Nieto, F., Hernández, S., Kusano, I., Álvarez, A., Jurado, J., 2018. CFD-based aeroelastic characterization of streamlined bridge deck cross-sections subject to shape modifications using surrogate models. J. Wind Eng. Ind. Aerod. 177, 405–428.

Davenport, A.G., 1961. The spectrum of horizontal gustiness near the ground in high winds. Q. J. R. Meteorol. Soc. 87 (372), 194–211.

Davenport, A., 1962. Buffeting of a suspension bridge by storm winds. J. Struct. Div. 88 (3), 233–270.

Diana, G., Bruni, S., Rocchi, D., 2005. A numerical and experimental investigation on aerodynamic non. In: EACWE4 —The Fourth European & African Conference on Wind Engineering. Prage: Institute of Theoretical and Applied Mechanics Academy of Sciences of the Czech Republic, Prague, pp. 86–87.

Diana, G., Resta, F., Rocchi, D., 2008. A new numerical approach to reproduce bridge aerodynamic non-linearities in time domain. J. Wind Eng. Ind. Aerod. 96 (10–11), 1871–1884.

Fang, C., Tang, H., Li, Y., Zhang, J., 2020. Stochastic response of a cable-stayed bridge under non-stationary winds. Ocean Eng. 199 (106967), 1–15.

Fenerci, A., 2018. Full-scale investigation of the effects of wind turbulence characteristics on dynamic behavior of longs-span bridges in complex terrain. Trondheim: Doctoral theses at NTNU 100, 2018.

Fenerci, A., Øiseth, O., 2017. Measured buffeting response of a long-span suspension bridge compared with numerical predictions based on design wind spectra. J. Struct. Eng. 143 (9), 1–15, 04017131.

Fenerci, A., Øiseth, O., 2018. Strong wind characteristics and dynamic response of a long-span suspension bridge during a storm. J. Wind Eng. Ind. Aerod. 170, 116–138.

Fenerci, A., Øiseth, O., Rønnquist, A., 2017. Long-term monitoring of wind field characteristics and dynamic response of a long-span suspension bridge in complex terrain. Eng. Struct. 147, 269–284.

Fenerci, A., Kvåle, K. A., Petersen, Ø. W., Rønnquist, A., & Øiseth, O. (2018, 08 18). Retrieved from: https://doi.org/10.1016/j.engstruct.2017.06.069.

Hu, L., Xu, Y.-L., Huang, W.-F., 2013. Typhoon-induced non-stationary buffeting response of long-span bridges in complex terrain. Eng. Struct. 57, 406–415.

Hu, L., Xu, Y.-L., Zhu, Q., Guo, A., 2017. Tropical storm–induced buffeting response of long-span bridges: enhanced nonstationary buffeting force model. J. Struct. Eng. 143 (6).

Jain, A., Jones, N.P., Scanlan, R.H., 1996. Coupled aeroelastic and aerodynamic response analysis of long-span bridges. J. Wind Eng. Ind. Aerod. 69–80.

James, G., Witten, D., Hastie, T., Tibshirani, R., 2013. An Introduction to Statistical Learning with Applications in R. Springer Science+Business Media, New York.

Kaimal, J.C., Wyngaard, J.C., Izumi, Y., Cote, O.R., 1972. Spectral characteristics of surface-layer turbulence. Quaterly J. Roy. Meteorol. Soc. 98 (417), 563–589.

Katsuchi, H., Akiyama, H., Scanlan, R., Jones, N.P., 1998. Multi-mode flutter and buffeting analysis of the Akashi-Kaikyo bridge. J. Wind Eng. Ind. Aerod. 431–441.

Kuhn, H., Tuker, A., 1951. Nonlinear programing. In: Proceedings of the Second Berkeley Symposium on Mathematical Statistics and Probability. Berkeley.

Le, V., Caracoglia, L., 2020. A neural network surrogate model for the performance assessment of a vertical structure subjected to non-stationary, tornadic wind loads. Comput. Struct. 231.

Li, S., Laima, S., Li, H., 2018. Data-driven modeling of vortex-induced vibration of a long-span suspension bridge using decision tree learning and support vector regression. J. Wind Eng. Ind. Aerod. 172, 196–211, 2018.

Lystad, T.M., Fenerci, A., Øiseth, O.A., 2018. Evaluation of mast measurements and wind tunnel terrain models to describe spatially variable wind field characteristics for long-span bridge design. J. Wind Eng. Ind. Aerod. Elsevier 179, 558–573.

Lystad, T.M., Fenerci, A., Øiseth, O.A., 2020. Buffeting response of long-span bridges considering uncertain turbulence parameters using the environmental contour method, 213. Engineering Structures.

Macdonald, J., 2003. Evaluation of buffeting predictions of a cable-stayed bridge from full-scale measurements. J. Wind Eng. Ind. Aerod. 91 (12–15), 1465–1483.

McKay, M.D., Beckman, R.J., Conover, W.J., 1979. A comparison of three methods for selecting values of input variables in the analysis of output from a computer code. American Statistical Association and American Society for Quality, pp. 239–245.

Nieto, F., Cid Montoya, M., Hernández, S., Kusano, I., Casteleiro, A., Álvarez, A.J., et al., 2020. Aerodynamic and aeroelastic responses of short gap twin-box decks: box geometry and gap distance dependent surrogate based design. J. Wind Eng. Ind. Aerod. *201*.

Olsson, A., Sandberg, G., Dahlblom, O., 2003. On Latin hypercube sampling for structural reliability analysis. Struct. Saf. 47–68.

Petersen, Ø.W., Øiseth, O., Lourens, E.-M., 2017. Estimation of the dynamic response of a slender suspension bridge using measured acceleration data. In: X International Conference Oon Structural Dynamics. EURODYN 2017. Rome.

Ripley, B.D., 1996. Pattern Recognition and Neural Networks. Cambridge University Press, Cambridge ,UK.

Rizzo, F., Caracoglia, L., 2020. Artificial Neural Network model to predict the flutter velocity of suspension bridges. Comput. Struct. 233.

Rosenblatt, F., 1958. The perceptron: a probabilisitc model for information storage and organization in the brain. Psychol. Rev. 65 (6), 386–408.

Rosenblatt, F., 1961. Principles of Neurodynamics: Perceptrons and the Theory of the Brain Mechanisms. Spartan Books, Washington.

Rumelhart, D.E., Hinton, G.E., Williams, R.J., 1986. Learning representations by back-propagating errors. Lett. Nat. 323 (9), 533–536.

Scanlan, R.H., Tomko, J.J., 1971. Air foil and bridge deck flutter derivatives. J. Soil Mech. Found Div. 97 (6), 1717–1739.

Siedziako, B., Øiseth, O., Rønnquist, A., 2017. An enhanced forced vibration rig for wind tunnel testing of bridge deck section models in arbitrary motion. J. Wind Eng. Ind. Aerod. 164, 152–163, 2017.

Vapnik, V.N., 1995. The Nature of Statistical Learning Theory. Springer, New York.

Wang, H., Wu, T., 2020. Knowledge-enhanced deep learning for wind-induced nonlinear structural dynamic analysis. J. Struct. Eng. 146 (11).

Wang, H., Zhang, Y.-M., Mao, J.-X., Wan, H.-P., 2020. A probabilistic approach for short-term prediction of wind gust speed using ensemble learning. J. Wind Eng. Ind. Aerod. 202.

William, K., 1939. MInima of Several Variables with Inequalities as Side Conditions. University of Chicago, Chicago. Thesis (S.M.).

Wu, T., Kareem, A., 2011. Modeling hysteretic nonlinear behavior of bridge aerodynamics via cellular automata nested neural network. J. Wind Eng. Ind. Aerod. 99, 378–388, 2011.

Xu, Y.L., Zhu, L.D., 2005. Buffeting response of long-span cable-supported bridges under skew winds. Part 2: case study. J. Sound Vib. (281), 675–697.

Zhu, L.D., Xu, Y.L., 2005. Buffeting response of long-span cable-supported bridges under skew winds. Part 1: theory. J. Sound Vib. 281 (3–5), 647–673.

II

Castellon D., Fenerci A., Øiseth O.

Environmental contours for wind-resistant bridge design in complex terrain

Journal of Wind Eng. Ind. Aerodyn. (p. 104943, vol. 224 2022)

Contents lists available at ScienceDirect

Journal of Wind Engineering & Industrial Aerodynamics

journal homepage: www.elsevier.com/locate/jweia

Environmental contours for wind-resistant bridge design in complex terrain

Dario Fernandez Castellon [a,*], Aksel Fenerci [b], Ole Øiseth [a]

[a] *Department of Structural Engineering, Norwegian University of Science and Technology, Richard Birkelands Vei 1A, Trondheim, Norway*
[b] *Department of Ocean Operations and Civil Engineering, Norwegian University of Science and Technology, Larsgårdsvegen 2, 6025, Ålesund, Norway*

ABSTRACT

Accurate estimation of the extreme wind fields is crucial for long-span bridge design. The current practice is focused on estimating the extreme mean wind speed, neglecting the inherent uncertainty in the turbulence model parameters. However, full-scale measurements on bridges show that such uncertainties are significant and should be considered in design. Here, the environmental contour method (ECM) is used to obtain long-term extreme wind fields considering uncertainties from the mean wind speed, turbulence intensities and spectral parameters measured at the Sulafjord Bridge site. Design contours of combinations of wind field parameters are obtained for target return periods of 4, 50 and 100 years. The contours are based on a proposed probabilistic modeling strategy that combines hindcast mesoscale simulations and field measurements. The contour estimates are also compared with state-of-the-art design values from the design recommendations. It is concluded that the environmental contours provide a more complete and yet intuitive description of the wind field at the bridge site compared to the current design methodology. The ECM is found suitable for obtaining design wind fields at new long-span bridge sites as it makes use of the limited site data more efficiently and it is still easy-to-use for the practicing engineer.

1. Introduction

General practice in bridge design establishes the structural response based on extreme values of wind speeds for long-term return periods (CEN, 2004). In the current design practice, the corresponding design wind loads are estimated using the mean wind speed as the sole stochastic variable, whereas other turbulence-related parameters are treated deterministically, usually dependent on the mean wind speed. However, monitoring campaigns in complex terrain showed that most of the scatter in measured structural response is strongly related to randomness in turbulence-related parameters (Fenerci et al., 2017). The observations show that the extreme structural response does not necessarily occur at the extreme value of mean wind speed but at relatively lower wind speeds with more severe turbulence parameters, such as turbulence intensity. Site measurements of wind and bridge response expose the necessity of design methodologies that consider the stochastic variability in wind variables, such as turbulence intensities, spectral parameters, spatial correlation of turbulence, and incoming wind direction together with the usual mean wind speed (Wang et al., 2013), (Li et al., 2021).

Relevant studies on wind characterization with probabilistic turbulence modeling are not abundant (Fenerci and Øiseth, 2018), (Solari and Piccardo, 2001). On the other hand, there are many studies in the literature about the assessment of structural wind-induced effects using probabilistic frameworks; however, the randomness is usually limited to the structural or aerodynamic parameters and the mean wind speed (Davenport, 1983; Solari, 1997; Pagnini and Solari, 2002; Pagnini, 2010; Seo and Caracoglia, 2012, 2013; Kareem, 1987; Ciampoli et al., 2011). Uncertainty in turbulence itself has been overlooked except for a few studies (Solari and Piccardo, 2001), (Lystad et al., 2018). In that regard, Lystad et al. used the environmental contour method (ECM) to estimate extreme wind fields for the Hardanger Bridge site (Lystad et al., 2020). The ECM obtains combinations of environmental parameters with a selected return period from their joint distribution (Winterstein et al., 1993), (Haver and Winterstein, 2009). Contours may be obtained using different methods, such as the inverse first-order reliability method (IFORM), the inverse second-order reliability method (ISORM), the highest density contour method (HDC) or Monte Carlo simulations (Winterstein et al., 1993), (Chai and Leira, 2018; Haselsteiner et al., 2017; Bang Huseby et al., 2013). Applications of the ECM have been extensively covered in the marine technology and wind energy industries, where researchers have used the method to determine the design loads of offshore platforms within a probabilistic framework (Naess and Moan, 2012; Moan et al., 2005; Saranyasoontorn and Manuel, 2004, 2006; van de Lindt and Niedzwecki, 1997; Niedzwecki et al., 1998; Vanem, 2019; Montes-Iturrizaga and Heredia-Zavoni, 2015; Heredia-Zavoni and Montes-Iturrizaga, 2019; Moriarty et al., 2002; Fitzwater et al., 2003; Raed et al., 2020; Karmakar et al., 2016; Velarde

---

Abbreviations: ECM, Environmental Contour Method; IFORM, Inverse First Order Reliability Method; CDF, Cumulative Distribution Function.

* Corresponding author.

E-mail addresses: dario.r.f.castellon@ntnu.no (D.F. Castellon), aksel.fenerci@ntnu.no (A. Fenerci), ole.oiseth@ntnu.no (O. Øiseth).

https://doi.org/10.1016/j.jweia.2022.104943
Received 23 June 2021; Received in revised form 25 January 2022; Accepted 16 February 2022

et al., 2019). Environmental contours have also been used to characterize the seismic hazard and derive the seismic design response spectra (Bazzurro et al., 1996; Van De Lindt and Niedzwecki, 2000; Loth and Baker, 2015). However, in design against wind actions on long-span bridges, the method remains largely unexplored despite the remarkable potential advantages.

Recently, Lystad et al. (2020) showed environmental contours for the Hardanger Bridge site based on a probabilistic wind field model from Fenerci and Øiseth (2018a) which was based on wind measurements on an existing bridge (Lystad et al., 2018). The results obtained for the Hardanger Bridge showed weaknesses in the current design methodology and motivated extension of the ECM to the structural design of new bridge sites. However, an obvious challenge that arises in the design of new bridges is obtaining data that are representative of extreme wind conditions because extreme wind conditions are inferred from measurement campaigns of relatively short duration. Additionally, wind measurements for new bridges are performed at meteorological stations in the vicinity of the site, instead of the midspan of the bridge, where the conditions are most relevant for bridge design. Here, we will attempt to extend the methodology to a new bridge site in complex terrain.

This paper presents environmental contours for the Sulafjord Bridge site to investigate the potential application of the ECM in the design of long-span bridges. Contours were obtained from the joint probability distribution of the mean wind speed, turbulence intensities and turbulence spectral parameters for each incoming wind direction. The joint turbulence model was established with a novel strategy where data from the 4-year mast measurement campaign (Furevik et al., 2020) and 10-year hindcast mesoscale simulations are combined, exploiting the advantages of both datasets. The contours represent the extreme wind fields for 4-, 50- and 100-year return periods.

This paper is outlined as follows. Section 2 presents the bridge site, measurement campaign, and hindcast data, including histograms of wind speed and direction, as well as the wind roses. This section expands the findings of the Sulafjord measurement campaign reported by Castellon et al. (Castellon, 2019) and Midjiyawa et al. (2021) and discusses how the dataset can be used to obtain the best possible wind field model for bridge design. Section 3 presents the proposed probabilistic modeling strategy, which is essentially a joint probability distribution of all the wind field parameters. The model is based on the joint lognormal distribution for turbulence intensities and turbulence spectral parameters that are dependent on the mean wind speed and direction. A Weibull distribution is used for the mean wind speed, and a discrete division for the mean wind direction is assumed. Section 4 presents the environmental contour lines for 4-, 50- and 100-year return periods and contour surfaces for a 100-year return period. The contour lines give combinations of two environmental parameters, while the surfaces correspond to combinations of three parameters. The four-year return period corresponds to the duration of the measurement period, whereas the results for 50- and 100-year return periods can be applied in bridge design. Section 5 presents the results and discusses the methodology's applicability to bridge design, including a comparison with reference values from the current design practice. Section 5 also contains modeling limitations and provides recommendations for future implementation of the ECM.

2. Wind conditions at the Sulafjord Bridge site

2.1. Bridge site

The Sulafjord is a Norwegian fjord located 10 km southwest of the city Ålesund on the western coast of Norway. The fjord is oriented from southeast to northwest, and it is approximately 12 km long, 4 km wide, and has a maximum water depth of 450 m. Fig. 1 shows the surroundings and the topography of the fjord, which is largely characterized by mountainous terrain with elevations of approximately 500 m on both sides, directing the wind flow through the fjord. Fig. 2 shows a picture of the fjord surroundings from the bridge location towards the north and south. Fig. 2 a) also shows the island Godøya, which is located on the northern side of the fjord. The island partly shields the fjord from the winds coming directly from the sea (Castellon, 2019). Fig. 3 shows an illustration of the Sulafjord suspension bridge adapted from illustrations by the Norwegian Public Roads Administration (NPRA) (Vegvesen, 2016).

2.2. Measurement campaign

Beginning in 2014, a wind measurement campaign led by the NPRA was deployed. This campaign aims to characterize the wind conditions in the Sula, Halsa and Vartdal fjords (Furevik et al., 2020). The data are handled by the Norwegian Meteorological Institute and are openly

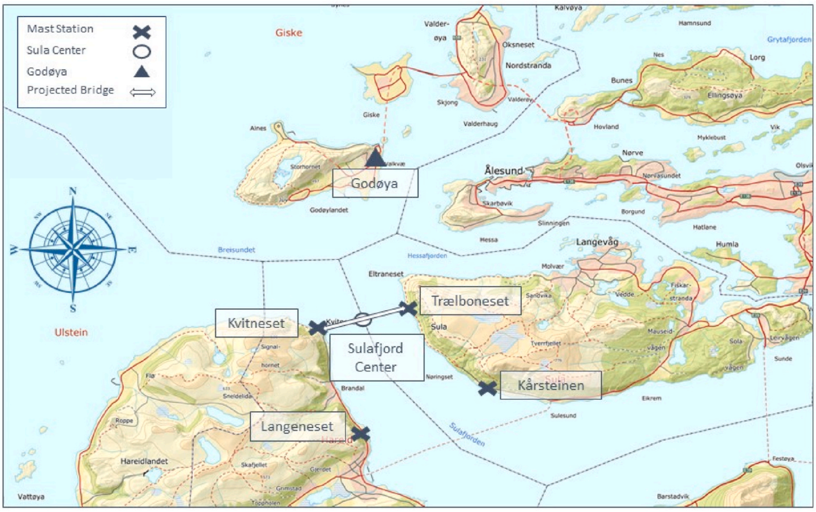

Fig. 1. Topographical map of the Sulafjord site (adapted from https://norgeskart.no/- ®norgeskart Norwegian Mapping Authority).

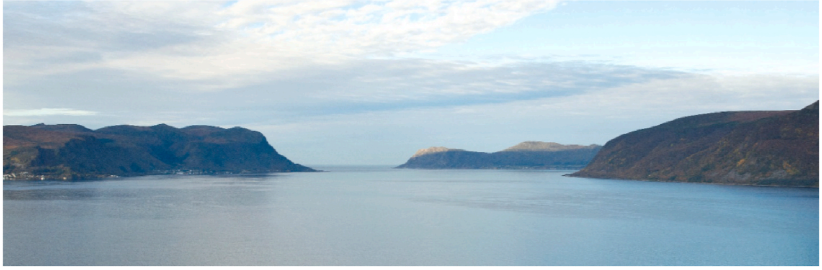

a) North view

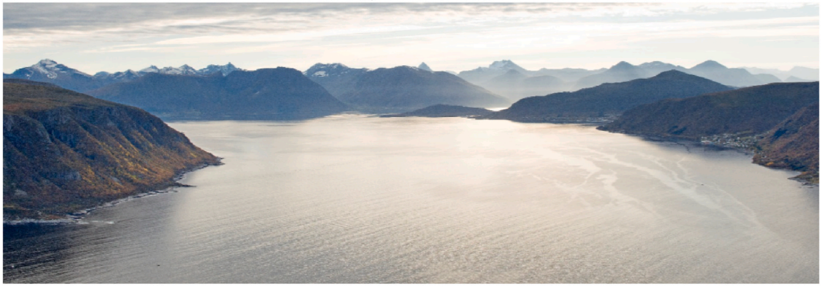

b) South view

Fig. 2. The bridge site. (Images courtesy of NPRA).

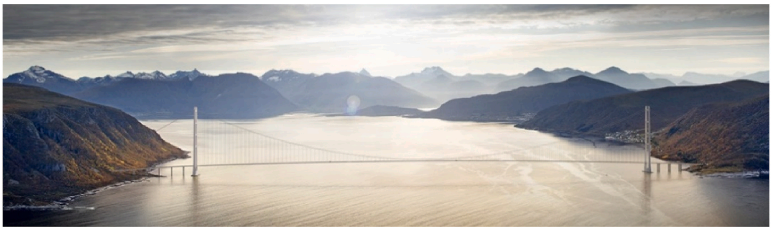

Fig. 3. Illustration of the Sulafjord suspension bridge. (Image courtesy of NPRA).

available (Norwegian Meteorological Institute, 2020). Four stations from the campaign are located at the Sulafjord site (cross symbols in Fig. 1), and Table 1 shows their geographical coordinates.

Each station is composed of a meteorological mast. The masts are equipped with wind sensors at different heights, to capture the vertical wind profile. The WindMaster Pro 3-Axis anemometers (Gill Instruments Limited) were used which can measure wind gusts up to 65 m/s. The speed resolution is 0.01 m/s, and the direction resolution is 0.1°, while the accuracy at 12 m/s is reportedly $<1.5\%$ RMS and 2° for speed and direction, respectively. Table 1 also shows the number of sensors and their altitude with respect to the sea level for each station.

2.3. Wind data from meteorological masts

The measurement data were analyzed to develop a statistical model of the wind conditions at the site. In total, 151,505 10-min intervals from sensors at approximately 50 m above sea level were analyzed. This elevation corresponds to the lowest sensor at Kvitneset and the second lowest at the other stations and most representative of the bridge height. Recordings with anomalies such as system log-out or missing data, within the averaging period of 10-min, are disregarded from the analysis as they cause irregularities in the power spectrum estimation. Further details of data processing are explained in section 2.3.3.

Table 1
Sulafjord wind mast station coordinates.

Station name	Latitude	Longitude	Sensors	Altitude (m)
Kvitneset	62°25′17.74"N	6° 0′4.03"E	3	92.5-71.5-44.5
Trælboneset	62°25′39.47"N	6° 3′45.45"E	3	76.8-48.3-27.3
Langeneset	62°23′10.68"N	6° 1′52.72"E	4	94.8-75-50-27
Kårsteinen	62°24′0.48"N	6° 7′9.82"E	3	62.8-40-13.4

The wind data are given in polar coordinates and need to be transformed to a Cartesian coordinate system aligned with the 10-min mean wind direction.

$$\begin{aligned} V+\ u(t) &= V_p(t)cos\{\varphi(t)-\overline{\varphi}\} \\ v(t) &= V_p(t)sin\{\varphi(t)-\overline{\varphi}\} \\ w(t) &= W(t)-\overline{W} \end{aligned} \tag{1}$$

Equation (1) shows the transformation of the wind velocity in polar coordinates with the magnitude $V_p(t)$ and direction $\varphi(t)$ into mean wind speed V and mean wind direction $\overline{\varphi}$ and the wind turbulence decomposition into along-wind $u(t)$, cross-wind $v(t)$ and vertical $w(t)$ components. Recordings with a mean speed below 5 m/s were discarded from the analyses as such records tend to be severely nonstationary due to rapid changes in temperature and wind direction. Such data can however be disregarded as they won't cause significant structural responses and therefore not relevant for the application here, which is focused on extreme wind fields. Fig. 4 shows the histograms of the mean wind direction, $\overline{\varphi}$, from the mast-measurements where the north is aligned with zero. The histograms show clusters of samples at specific directions which are mainly governed by the terrain's topography. The cutoff-directions of the clusters were chosen corresponding to the peaks of the histograms. The figures show that there are two main directions at Trælboneset, Langeneset and Kåresteinen, while there are three directions at Kvitneset. The main directions were divided into these sectors such that wind recordings from different topographical conditions could be studied separately. The main directions are shown by dashed lines in the histograms and Table 2 reports their directional intervals. Trælboneset station shows the dominant cluster in the incoming direction interval 100°–230°. Further details about the topographic influence over the mentioned behavior was explored with the wind rose diagrams that will be presented in next section.

2.3.1. Wind roses

Fig. 5 shows wind roses of the stations' mean wind speeds on top of the topographical map. The map clearly illustrates that there are tall mountains close to the masts and that the terrain by the masts will influence the wind recordings severely for some directions. It is therefore not straightforward to compare the wind roses at the four masts. The wind roses at Trælbonset and Kvitneset shows that the main incoming wind direction is from south in both locations. This behavior can be explained by the island Godøya (Fig. 1), which partially shields the two locations from winds coming from the open sea. A similar pattern would normally be expected at Kåresteinen and Langeneset due to their close location. Nonetheless, their wind roses are significantly different. The mast at Langeneset is partly shielded from winds approaching from southwest by the tall mountain close by. Similarly, the winds coming from south are severely obstructed by the tall mountain behind the mast at Kåresteinen. This illustrates that the measurements gathered at Langeneset and Kåresteinen are not entirely representative for the southerly winds at a potential bridge crossing between Kvitneset and Trælboneset. The wind roses also illustrate that the wind field is shaped by the mountains along the fjord since the main wind directions tend to be aligned with the tall mountain sides for some of the wind directions. It should also be noted that the shape of the wind roses strongly depends on how many sectors that are used.

Table 2
Main directional sectors.

Location	Sector 1	Sector 2	Sector 3
Kvitneset	100°–230°	260°–360°	370°–410°
Trælboneset	120°–230°	280°–400°	–
Kårsteinen	90°–150°	220°–340°	–
Langeneset	80°–240°	290°–360°	–

According to the feasibility studies by the NPRA (Vegvesen, 2016), the most convenient track for a suspension bridge crossing the fjord will be near the Kvitneset and Trælboneset stations (thick line in Fig. 1). Fig. 6 and Fig. 7 show the histograms of the mean wind speed at both locations considering the directional division. Fig. 6 from Kvitneset shows sector 2 (250°–320°) as the dominant sector with the highest recorded mean wind speed and sector 1 (120°–210°) as the most populated sector with largest number of samples. Fig. 7 shows Trælboneset sector 1 as both dominant and most populated. The histograms and wind roses show that the winds coming from the seaside have lower mean wind speeds at Trælboneset station compared to other stations. The main reason for this behavior is the effect of the Godøya island which protects the Trælboneset-side of the track from the open sea winds while the Kvitneset-side is partially uncovered from northwestern sea winds. Evidence of this is clearly found from the Kvitneset recordings in which the maximum mean wind speed of 25.7 m/s was observed in the sector not protected by Godøya. The shielding effect also implies that the most critical wind conditions on the Sulafjord bridge are expected to come from the southern direction approaching nearly perpendicular to the bridge deck. The measurements gathered at Trælboneset are clearly most representative for the southerly winds approaching the bridge crossing since the southerly winds approaching Kvitneset has passed over a mountain close by. The data from Trælboneset is therefore used to

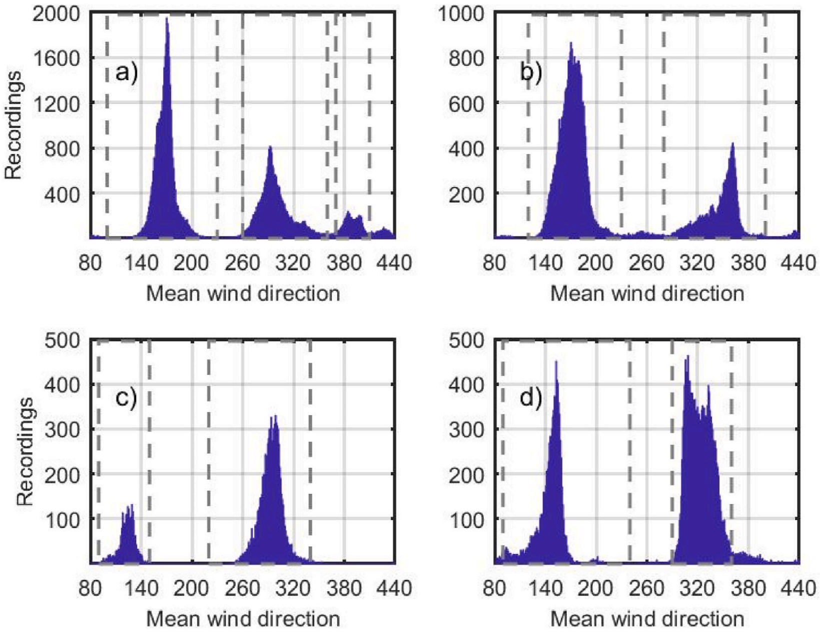

Fig. 4. Direction histogram station: a) Kvitneset b) Trælbodneset c) Kårsteinen d) Langeneset.

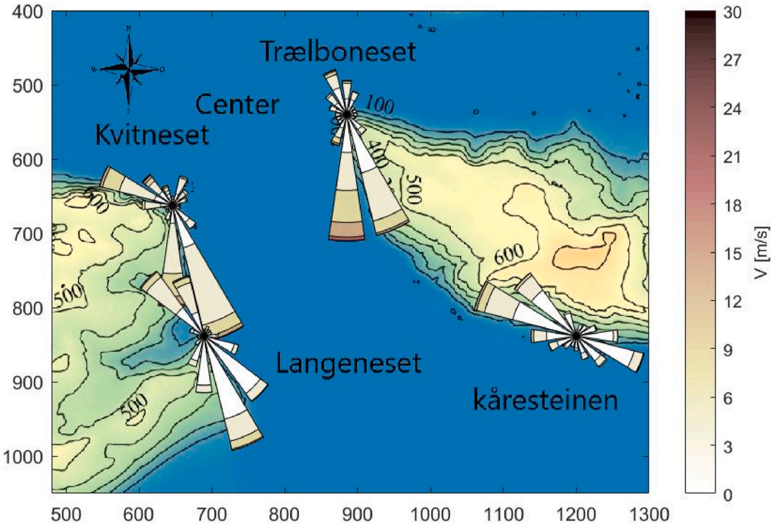

Fig. 5. Wind rose plot mean speed.

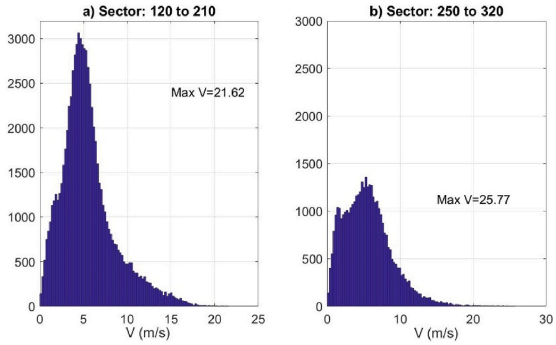

Fig. 6. Mean wind speed histograms for the Kvitneset station from measured data at a) Sector 1 b) Sector 2.

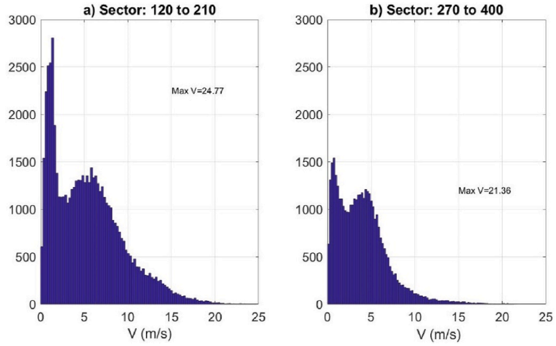

Fig. 7. Mean wind speed histograms for the Trælboneset station from measured data at a) Sector 1 b) Sector 2.

obtain the results presented in this paper.

2.3.2. Data processing

The recordings were resampled at 2 Hz to remove high-frequency content associated with possible vibration of the mast. The resampling does not introduce any significant inaccuracies since the wind characteristics will be applied in the design of a long-span bridge. In these types of projects the responses and associated load effects are dominated by vibration modes with natural frequencies much lower than 1 Hz. In addition, high-pass filtering was used to subtract nonstationary trends, as this technique better removes the variances in ramp-like events in the recordings (Hannesdóttir et al., 2019) than detrending each 10 min segment. The filter was a minimum-order, linear-phase, finite impulse response (FIR) with pass frequency $f_{pass} = 1/300\ hz$, steepness $s = 0.85$ and transition width $W = 5x10-4$, following the recommendations in (Hannesdóttir et al., 2019).

2.3.3. One-point turbulence spectrum

The turbulence was modeled from its one-point Kaimal-type power spectrum S_n, Equation (2) (Kaimal et al., 1972). Model uncertainties were introduced by assuming the mean wind speed (V), the along-wind, cross-wind and vertical turbulence intensities (I_u,I_v, I_w), and the spectral parameters (A_u,A_v,A_w) as stochastic variables. Despite the Kaimal-type power spectrum don't consider turbulence length scales in its formulation, the spectral parameters (A_u,A_v,A_w) are proportional and analogous to these quantities (Fenerci et al., 2017), (Fenerci and Øiseth, 2017). Parameters such the spatial coherence and the wind angle of attack are outside the capabilities of the measurement system because of the long distance between stations and the absence of an appropriate structural reference frame crossing the fjord site. In a design situation, uncertainties in those parameters can be modeled after measurements at similar sites, in the case of absence of such data.

$$\frac{S_n f}{(V\,I_n)^2} = \frac{\mathrm{A}_n f_{z_h}}{\left(1 + 1.5\mathrm{A}_n f_{z_h}\right)^{5/3}},\ f_z = \frac{z_h f}{V},\ I_n = \frac{\sigma_n}{V} \tag{2}$$

The subscripts $n \in \{u, v, w\}$ indicate the along-wind and vertical turbulence components, z_h is the reference height, f is the frequency and σ_n represents the standard deviations.

For the estimation of the spectral parameters (A_u,A_v,A_w), the power spectral density function (PSD) of the turbulence components was obtained by applying the Welch method, taking the average of 8 segments with a 50% overlapping and Hamming window. Then, the power spectra S_n from Equation (2) were fitted to the spectral parameters $(A_{u,}A_v,A_w)$ in the least square sense. As an illustration, overlapping fitted and measured power spectra from a recording registered on 01.01.19 at Trælboneset station from 14:40 to 14:50 corresponding to the annual highest mean speed are shown in Fig. 8. Scatter in the measured PSD comes from the spectral estimation. The spectra have been estimated using the Welch method. Smoother estimates can be obtained using shorter windows, but this comes at the price of lower resolution and higher bias. The presented estimates provide a balance between scatter (variance) and bias & resolution of the estimate. The distributions of the $(A_{u,}A_v, A_w)$ coefficients are not very sensitive to the applied settings in the spectral estimate when least squares are used to fit the model. Along with the spectral fittings of Figs. 8 and 9 shows the time-histories of the turbulence components on the same interval. The time-histories show a stationary behavior. The figure also includes the time-history of the vertical angle of attack (β), which is a parameter of paramount importance for the bridge's non-linear aerodynamic behavior. The time-series of the angle of attack show that this value oscillates between −15 and 20°, this range is slightly higher than that reported on the Hardanger bridge (Barni et al., 2021). In contrast, the mean values of the vertical angle of attack shown in Fig. 10 respect to the mean wind speed correspond to observations of the Hardanger bridge (Fenerci and Øiseth, 2017). Thus, suggesting that the angle of attack at the Sulafjord bridge may have higher variation than at the latter location. To determine the actual effect of this parameter over the Sulafjord bridge, a complete study of the aerodynamic derivatives is required, however, such study is outside the scope of this paper. Nonetheless, with the probabilistic modeling provided here, it is possible to reproduce the vertical angle of attack for practical engineering applications, since for such cases, the vertical angle of attack is handled with simulated time-series depending on the spectral densities and the mean wind conditions.

2.4. Hindcast wind data

In addition to the mast measurement data, hindcast simulations were performed by Kjeller Vindteknikk (Vindteknikk and og Vartdalsfjorden, 2018). Simulated mean wind velocities were obtained using the state-of-the-art mesoscale numerical weather prediction system, the Weather Research and Forecast model (WRF) work version 3.2.1 (UCAR and, 2013), (Skamarocket al., 2008). The modeling structure, physical packages, numerical routines and other details are given in (Klemp et al., 2007), (Michalakeset al., 2001). The geographical input data in the model were adapted from the National Oceanic and Atmospheric Administration (NOAA) for the entire domain except for Norway and Sweden, where N50 land data from the Norwegian Map Authority and map data from the Geografiska Severgedata (GSD)-Land Cover were used. The meteorological input data were adapted from the European Center for Medium-range Weather Forecasting (ECMWF) using a resolution of approximate 0.7° and 6 h interval data as boundary of the model. The hindcast data are fitted to meteorological observations in the area using an assimilation model that incorporates all available observation globally into a numerical weather prediction model that creates a description of the state of the atmosphere on a uniform horizontal grid four times a day. The assimilation model incorporates data from several thousand ground based observation stations, vertical profiles from radiosondes, aircrafts, and satellites and are therefore reasonably accurate (Deeet al., 2011), (Berrisfordet al., 2009). The model was set up with 4 nested domains from which the inner domain has a resolution of 500 × 500 m (Fig. 11). This is the highest resolution possible as the simulations are limited to meso-scale and not to local topographical effects. The simulation model has 51 layers in the vertical with eight layers in the lower 200 m. The WRF-model computes the variation in the wind

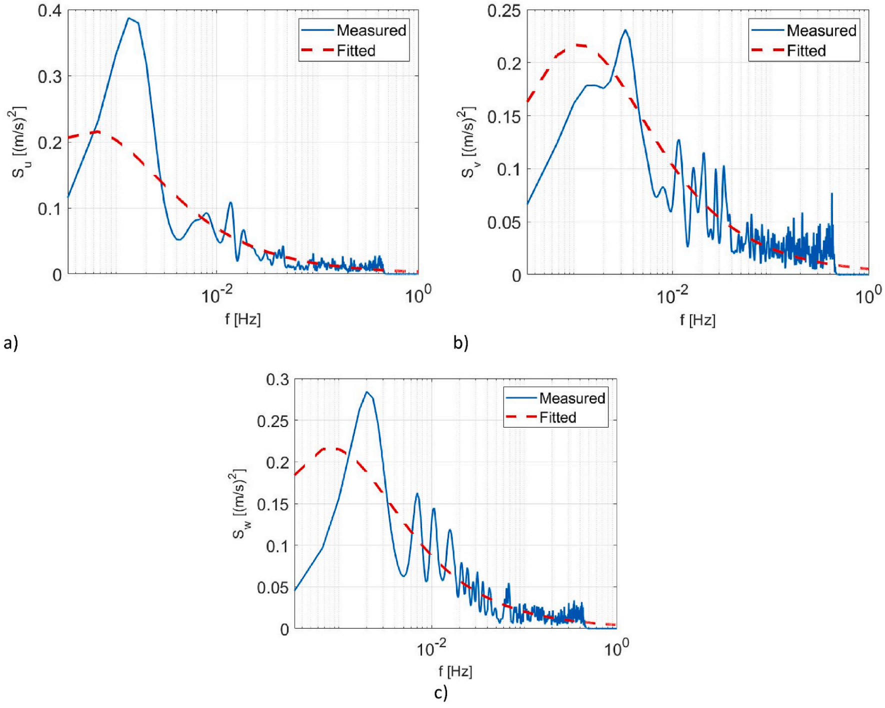

Fig. 8. Three components of the one-point spectrum 'max 2019' Record 01.01.19 from 14:40 to 14:50. a) Su b) Sv c) Sw.

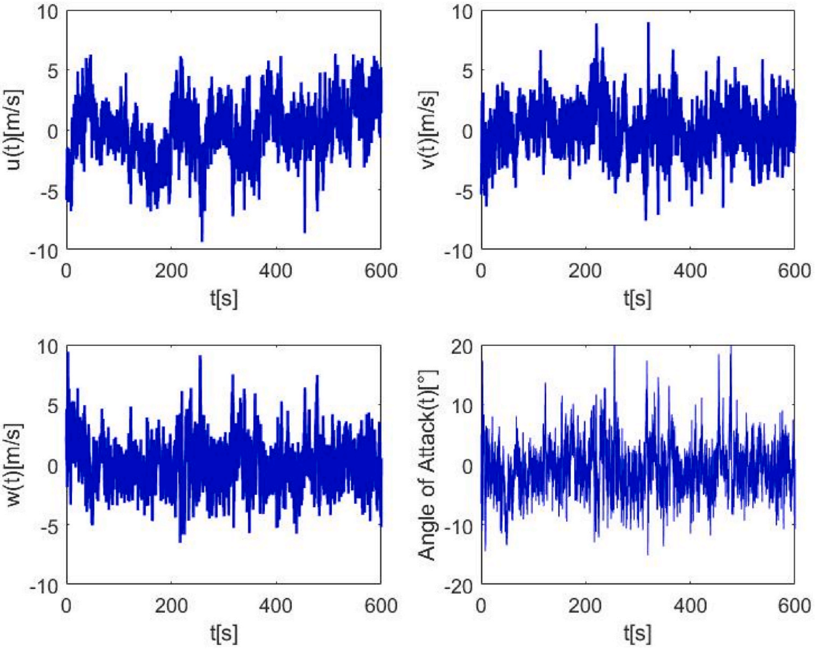

Fig. 9. Time-histories of the three components ‘max 2019′ Record 01.01.19 from 14:40 to 14:50. a) u b) v c) w d) angle of attack.

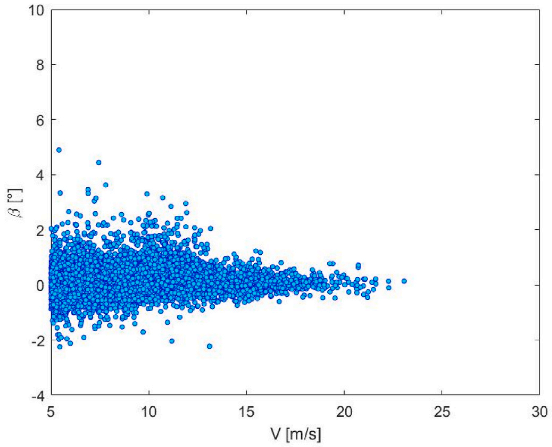

Fig. 10. Vertical angle of attack respect to mean wind speed.

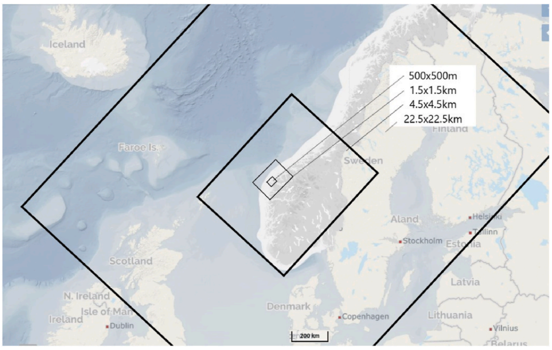

Fig. 11. Nested domains of hindcast dataset simulations (adapted from https://norgeskart.no/- ®norgeskart Norwegian Mapping Authority).

conditions for a time step from 1 to 108 s in the different domains increasing the time step with decrease in the resolution, achieving then a more realistic temporal development of the wind conditions. Data is stores every 1 h of simulation. More information about the hindcast data set may be found in (Vindteknikk and og Vartdalsfjorden, 2018).

The simulated dataset is 10 years long starting from January 2007. The dataset contains the mean wind speed and direction for 1-h intervals in the locations of the four mast stations in addition to the Sulafjord center (62°25′19.68"N, 6°01′52.68"E) (circle in Fig. 1). The simulations were carried out at 10, 50, 70 and 100 m above the ground or water level. Histograms of the 1-h direction distribution for the different sites are presented in Fig. 12, while the principal sectors are reported in Table 3. The figure shows a similar trend in the distribution peaks as the site measurements. However, an increased scatter of samples towards the distribution valleys may be observed, with the most severe situation for the Kårsteinen station in which the peaks can barely be differentiated from the valleys. Validation of the hindcast data is presented in (Vindteknikk and og Vartdalsfjorden, 2018).

Similar to the recorded data, the wind rose of the mean wind speed for the simulation sites is shown in Fig. 13. The analyzed data correspond to the simulations at a 50-m height since it represents the bridge height. Simulated samples below 5 m/s were disregarded from the plots. It is not expected that wind roses from Figs. 5 and 13 coincide exactly since the wind flow is affected by the local topographical effects not included in meso-scale simulations. Then, the differences between the wind roses of Kårsteinen and Langeneset are plausible, and hence the erection of several mast stations in the area. On the other hand, local

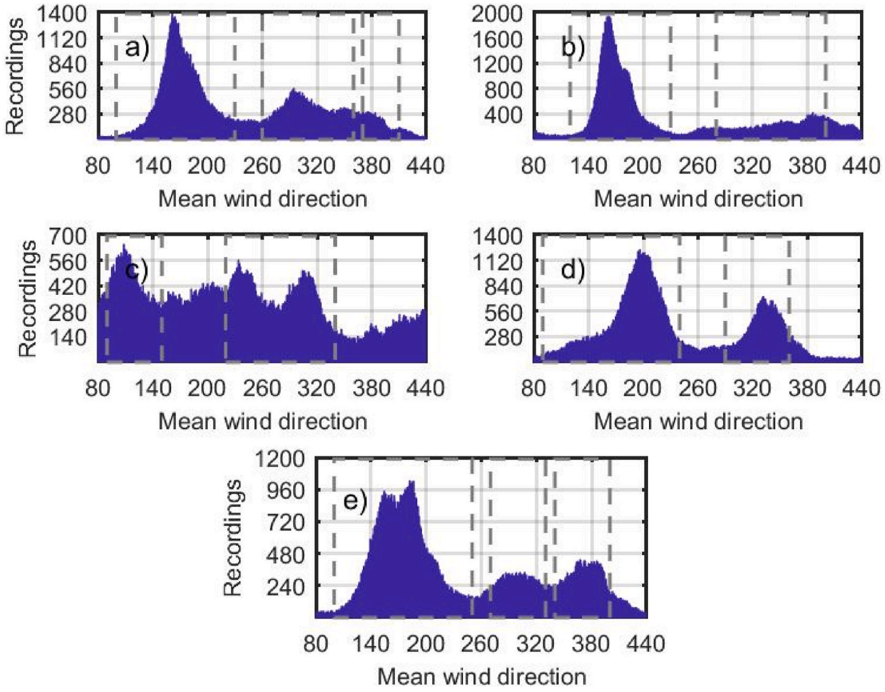

Fig. 12. Direction histogram from hindcast data locations: a) Kvitneset b) Trælbodneset c) Kårsteinen d) Langeneset e) Sulafjord center.

Table 3
Main directional sectors.

Location	Sector 1	Sector 2	Sector 3
Kvitneset	100°–230°	260°–360°	370°–410°
Trælboneset	120°–230°	280°–400°	–
Kårsteinen	90°–150°	220°–340°	–
Langeneset	80°–240°	290°–360°	–
Sulafjord center	100°-250	340°–400°	270°–330°

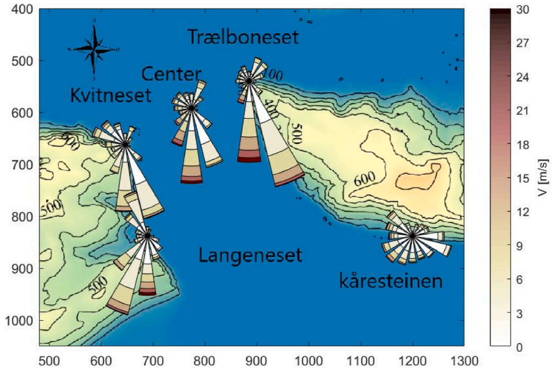

Fig. 13. Wind rose plot mean wind speed hindcast data.

topographical effects don’t present a major complication at the Sulafjord center location, which is the most representative for the bridge and meso-scale simulations are still the best option for extreme mean wind velocity estimations because of their longer observation period.

2.4.1. *Wind speed histograms*

In a similar way as Figs. 6 and 7, Fig. 14 contains the histograms of the mean wind speed from Sulafjord center location but using the hindcast data. In this case the sector from 100° to 250° is both the dominant and most populated sector.

3. A probabilistic model of the wind field

A probabilistic model of the wind field is defined by a joint distri-

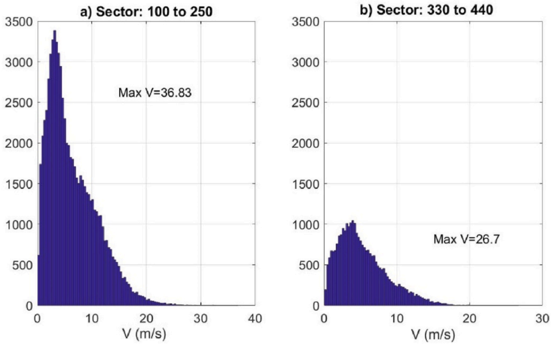

Fig. 14. Mean wind speed histograms of the Sulafjord center station from hindcast data at a) Sector 1 b) Sector 2.

bution of the turbulence parameters (Fenerci and Øiseth, 2018), (Lystad et al., 2020). Introducing W as the wind state variable collecting the wind parameters, its joint distribution can be expressed as the product of the conditional distributions:

$$\begin{aligned} &F_W(W) = F_V(V)^* F_{I_u,I_v,I_w,A_u,A_v,A_w|V}\,(I_u,I_v,I_w,A_u,A_v,A_w|V) \\ &W = [\,V,\ I_u,I_v,I_w,A_u,A_v,A_w] \end{aligned} \tag{3}$$

Fenerci et al. (2018) showed that the joint distribution can be expressed as the product of Weibull distribution of the mean wind speed and a joint lognormal distribution of the turbulence parameters. This is highly advantageous because the relation between the turbulence parameters can be determined by the correlation of parameters only. Fenerci et al. (2018) showed that the joint lognormal distribution fits the turbulence data of the Hardanger bridge. Whereas Lystad et al. (2020) showed that the Weibull fits the mean wind speed data for the same project. Using a similar approach, in this chapter the parameters Equation (3) will be derived for the Sulafjord site. Chapter 3.1 is devoted to the Weibull distribution of the mean wind speed and chapter 3.2 to the joint lognormal distribution of the turbulence.

Measured data was not available at the fjord center and meso-scale simulations don’t include turbulence effects. Therefore, a strategy combing both sources was implemented. The Weibull distribution of the mean wind speed was obtained using the meso-scale data as it covers a more extended period than the site measurements and it is possible to obtain the data at the desired midspan location. Subsequently, the joint lognormal distribution of turbulence parameters was obtained from the site anemometry measurements as the turbulence characteristics cannot be obtained from meso-scale simulations. However, as site measurements are not available at the fjord midspan, the turbulence parameters were assumed to be reasonably well represented by the measurements at the Trælboneset station. This follows both from simple considerations of the site topography (local effects are less expected) and the fact that the wind direction of the station matches the mesoscale simulations with good accuracy. Complementary arguments to the selection of Trælboneset station are discussed in section 3.2.

3.1. *Mean wind speed distribution*

The wind roses and wind histogram analysis showed that local topographical effects strongly influence the environmental variables. As discussed earlier, the dataset was split into sectors, where the dominant sector includes the recordings with the highest mean wind speeds. This information was further included in the probabilistic model by establishing the mean wind speed distribution from the dominant sectors at the Sulafjord center, $V = V|\overline{\varphi}_{dominant}$. The distribution for the mean wind speed F_V on Equation (3) is Weibull type with the following cumulative distribution function (CDF):

$$F_V(V) = 1 - \exp\left[\left(\frac{V}{\lambda}\right)^k\right] \text{; } for\ V > 0 \tag{4}$$

With k *and* λ as the shape and scale parameters, respectively. The parameters were adapted from the hindcast data as it covers a more extended period than the site measurements and it is possible to obtain the data at the desired midspan location.

3.1.1. *Extreme value distribution from hindcast data*

Directly fitting the Weibull distribution from Equation (4) to the available data yields a good match with the central behavior of the distribution. However, the accuracy is lost in the tail where the largest wind loading conditions are expected. Thus, the parent distribution was established in correspondence to a type 1 generalized extreme value distribution (Gumbel) from the annual largest mean wind speeds, F_Z, reported in the hindcast data. In this way, most of the weight was given to fit the tail of the parent distribution.

$$F_Z(z) = 1 - e^{-e^{-y}},\ y = \frac{z-\alpha_1}{\alpha_2} \tag{5}$$

Here, α_1 *and* α_2 are the location and scale parameters of the distribution, respectively, y is the reduced variate, and z is a variable relative to the mean wind speed. A linear variation was assumed between y and the wind speeds following the best linear unbiased estimator (BLUE) method (Lieblein, 1974). Then, F_Z was established from the annual largest recordings ranked in ascending order, such that the lowest maximum has the rank of $m = 1$, and the highest rank is $m = n$, as follows:

$$F_z(z) = \left[\frac{m}{n+1}\right] \tag{6}$$

The distribution parameters α_1 *and* α_2, and thus F_z, are obtained by a least-squares fit from the reduced variate, which was directly adapted from the hindcast data.

$$y(z) = -ln[-\ln(F_Z(z))] \tag{7}$$

Subsequently, F_V is established from F_Z utilizing the asymptotic theorem (Gumbel, 1958), i.e., F_V asymptotically approaches F_Z given that the number of short-term recordings in the one-year period, N, is sufficiently large and the statistical parameters of the individual recordings are independent. For the 1-h averaging period of the hindcast data, $N = 8760$ is sufficiently large to fulfil the requirement, and the parent distribution for the 1-h averaging period, $F_{V_{3600}}$, can be found as follows:

$$F_Z(V) = \left[F_{V_{3600}}(V)\right]^{N_{8760}} \leftrightarrow F_{V_{3600}}(V) = [F_Z(V)]^{1/N_{8760}} \tag{8}$$

A 10-min averaging period is typically used for structural design purposes, however the standard in meteorological forecast is 1-h intervals. Thus, a transformation between the averaging periods is required to proceed with the structural design. Direct conversion of averaging periods of mean wind speed records is not possible (Harper et al., 2009). Then, transformations must be completed on their estimates. In this work, the adjacent short-term 10-min intervals in the 1-h periods were assumed to be independent events allowing to estimate the parent distribution of the 10-min mean wind speed, $F_{V_{600}}$, as shown in Equation (9). This assumption doesn’t involve a loss in accuracy given that the number of cycles of interest (10-min intervals in one year) is larger than the cut-off step-memory of stationary dependance (number of cycles in which the maximum events are no longer related), thus, the dependance between adjacent cycles is effectively negligible (Naess et al., 2013).

$$\left[F_{V_{3600}}(V)\right]^{N_{8760}} \cong \left[F_{V_{600}}(V)\right]^{6*N_{8760}} \leftrightarrow F_{V_{600}}(V) \cong [F_Z(V)]^{1/N_{52560}} \tag{9}$$

Fig. 15 a) shows the reduced variate for the recordings of the dominant wind direction (100°–250°) at the Sulafjord center, while Fig. 15 b) shows the associated annual Gumbel probability distribution. In both cases, the annual largest wind speeds are represented with circles. The velocities in the range of 25–35 are emphasized, as the design conditions are expected in the distribution’s tail. Thus, the Weibull parent distribution establishment is focused on velocities from 25 to 35 m/s. Fig. 15 c) shows the scaled Gumbel CDF $[F_Z(V)]^{1/N_{52560}}$ in the continuous line and the fitted 10-min short-term Weibull CDF in the discontinuous line, $F_{V_{600}}$.

The parameters from the 10-min Weibull type parent distributions are shown in Table 4.

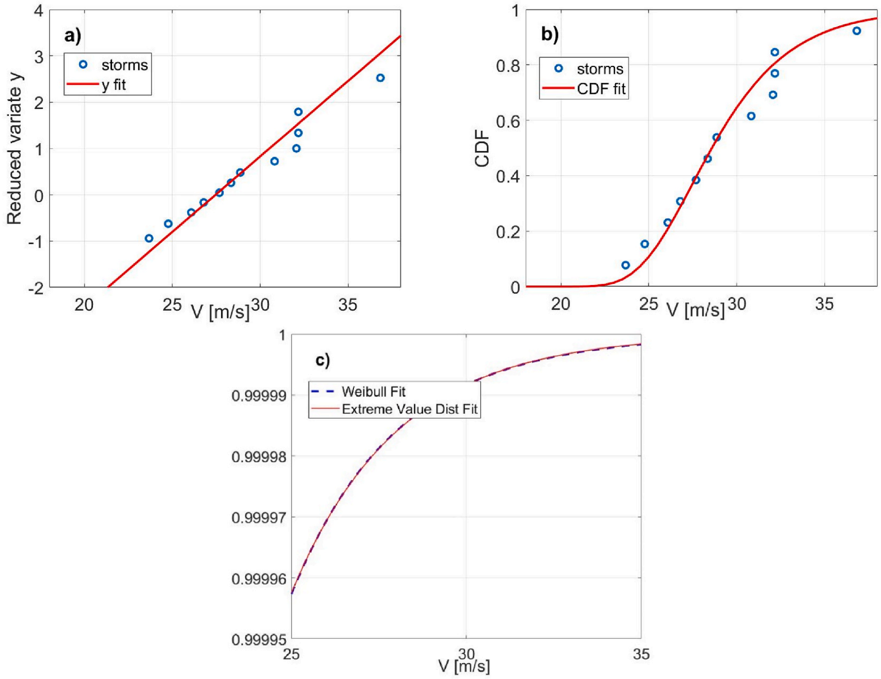

Fig. 15. Extreme distribution fit of the Sulafjord center from the hindcast data dominant sector a) Reduced variate b) Annual CDF c) 10-min CDF fitting.

Table 4
Parameters of the parent distributions from hindcast data for Eq. 3

Location	Sector	λ	k
Sulafjord center	100°–250°	1.52	0.82

3.2. Statistical properties of the turbulence parameters

Section 3.1 explained how to obtain the distribution for the mean wind speed. To complete the probabilistic model of Equation (3), This section explains how to obtain the joint distribution of the turbulence intensities (I_u,I_v, I_w) and spectral parameters (A_u,A_v,A_w), conditional to mean wind speed, $F_{I_u,I_v,I_w,A_u,A_v,A_w|V}$. Turbulence parameters are adapted from mast measurements according to the following procedure:

First, the data was divided in directional sectors from Table 2. Then, recordings with mean wind speeds below 11 m/s were disregarded from the analysis as attention is paid to the tail of the mean wind speed distribution. Subsequently, the data was divided depending on the mean wind speed in segments of 2 m/s, in this way trends of the joint distribution parameters respect to mean wind speed can be highlighted. On each segment of data, the parameters of the lognormal distribution and the correlation coefficients were fitted using the method of moments. Finally, the trends in the distribution and correlation parameters respect to the mean wind speed were fitted using least squares.

The size of the segments was chosen by engineering criterion. Small segments would leave few samples for distribution fitting whereas large segments would leave few points for trend fitting respect to mean wind speed. 2 m/s balanced the accuracy in both type of fittings given the number of recordings available.

The result is a joint lognormal distribution whose parameters are dependent of the mean wind speed. Parameters of a marginal lognormal distribution and correlation coefficients are described as follows:

$$f_{logn}(x|\widetilde{\mu},\widetilde{\sigma}) = \frac{1}{x\widetilde{\sigma}\sqrt{2\pi}}\exp\left\{\frac{-(Ln\,x-\widetilde{\mu})^2}{2\widetilde{\sigma}^2}\right\}$$

$$\widetilde{\mu} = \exp\left(\mu+\frac{\sigma^2}{2}\right),\ \widetilde{\sigma}^2 = \left[\exp\left(\sigma^2\right)-1\right]\exp\left(2\mu+\sigma^2\right) \tag{10}$$

$$\rho(x,y) = \frac{1}{N-1}\sum_{i=1}^{N}\left(\frac{x_i-\mu_x}{\sigma_x}\right)\left(\frac{y_i-\mu_y}{\sigma_y}\right)$$

$$\boldsymbol{R}_{xy} = \begin{bmatrix} 1 & \rho(x,y) \\ \rho(y,x) & 1 \end{bmatrix}$$

With, $f_{logn}(x|\widetilde{\mu},\widetilde{\sigma})$ the lognormal distribution a variable x and $\widetilde{\mu},\widetilde{\sigma}$ the lognormal mean and standard deviation (parameters of the distribution). $\rho(x,y)$, the correlation coefficient of the variables x *and* y, and $\boldsymbol{R}_{xy}$ the correlation matrix.

At middle of fjord there is not wind turbulence data. Therefore, turbulence conditions were adapted from the mast station that provided the most representative data. The wind roses from Figs. 5 and 13 show that most frequent and stronger winds for the fjord center come from the south and southwest and that this situation is also observed at Trælboneset. In addition, winds from south and southwest arrive mostly undistributed to Trælboneset making is suitable to represent the topographic conditions of the fjord center in these directions. Thus, the turbulence conditions at Trælbonset were used as the design conditions for the Sulafjord center.

Table 5
Number of samples at the interval division from measured data from the dominant sector at Trælboneset.

Speed interval	11–13	13–15	15–17	17-max
Samples	2681	1755	758	520

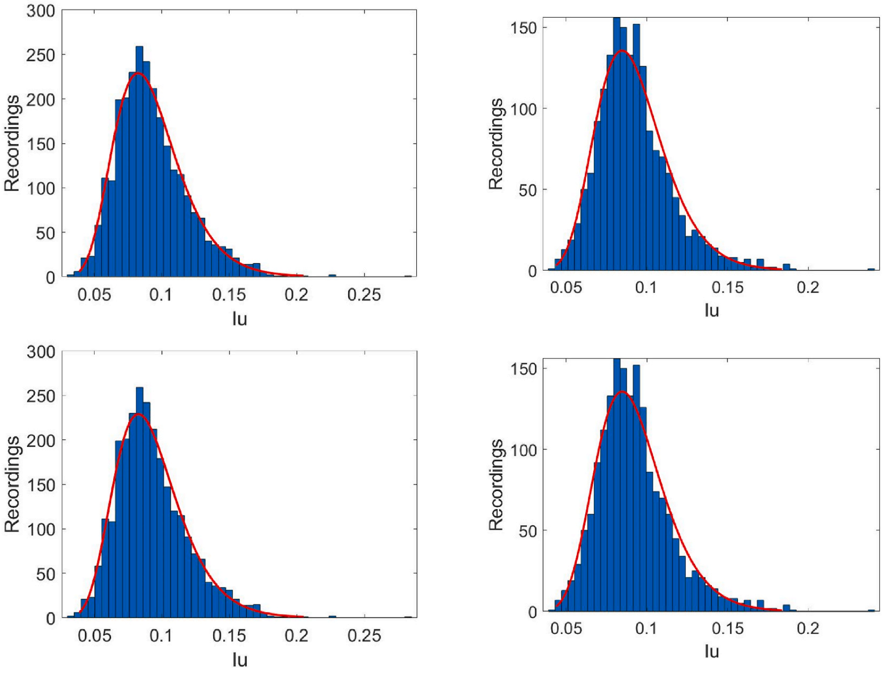

Fig. 16. Lognormal distributions for turbulence parameter I_u from the dominant sector at Trælboneset fitted at V = a) 11–13 m/s b) 13–15 m/s c) 15–17 m/s d) 17 m/s-max.

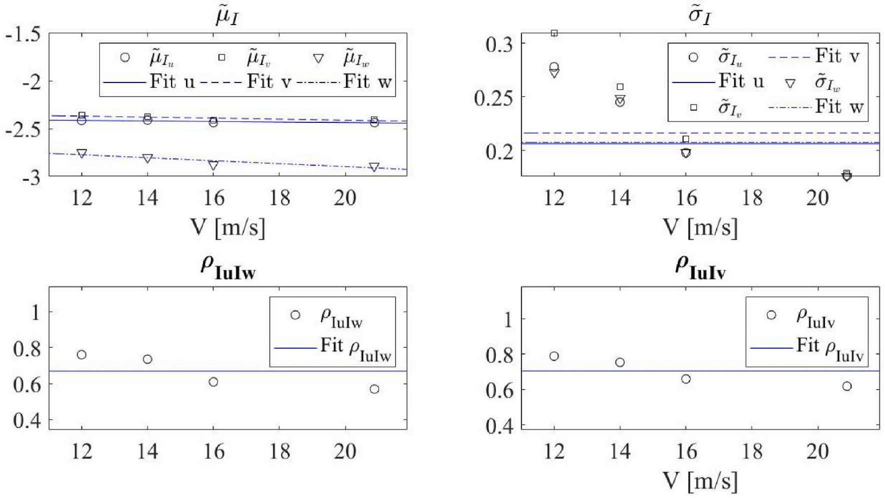

Fig. 17. Statistical parameter fit for the turbulence intensity: Lognormal parameter $\tilde{\mu}_I$, Lognormal parameter $\tilde{\sigma}_I$, Correlation coefficient $\rho_{I_uI_v}$, Correlation coefficient.$\rho_{I_uI_w}$

The number of samples in each discretization segment for the Trælboneset dominant sector (120°–230°) is reported in Table 5. As an example, Fig. 16 shows the lognormal distribution fittings for the I_u parameter for different mean wind speed segments on top of the histogram of the data.

Fig. 17 shows the variation in the lognormal distribution parameters of the spectral parameters $\widetilde{\mu}_{A_i}$ and $\widetilde{\sigma}_{A_i}$ with respect to the mean wind speed from Trælboneset dominant sector. Fig. 18 shows a similar plot for the turbulence intensity parameters $\widetilde{\mu}_{I_i}$ and $\widetilde{\sigma}_{I_i}$. $\widetilde{\mu}_{A_i}$, $\widetilde{\sigma}_{A_i}$ and the correlation coefficients are constant with respect to the mean wind speed, whereas $\widetilde{\mu}_{I_i}$ shows a linear variation. The variation of $\widetilde{\sigma}_{I_i}$, was adapted as constant despite it show a higher order trend. The reason behind this is that as less sampling points are present in the high mean wind speed

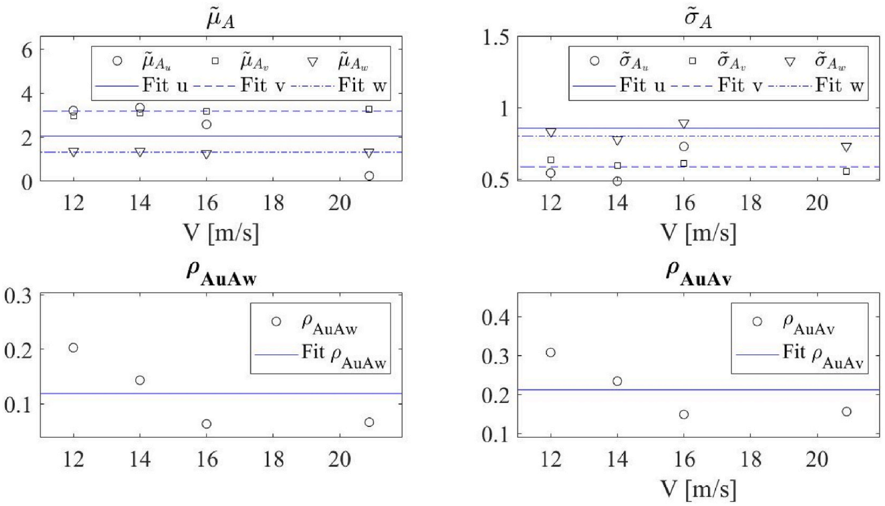

Fig. 18. Statistical parameters fit for the spectral quantities: Lognormal distribution parameter $\tilde{\mu}_A$, Lognormal distribution parameter $\tilde{\sigma}_A$, Correlation coefficient $\rho_{A_uA_v}$, Correlation coefficient.$\rho_{A_uA_w}$

Table 6
Statistical parameters of the turbulence model.

	$\tilde{\mu}$	$\tilde{\sigma}$
I_u	$-2.381-0.003V$	0.206
I_v	$-2.307-0.005V$	0.216
I_w	$-2.588-0.015V$	0.208
A_u	2.054	0.855
A_v	3.184	0.584
A_w	1.314	0.800

Table 7
Correlation coefficient fit matrix of the turbulence model.

	I_u	I_v	I_w	A_u	A_v	A_w
I_u	1.00					
I_v	0.71	1.00		Symmetric		
I_w	0.67	0.70	1.00			
A_u	0.00	0.00	0.00	1.00		
A_v	0.16	0.56	0.18	0.00	1.00	
A_w	0.00	0.00	0.47	0.00	0.19	1.00

range; this may lead to inaccuracies in the dispersion of the sample affecting the lognormal standard deviation. This effect is however more pronounced in the lognormal normal standard deviation than the lognormal mean, therefore, values of $\tilde{\mu}_{I_i}$ are still acceptable. This follows the recommendations found the literature (Fenerci and Øiseth, 2018), (Hannesdóttir et al., 2019). The values of the fitted parameters are reported in Table 6, while the correlation coefficient matrix is in Table 7. To simplify the modeling, correlation coefficients between −0.15 and 0.15 which are negligible for the calculations were not reported in the table.

4. Environmental contours

4.1. Environmental contour method

The established probabilistic model expresses the joint distribution of the correlated stochastic wind variables and provides the basis for obtaining the environmental contours. The ECM allows for the assessment of the model uncertainties considering multiple correlated stochastic variables. The method approximates the reliability integral based on an inverse application of the first-order reliability method (FORM) (Hasofer and Lind, 1974) (Winterstein et al., 1993):

$$p_e = P[g(\boldsymbol{X}) > 0] = \int_{g(X)>0} f_X(x)dx \tag{11}$$

where p_e is the exceedance probability of an extreme event, $\boldsymbol{X}$ ($\overline{\varphi}$,V,I_u,I_v, I_w, A_u,A_v, A_w) is the set of stochastic variables and $g(\boldsymbol{X})$ is the limit function, which represents the difference between a generic wind condition $W(\boldsymbol{X})$ and the extreme wind condition W_{RP}, which is associated with the long-term extreme value of $\boldsymbol{X}$ with a return period *RP in years.* $g(\boldsymbol{X}) = W(\boldsymbol{X}) - W_{RP}$.

For design applications, the probability of exceedance is fixed to a design practice (or construction code) through the long-term return period *RP* in years. Thus, this value can be computed for the given return period in terms of short-term processes with T_{st} duration in minutes.

$$p_e = \left[\frac{RP\ \text{x}\ 365.25\ \text{x}24\ \text{x}60}{T_{st}}\right]^{-1} \tag{12}$$

The set of stochastic variables $\boldsymbol{X}$ is transformed into a set of independent normally distributed variables, $\boldsymbol{U}(u_1, u_2, \ldots, u_n)$, given that the proper transformation rule is reversible. A detailed explanation of the method and its advantages may be found in (Winterstein et al., 1993). In the transformed space, the shortest distance between the boundary of the limit function $(\tilde{g}(\boldsymbol{U}) = 0)$ and the origin is known as the reliability index, β. This parameter is fixed in correspondence to the exceedance probability and is computed by exploiting the symmetry of the joint standard normal cumulative distribution function, $\Phi(x)$:

$$\begin{aligned} p_e &\cong \Phi(\beta) \\ \beta &\cong -\Phi^{-1}(p_e) \end{aligned} \tag{13}$$

Although the boundary of the limit function can adopt complex shapes, it can reportedly be approximated by its first-order Taylor expansion (Hasofer and Lind, 1974). Then, an optimization procedure is applied as follows:

$$\text{Given}\quad \beta : \text{find } W_{RP} = max|W(\boldsymbol{U})|;\, subjectto|\boldsymbol{U}| = \beta \tag{14}$$

The result is a hypersphere of radius β in the standard normal space that shall be transformed back to the space of the original variables. Herein, two reversible transformation rules were applied because the mean wind speed and the turbulence structure follow different distribution types. The Weibull distributed mean wind speed was transformed with the Rosenblatt transform (Rosenblatt, 1952), while the correlated lognormal distributed turbulence parameters were transformed with a linear transform.

The Rosenblatt transformation works by obtaining the joint CDF from the product of the marginals:

$$F_{x1x2\ldots xn}(x_1, x_2, \ldots, x_n) = F_{x1}(x_1)F_{x2}(x_2|x_1)\ldots F_{xn}(x_n|x_{n-1}\ldots.x_{\text{-}}1) \tag{15}$$

Then, the variables are transformed by considering the conditional distributions individually. The mean wind speed was chosen as the first variable, as it is considered the most important variable for the buffeting response of long-span bridges (Castellon et al., 2021). Then, the mean wind speed was transformed first.

$$F_V(V) = \Phi(u_1) \leftrightarrow \mathrm{V} = F_{\mathrm{V}}^{-1}[\Phi(u_1)] \tag{16}$$

When the stochastic variables are correlated and normally distributed, the linear transformation rule can be applied.

$$\begin{aligned} &\boldsymbol{U} = \boldsymbol{A}(\boldsymbol{X} - \boldsymbol{M}_X) \leftrightarrow \boldsymbol{X} = \boldsymbol{A}^{-1}\boldsymbol{U} + \boldsymbol{M}_X \\ &\boldsymbol{M}_X = \left[\mu_{x_1}\ \mu_{x_2}, \ldots,\ \mu_{x_n}\ \right] \end{aligned} \tag{17}$$

where A is a triangular matrix that can be found using the Cholesky decomposition of the covariance matrix C_{XX}, which is Hermitian and positive definite:

$$\boldsymbol{C}_{XX} = \boldsymbol{A}^{-1}\,\boldsymbol{A}^{-T} \tag{18}$$

with

$$\boldsymbol{C}_{XX} = \begin{bmatrix} \sigma_{x_1}^2 & \rho_{12}\sigma_{x_1}\sigma_{x_2} & \cdots & \rho_{1n}\sigma_{x_1}\sigma_{x_n} \\ \rho_{21}\sigma_{x_1}\sigma_{x_2} & \sigma_{x_2}^2 & \cdots & \rho_{2n}\sigma_{x_2}\sigma_{x_n} \\ \vdots & \vdots & \ddots & \vdots \\ \rho_{n1}\sigma_{x_1}\sigma_{x_n} & \rho_{n2}\sigma_{x_2}\sigma_{x_n} & \cdots & \sigma_{x_n}^2 \end{bmatrix} \tag{19}$$

Then, for the case in which stochastic variables are correlated and lognormally distributed, the same transformation rule procedure applies, and the lognormal variables can be found as follows:

$$\boldsymbol{X} = \exp\left(\boldsymbol{A}^{-1}\boldsymbol{U} + \boldsymbol{M}_X\right) \tag{20}$$

The full set of turbulence parameters conditional on the mean wind speed are transformed in a single operation using the linear transformation rule for the case of lognormal distributed variables from Equation (20).

$$F_{I_u,I_v,I_w,A_u,A_v,A_w|V}\ (I_u, I_v, I_w, A_u, A_v, A_w|V) = \Phi(u_2, u_3, u_4, u_5, u_6, u_7) \tag{21}$$

4.2. Sulafjord contours

4.2.1. Reference values from standard methodologies

The general practice in bridge design is to estimate the mean wind speed from an extreme value analysis and the turbulence variables from code values or measurements, usually dependent on the mean wind speed and the reference height. Reference values of the wind variables required for the Sulafjord bridge following the standard design methodology are reported in Table 8. The table presents mean wind speeds with 50- and 100-year return periods. Additionally, the table provides turbulence intensities (I_u, I_v, I_w) and spectral parameters ($A_{u,}A_v$, A_w) corresponding to their mean values for recordings above 15 m/s from the dominant incoming direction. Reference values of turbulence intensities and spectral parameters at the Sulafjord center were adopted from Trælbonset since site measurements are not available at the fjord center.

4.2.2. Design contours

The environmental contour lines for the Sulafjord bridge design for return periods of 4, 50 and 100 years are shown in Fig. 19. Site measurement data are also plotted along with the contour lines. The x-axis of the subfigures represents the mean wind speed, and the y-axis represents each of the remaining turbulence parameters. The 4-year contours represent the measurement campaign period and envelope the measured data well. Additionally, the 50- and 100-year return period contours represent extreme wind conditions. Reference values are reported in Table 8. Finally, contour surfaces for the 100-year return period of the turbulence intensity parameters are shown in Fig. 20.

5. Discussion

The results show that environmental contours successfully capture the variability in the site data. In general, the 4-year contours covered the measured data well. Furthermore, 50- and 100-year contours produce reasonable estimates of the extreme wind fields that follow the site data. Compared with the current design methodology, the contours represent a more complete description of the extreme wind fields, as they also include turbulence measurements. Therefore, presenting the extreme wind conditions of the Sulafjord Bridge site with environmental contours shows a significant advantage to the traditional wind speed method using the same resources typically available in the design of long-span bridges. Then, a designer will use the contours to identify combinations of environmental parameters that provide the largest response by checking points along the contour lines. The procedure is explained in (Lystad et al., 2020), (Lystad et al., 2021).

5.1. Model recommendations

Several challenges arise when developing contours based on probabilistic modeling with the proposed strategy for long-span bridge design. First, hindcast simulations are limited to the mesoscale, and site measurement campaigns have relatively short periods. Thus, the mean wind speed and turbulence parameters of probabilistic modeling should be established separately. Furthermore, locations with higher wind loads are often in the middle of the bridge's span, where site measurements from mast stations are rarely available. Additionally, establishing the joint distribution of the turbulence parameters requires approximations that are applicable beyond the range of available data. In the following section, the modeling limitations are discussed together with the strategies implemented to overcome these limitations.

First, there are discrepancies between the averaging period of the hindcast data and the site measurements. The hindcast data were simulated using a 1-h averaging period, whereas the site measurements used 10 min. It is recommended that the discrepancies between the averaging periods for the mean wind speed be resolved by considering the adjacent short-term 10-min intervals in 1 h as independent. This assumption yields conservative estimations of the mean speed values. The benefit from using data from the meso-scale model is that longer time series of mean wind speed are available and that data for mean wind speed is available at the middle of the fjord. Mast measurements is clearly the best alternative if many years of data in a representative

Table 8
Reference values from mean wind speed and turbulence parameters.

Parameter	V_{50}	V_{100}	I_u	I_v	I_w	A_u	A_v	A_w
Sulafjord Center	39.83	42.1	0.089	0.091	0.057	12.08	29.37	5.33

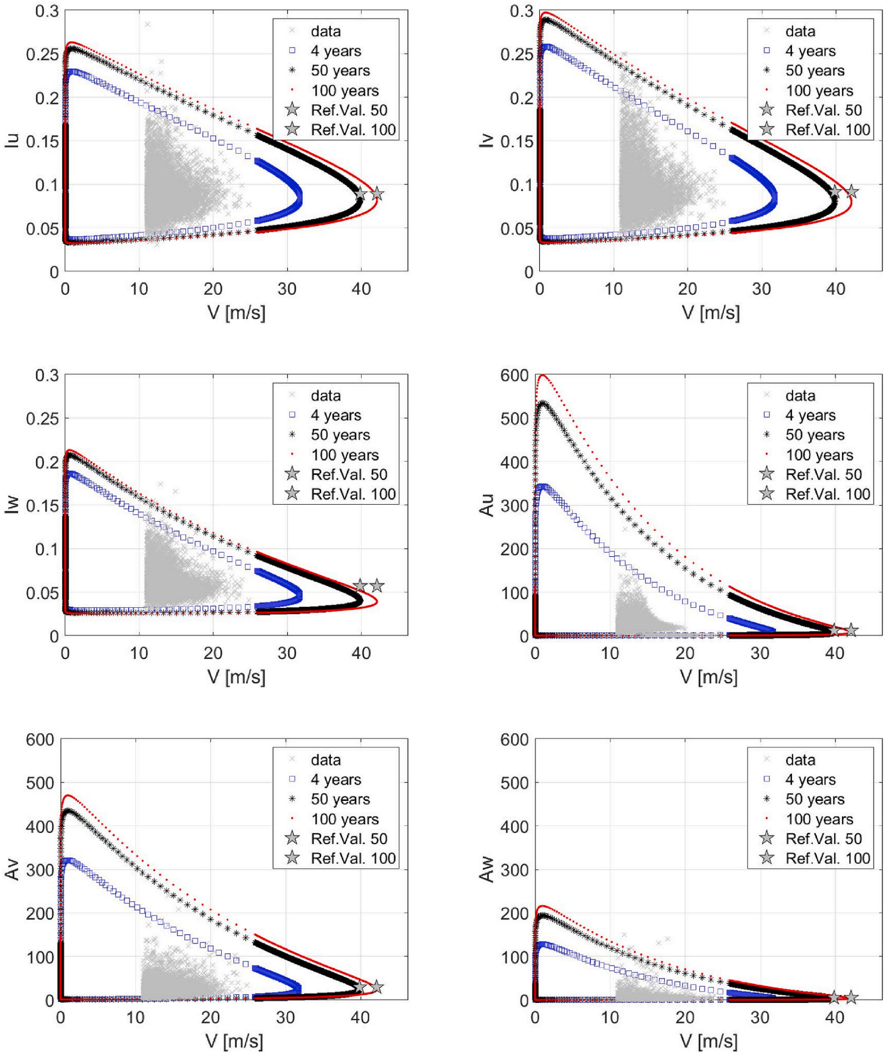

Fig. 19. Environmental contours of Sulafjord bridge design.

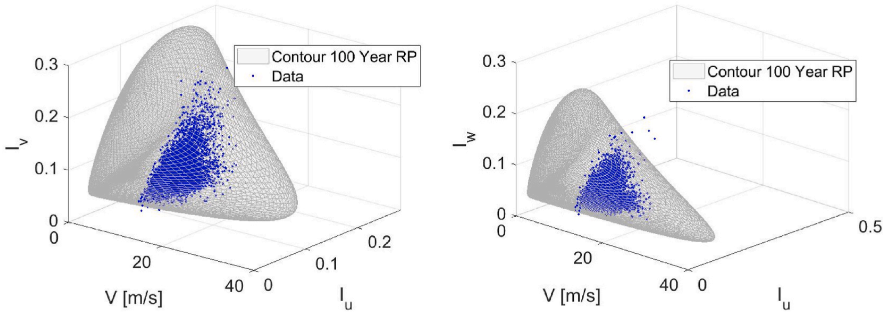

Fig. 20. Surface contours of the 100-year return period for Sulafjord bridge design: a) $I_u - I_v$ b). $I_u - I_w$

location at the bridge site is available. This is however rarely the case making meso-scale simulation an attractive alternative to cover longer time periods.

Additionally, site measurement data are not available at the center of Sulafjord, making it necessary to infer its turbulence properties from other available locations. Kårsteinen and Langeneset were not considered in the analysis because of their distant locations from the bridge track. The Kvitneset station could also be considered as a viable alternative, but it is seen that the winds at the midspan of the fjord does not follow the same direction as the winds at Kvitneset. The local topography around the station also suggests that local effects are likely to dominate the turbulence characteristics. On the other hand, Trælboneset station has almost twice the amount of strong wind records (above 17 m/s). Thus, it was decided to derive the turbulence model after Trælboneset records as it also contains a good number of records to ensure a good distribution fitting in the mean wind speed range above 10 m/s.

Finally, Figs. 17 and 18 show the variation in the joint distribution parameters with respect to the mean wind speed. All the correlation coefficients ρ_{ii} and the lognormal mean parameter of the turbulence intensity $\widetilde{\mu}_{I_i}$ agree with their adopted functions. Significant deviations can be observed between with the lognormal standard deviation parameter $\widetilde{\sigma}_{I_i}$ and its adopted constant value. The number of recordings decrease for higher mean wind speeds affecting the uncertainty in the distribution fittings with a stronger effect on the $\widetilde{\sigma}_{I_i}$ parameter compared to the $\widetilde{\mu}_{I_i}$ parameter. Then, trends of sigma may be attributed to lack of data, because using linear or higher order functions produce unrealistic estimates of the turbulence in the extrapolated region. Therefore, the constant vale of $\widetilde{\sigma}_{I_i}$ was chosen as it produced stable estimates. Similar approach may be found the literature (Fenerci and Øiseth, 2018), (Hannesdóttir et al., 2019).

6. Conclusion

In this paper, the wind conditions and wind characterization at the Sulafjord Bridge site from the 4-year mast measurement campaign and the 10-year hindcast simulation data are presented. A probabilistic model of the environmental variables was established using a novel and practical strategy in which hindcast simulations are combined with filed measurements. Efficient techniques for combining these datasets are an open matter of discussion and therefore were addressed in this study. The probabilistic model expresses the joint probability distributions of the turbulence intensities (I_u,I_v, I_w) and spectral parameters (A_u,A_v,A_w) conditional on the mean wind speed (V) and mean wind direction. The mean wind speed was modeled using a Weibull distribution transformed from the extreme value distribution of the hindcast data, where the mean wind direction was modeled as a discrete variable since the fjord distributes the flow in discrete directions. The joint distribution of the remaining wind variables (turbulence intensities and spectral parameters) were established from the site measurement data as a joint lognormal distribution with correlation coefficients.

Environmental contours were obtained for 4-, 50- and 100-year return periods based on the probabilistic turbulence model. The contours reasonably captured the variability in the wind conditions at the fjord site when compared with the site measurements. The contours present combinations of wind field parameters for the given return periods. As such, for instance wind conditions with higher turbulence intensities occurring at lower mean wind speeds can also be obtained and checked for design purposes. Therefore, designing the Sulafjord Bridge with the ECM will increase the accuracy in the extreme response predictions as opposed to the current practice. It is also concluded that the ECM uses the available data in a more efficient manner.

In conclusion, it is recommended to use the ECM to characterize the wind conditions at a bridge site using data typically available at the design stage of long-span bridges.

Data availability statement

Some or all data, models, or code used during the study were provided by a third party. Hindcast data from Kjeller Vindteknikk AS. Direct requests for these materials may be made to the provider as indicated in the Acknowledgements.

Some or all data, models, or code generated or used during the study are available in a repository online in accordance with funder data retention policies. Mast measurements (Norwegian Meteorological Institute, 2020).

CRediT authorship contribution statement

Dario Fernandez Castellon: Writing – original draft, Software, Methodology, Formal analysis. **Aksel Fenerci:** Writing – review & editing, Data curation, Investigation. **Ole Øiseth:** Conceptualization, Supervision, Project administration.

Declaration of competing interest

The authors declare that they have no known competing financial interests or personal relationships that could have appeared to influence the work reported in this paper.

Acknowledgments

The research presented in this paper was financially supported by the NPRA as a part of the E-39 Coastal highway project. The authors recognize the help from Kjeller Vindteknikk AS and Hálfdán Ágústsson for sharing the hindcast data and from the Norwegian Meteorological Institute for making the site measurement data available.

References

Bang Huseby, A., Vanem, E., Natvig, B., 2013. A new approach to environmental contours for ocean engineering applications based on direct Monte Carlo simulations. Ocean Eng 60, 124–135. https://doi.org/10.1016/j.oceaneng.2012.12.034.

Barni, N., Øiseth, O., Mannini, C., 2021. Time-variant self-excited force model based on 2D rational function approximation. J. Wind Eng. Ind. Aerod. 211, 104523. https://doi.org/10.1016/j.jweia.2021.104523.

Bazzurro, P., Winterstein, S.R., Ude, T.C., Cornell, C.A., 1996. Magnitude-distance contours for probabilistic seismic hazard analysis. Probabilistic Mech. Struct. Geotech. Reliab. Proc. Spec. Conf. 202–205. August 1996.

Berrisford, P., et al., 2009. The ERA-Interim Archive. ECMWF, Shinfield Park, Reading [Online]. Available: https://www.ecmwf.int/node/8173.

Castellon, D.F., 2019. Aksel Fenerci, and O. Øiseth, "A probabilistic analysis OF the wind field at SULAFJORDEN bridge SITe. In: ANCRiSST:14th International Workshop on Advanced Smart Materials and Smart Structures Technology, pp. 115–118. https://doi.org/10.13133/9788893771146 [Online]. Available:

Castellon, D.F., Fenerci, A., Øiseth, O., 2021. A comparative study of wind-induced dynamic response models of long-span bridges using artificial neural networks, support vector regression and buffeting theory. J. Wind Eng. Ind. Aerod. 209, 104484. https://doi.org/10.1016/j.jweia.2020.104484.

CEN, 2004. Eurocode 1: Actions on Structures - Part 1-4, 1. General actions - Wind actions.

Chai, W., Leira, B.J., 2018. Environmental contours based on inverse SORM. Mar. Struct. 60, 34–51. https://doi.org/10.1016/j.marstruc.2018.03.007. December 2017.

Ciampoli, M., Petrini, F., Augusti, G., 2011. Performance-based wind engineering: towards a general procedure. Struct. Saf. 33 (6), 367–378. https://doi.org/10.1016/j.strusafe.2011.07.001.

Davenport, A.G., 1983. The relationship of reliability to wind loading. J. Wind Eng. Ind. Aerod. 13 (1–3), 3–27. https://doi.org/10.1016/0167-6105(83)90125-3.

Dee, D.P., et al., 2011. The ERA-Interim reanalysis: configuration and performance of the data assimilation system. Q. J. R. Meteorol. Soc. 137 (656), 553–597. https://doi.org/10.1002/qj.828.

Fenerci, A., Øiseth, O., 2017. Measured buffeting response of a long-span suspension bridge compared with numerical predictions based on design wind spectra. J. Struct. Eng. 143 (9), 04017131 https://doi.org/10.1061/(asce)st.1943-541x.0001873.

Fenerci, A., Øiseth, O., 2018. Site-specific data-driven probabilistic wind field modeling for the wind-induced response prediction of cable-supported bridges. J. Wind Eng. Ind. Aerod. 181, 161–179. https://doi.org/10.1016/j.jweia.2018.09.002. June.

Fenerci, A., Øiseth, O., Rønnquist, A., 2017. Long-term monitoring of wind field characteristics and dynamic response of a long-span suspension bridge in complex terrain. Eng. Struct. 147, 269–284. https://doi.org/10.1016/j.engstruct.2017.05.070.

Fitzwater, L.R.M., Cornell, C.A., Veers, P.S., 2003. Using Environmental Contours to Predict Extreme Events on Wind Turbines. ASME 2003 Wind Energy Symp. Wind., pp. 244–258. https://doi.org/10.1115/wind2003-865

Furevik, B.R., Agustsson, H., Lauen Borg, A., Midjiyawa, Z., Nyhammer, F., Gausen, M., 2020. Meteorological observations in tall masts for the mapping of atmospheric flow in Norwegian fjords. Earth Syst. Sci. Data 12 (4), 3621–3640. https://doi.org/10.5194/essd-12-3621-2020.

Gumbel, E.J., 1958. Statistics of Extremes. Columbia University Press, New York.

Hannesdóttir, Á., Kelly, M., Dimitrov, N., 2019. Extreme wind fluctuations: joint statistics, extreme turbulence, and impact on wind turbine loads. Wind Energy Sci 4 (2), 325–342. https://doi.org/10.5194/wes-4-325-2019.

Harper, B., Kepert, J., Ginger, J., 2009. 4B . 1 WIND SPEED TIME AVERAGING CONVERSIONS FOR TROPICAL CYCLONE, pp. 6–8. June 2014.

Haselsteiner, A.F., Ohlendorf, J.H., Wosniok, W., Thoben, K.D., 2017. Deriving environmental contours from highest density regions. Coast. Eng. 123, 42–51. https://doi.org/10.1016/j.coastaleng.2017.03.002. March.

Hasofer, A.M., Lind, N.C., 1974. An exact and invariant first order reliability format. J. Eng. Mech. Div. 100, 111–121. July.

Haver, S., Winterstein, S.R., 2009. Environmental contour lines: a method for estimating long term extremes by a short term analysis. Trans. - Soc. Nav. Archit. Mar. Eng. 116, 116–127. January.

Heredia-Zavoni, E., Montes-Iturrizaga, R., 2019. Modeling directional environmental contours using three dimensional vine copulas. Ocean Eng. 187, 106102. https://doi.org/10.1016/j.oceaneng.2019.06.007. July 2018.

Kaimal, J.C., Wyngaard, J.C., Izumi, Y., Coté, O.R., 1972. Spectral characteristics of surface-layer turbulence. Q. J. R. Meteorol. Soc. 98 (417), 563–589. https://doi.org/10.1002/qj.49709841707.

Kareem, A., 1987. Wind effects on structures: a probabilistic viewpoint. Probabilist. Eng. Mech. 2 (4), 166–200. https://doi.org/10.1016/0266-8920(87)90009-9.

Karmakar, D., Bagbanci, H., Guedes Soares, C., 2016. Long-term extreme load prediction of spar and semisubmersible floating wind turbines using the environmental contour method. J. Offshore Mech. Arctic Eng. 138 (2), 1–9. https://doi.org/10.1115/1.4032099.

Klemp, J.B., Skamarock, W.C., Dudhia, J., 2007. Conservative split-explicit time integration methods for the compressible nonhydrostatic equations. Mon. Weather Rev. 135 (8), 2897–2913. https://doi.org/10.1175/MWR3440.1.

Li, Q.S., Li, X., Chan, P.W., 2021. Impact of a fifty-year-recurrence super typhoon on skyscrapers in Hong Kong: large-scale field monitoring study. J. Struct. Eng. 147 (3), 04021004 https://doi.org/10.1061/(asce)st.1943-541x.0002930.

Lieblein, J., 1974. Efficient Lillethods of Extreme-Value Methodology.

Loth, C., Baker, J.W., 2015. Environmental contours for determination of seismic design response spectra. In: 12th Int. Conf. Appl. Stat. Probab. Civ. Eng. ICASP 2015.

Lystad, T.M., Fenerci, A., Øiseth, O., 2018. Evaluation of mast measurements and wind tunnel terrain models to describe spatially variable wind field characteristics for long-span bridge design. J. Wind Eng. Ind. Aerod. 179, 558–573. https://doi.org/10.1016/j.jweia.2018.06.021. June.

Lystad, T.M., Fenerci, A., Øiseth, O., 2020. Buffeting response of long-span bridges considering uncertain turbulence parameters using the environmental contour method. Eng. Struct. 213, 110575. https://doi.org/10.1016/j.engstruct.2020.110575. March.

Lystad, T.M., Fenerci, A., Øiseth, O., 2021. Long-term extreme buffeting response of cable-supported bridges with uncertain turbulence parameters. Eng. Struct. 236 https://doi.org/10.1016/j.engstruct.2021.112126. March.

Michalakes, et al., 2001. Development of a next generation regional weather research and forecast model. Developments in teracomputing. https://doi.org/10.1142/4819.

Midjiyawa, Z., Cheynet, E., Reuder, J., Ágústsson, H., Kvamsdal, T., 2021. Potential and challenges of wind measurements using met-masts in complex topography for bridge design: Part I – integral flow characteristics. J. Wind Eng. Ind. Aerod. 211 https://doi.org/10.1016/j.jweia.2021.104584.

Moan, T., Gao, Z., Ayala-Uraga, E., 2005. Uncertainty of wave-induced response of marine structures due to long-term variation of extratropical wave conditions. Mar. Struct. 18 (4), 359–382. https://doi.org/10.1016/j.marstruc.2005.11.001.

Montes-Iturrizaga, R., Heredia-Zavoni, E., 2015. Environmental contours using copulas. Appl. Ocean Res. 52, 125–139. https://doi.org/10.1016/j.apor.2015.05.007.

Moriarty, P.J., Holley, W.E., Butterfield, S., 2002. Effect of turbulence variation on extreme loads prediction for wind turbines. J. Sol. Energy Eng. Trans. ASME 124 (4), 387–395. https://doi.org/10.1115/1.1510137.

Naess, A., Moan, T., 2012. Stochastic Dynamics of Marine Structures. Cambridge University Press, Cambridge.

Naess, A., Gaidai, O., Karpa, O., 2013. Estimation of extreme values by the average conditional exceedance rate method. J. Probab. Stat. https://doi.org/10.1155/2013/797014.

Niedzwecki, J.M., Van De Lindt, J.W., Yao, J.T.P., 1998. Estimating extreme tendon response using environmental contours. Eng. Struct. 20 (7), 601–607. https://doi.org/10.1016/S0141-0296(97)00061-8.

Norwegian Meteorological Institute, 2020. Observasjonsdata i SVV-E39-prosjektet. https://thredds.met.no/thredds/catalog/obs/mast-svv-e39/catalog.html.

Pagnini, L., 2010. Reliability analysis of wind-excited structures. J. Wind Eng. Ind. Aerod. 98 (1), 1–9. https://doi.org/10.1016/j.jweia.2009.08.010.

Pagnini, L.C., Solari, G., 2002. Gust buffeting and turbulence uncertainties. J. Wind Eng. Ind. Aerod. 90 (4–5), 441–459. https://doi.org/10.1016/S0167-6105(01)00202-1.

Raed, K., Teixeira, A.P., Guedes Soares, C., 2020. Uncertainty assessment for the extreme hydrodynamic responses of a wind turbine semi-submersible platform using different environmental contour approaches. Ocean Eng. 195, 106719. https://doi.org/10.1016/j.oceaneng.2019.106719. April 2019.

Rosenblatt, M., 1952. Remarks on a multivariate transformation author (s): murray Rosenblatt published by : Institute of mathematical statistics stable. Ann. Math. Stat. 23 (3), 470–472. REFERENCES Linked references are available on JSTOR for this article. http://www.jstor.org/stable/2236692.

Saranyasoontorn, K., Manuel, L., 2004. From the environmental contour method. Eng. Conf. 1, 128–135.

Saranyasoontorn, K., Manuel, L., 2006. Design loads for wind turbines using the environmental contour method. J. Sol. Energy Eng. Trans. ASME 128 (4), 554–561. https://doi.org/10.1115/1.2346700.

Seo, D.W., Caracoglia, L., 2012. Statistical buffeting response of flexible bridges influenced by errors in aeroelastic loading estimation. J. Wind Eng. Ind. Aerod. 104 (106), 129–140. https://doi.org/10.1016/j.jweia.2012.03.036.

Seo, D.W., Caracoglia, L., 2013. Estimating life-cycle monetary losses due to wind hazards: fragility analysis of long-span bridges. Eng. Struct. 56, 1593–1606. https://doi.org/10.1016/j.engstruct.2013.07.031.

Skamarock, W.C., et al., 2008. A description of the advanced research WRF version 3. Powers, J. G.

Solari, G., 1997. Wind-excited response of structures with uncertain parameters. Probabilist. Eng. Mech. 12 (2), 75–87. https://doi.org/10.1016/s0266-8920(96)00027-6.

Solari, G., Piccardo, G., 2001. Probabilistic 3-D turbulence modeling for gust buffeting of structures. Probabilist. Eng. Mech. 16 (1), 73–86. https://doi.org/10.1016/S0266-8920(00)00010-2.

Ucar and, D.T.C., 2013. The weather research and forecast model. http://www.wrf-model.org/index.php.

van de Lindt, J.W., Niedzwecki, J.M., 1997. Sensitivity of TLP tendon reliability estimates to excitation by multi-peaked random seas. Proc. Int. Offshore Polar Eng. Conf. 4, 139–144.

Van De Lindt, J.W., Niedzwecki, J.M., 2000. Environmental contour analysis in earthquake engineering. Eng. Struct. 22 (12), 1661–1676. https://doi.org/10.1016/S0141-0296(99)00114-5.

Vanem, E., 2019. 3-Dimensional environmental contours based on a direct sampling method for structural reliability analysis of ships and offshore structures. Ships Offshore Struct. 14 (1), 74–85. https://doi.org/10.1080/17445302.2018.1478377.

Vegvesen, Statens, 2016. E39 Sulafjorden Multispan Suspension Bridge Om GBS Feasibility Studies-Presentation [Online]. Available: https://www.vegvesen.no/_attachment/1545452/binary/1135150?fast_title=16+Flerspenns+hengebru+på+fast+fundament+%28GBS%29.pdf.

Velarde, J., Vanem, E., Kramhøft, C., Sørensen, J.D., 2019. Probabilistic analysis of offshore wind turbines under extreme resonant response: application of environmental contour method. Appl. Ocean Res. 93, 101947. https://doi.org/10.1016/j.apor.2019.101947. September.

Vindteknikk, Kjeller, og Vartdalsfjorden, Sulafjorden, 2018. Møre Og Romsdal Analyse Av Modellert Vind. strøm og bølger for.

Wang, H., Li, A., Niu, J., Zong, Z., Li, J., 2013. Long-term monitoring of wind characteristics at Sutong Bridge site. J. Wind Eng. Ind. Aerod. 115, 39–47. https://doi.org/10.1016/j.jweia.2013.01.006.

Winterstein, S.R., Ude, T.C., a Cornell, C., Bjerager, P., Haver, S., 1993. Environmental parameters for extreme response: inverse form with omission factors. Icossar- 93, 9–13. August.

Castellon D., Fenerci A., Øiseth O., Petersen Ø.

III

Investigations of the long-term extreme buffeting response of long-span bridges using importance sampling Monte Carlo simulations

Manuscript submitted to journal publication 2022

This article is submitted for publication and is therefore not included.

IV

Castellon D., Fenerci A., Øiseth O., Petersen Ø.

Full long-term buffeting analysis of suspension bridges using Gaussian process surrogate modelling and importance sampling Monte Carlo simulations

Manuscript submitted to journal publication 2022

This article is submitted for publication and is therefore not included.

ISBN 978-82-326-5343-0 (printed ver.)
ISBN 978-82-326-5401-7 (electronic ver.)
ISSN 1503-8181 (printed ver.)
ISSN 2703-8084 (online ver.)

NTNU
Norwegian University of
Science and Technology